UNIVERSITY OF COPENHAGEN
FACULTY OF SCIENCE

Master's Thesis

Center for Quantum Devices

Supercurrent and Screening of Spins in a Double Quantum Dot Josephson Junction

Alexandros Vekris
dbz341@alumni.ku.dk

Supervisors: Jesper Nygård, Kasper Grove-Rasmussen

August 2018

Abstract

In my thesis, I studied a lateral double quantum dot (DQD) system defined in a one-dimensional nanowire coupled to superconducting electrodes. The goal of this project was to investigate the supercurrent behaviour through this novel Josephson junction, as well as experiment with screening effects induced by increased coupling Γ between the quantum dots (QDs) and the leads.

It was found that in the honeycomb regime, on which the couplings are much weaker than the charging energies of the QDs $\Gamma \ll U$, the occupation number of the dots directly affects the sign of the supercurrent flowing through the junction. That is because even and odd electrons in the DQD correspond to $|S\rangle$ and $|D\rangle$ ground state of the system respectively. The ground state dictates whether the phase of the supercurrent acquires a π, changing its sign to negative. A consistent behaviour of $0 \longrightarrow \pi$ phase transitions occurred for every $|S\rangle \longrightarrow |D\rangle$ ground state transition of the DQD.

Increasing the coupling to the leads with the aim of reaching the intermediate coupling regime $\Gamma \sim U$, triggered screening of $S = \frac{1}{2}$ states of the DQD. We demonstrate intermediate steps of the charge stability diagrams with increasing coupling proving the screening of a $|D\rangle$ ground state to a Yu-Shiba-Rusinov (YSR) singlet $|S_{\mathrm{YSR}}\rangle$. Furthermore we investigated screening of the singlet (1,1) charge sector, by screening its excited $|T\rangle$ state with $S = 1$ state, to a $|D_{\mathrm{YSR}}\rangle$. Lastly, we increased the coupling to both superconducting leads and studied simultaneous screening of both QDs. We traced these transitions by analysing the supercurrent through these charge states and observing its $0 \longrightarrow \pi$ transitions.

To conclude, these results point in the better understanding of how superconductors behave in close proximity to magnetic impurities, as well as aid in the better visualisation of supercurrent through a DQD system.

Acknowledgments

I want to thank Jesper Nygård for accepting me to his group and giving me the chance to work in this great research institute. I am also grateful to Kasper Grove-Rasmussen for his day to day assistance that he provided me during this project and for inspiring me in the Yu-Shiba-Rusinov physics.

I would like to extend my gratitude to Juan Carlos Estrada Saldaña for everything that he taught me, especially regarding measurements. Thank you for helping me whenever I asked your assistance. I would like to thank the other members of our group that welcomed me. Anders, Morten and Jacob, all the introductory help you provided me in the first months of my thesis was very important. I would also like to thank Gorm Steffensen and Jens Paaske for their valuable insights. This project would have been much harder without the technical lab assistance of QDev. Thank you Shiv for all the trainings and for helping me with all my fab-related issues.

I would like to thank my family, friends, and Ευγενία for their love and support during these years.

Contents

Chapter 1

Introduction

1.1 Introduction and motivation

In a superconductor, electrons condense into Cooper pairs. These pairs are broken by magnetic fields, resulting in a destruction of superconductivity. Due to this reason, magnetic impurities, even in very low concentrations, can significantly change the properties of the superconductor. Remarkably, this is the case even for a single magnetic impurity, which is known to produce so-called Yu-Shiba-Rusinov subgap states [1, 2, 3]. If the exchange coupling between the impurity and quasiparticles in the superconductor is strong enough, these states can cross zero energy, resulting in a doublet to singlet quantum phase transition of the ground state of the impurity-superconducting system.

A singly-occupied quantum dot constitutes a fully tunable magnetic impurity. Using a gate, one can very simply and conveniently tune the exchange coupling of the impurity to the superconductor. Using quantum dots defined in semiconductor nanowires with a superconductor, Yu-Shiba-Rusinov (YSR) states have been succesfully measured in transport spectroscopy [4]. Quantum phase transitions have been observed in both superconductor (S) / quantum dot (QD) / metal (N) and S-QD-S devices [5].

However, a platform for studying two-impurity Yu-Shiba-Rusinov physics is lacking. Two impurities in a superconductor constitute the most simple system with magnetic interactions. This system is a precursor to more complex high-T_c systems containing magnetic ions in the superconducting crystal [6]. Two quantum dots in series coupled to two superconducting leads, forming a S-DQD-S geometry, are the natural fully-tunable system that one can use to study YSR physics.

In such system, through gate-voltage tuning, one can go from a non-correlated ground state, in which the two dots are decoupled from the leads, to a novel fully correlated state in which the spins of the two dots are fully screened by quasiparticles in the superconductors.

Interestingly, such system also constitutes a Josephson junction, in which the weak-link is made of the DQD. This provides with the unique opportunity to study how the ground state of the system affects the supercurrent through the device. Such studies were done before in single dot junctions [7], and it was found that, at low coupling, the supercurrent aquires a phase π in the current-phase relation $I_s = I_c \cdot sin(\phi)$.

In this thesis, I will present an experimental work on how two magnetic impurities interact with a superconductor. To realize this, I defined two quantum dots in a nanowire. The nanowires I used are confined in two dimensions, as their diameter is less than 100 nm. To form a DQD, I used gates to obtain two wells in the profile of the conduction band along the axis of the wire. Additionally, these gates provided tunability of the tunnel couplings of the dots to the two superconducting leads, defined on the same nanowire.

There are two basic paths to be explored on this project:

- First of all, we want to study how supercurrent will flow through this Josephson junction in the weak coupling regime. A significant difference to other Josephson junctions is the addition of a second QD in series. Moreover, the dependence of supercurrent has not been studied in the past in the molecular regime of a DQD, where two charge states hybridise.
- Secondly, increasing the coupling to the leads would create the desired circumstances to observe screening of the QDs. Electrostatic gates provide full control of the system as tunnel couplings to the leads and the inter-dot coupling are controlled by them. Hence, it is possible to individually screen QDs or to demonstrate simultaneous screening, by increasing both tunnel couplings.

1.2 Thesis outline

In chapter 2, I introduce basic theory concepts which are essential for understanding and analysing the results that follow. Superconductors, nanowires and the basics of quantum dots are explained. The last sections cover a description of hybrid systems such as the Josephson junction and quantum dots coupled to superconducting leads.

Chapter 3 describes the fabrication process of the samples, as well as includes the principles of a dilution refrigerator and details of our measurement setup. Techniques such as UV-lithography, electron beam lithography and metal evaporation are covered in that section. Moreover, the challenge of selectively removing the Aluminium shell of the nanowires is described.

Chapter 4 consists of the main results regarding supercurrent through a double quantum dot. Initially, the device is introduced along with a characterisation of its energy scales U, Δ. Furthermore, a detailed description of the extended resistively and capacitively shunted junction

(RCSJ) model follows. The supercurrent measurements consist of ‘single’ dot measurements, where one QD is kept at fixed occupation, as well as a study of the supercurrent in the ‘molecular’ regime, in the vicinity of the triple points of a DQD. We observed interesting similarities and differences between supercurrent in a single QD and a DQD system. Finally, high bias measurements are shown, complementing the supercurrent measurements.

Chapter 5 covers the experiments that were done in the S-DQD-S device in the intermediate coupling regime $\Gamma \sim U$. In that regime, it is favorable for the superconducting leads to screen magnetic impurities i.e. QDs with odd number of electrons. We demonstrate ground state transitions in the doublet $|D\rangle$ ground state diamonds, as well as screening of the excitation of the singlet (1,1) sector, $|T_{11}\rangle \longrightarrow |D_{\mathrm{YSR}}\rangle$. These transitions are supported not only by the zero bias conductance of the charge stability diagram, but also via supercurrent measurements.

Chapter 6 contains the conclusions and perspectives of this thesis. In a brief summary, the results of chapter 4 and 5 are described. Last but not least, I write a few ideas about future experiments that are relevant for this project and can be implemented.

Chapter 2

Theory

This chapter will cover the fundamental concepts of physics that were encountered while analyzing the results of this thesis. Superconductivity, quantum dots and hybrid phenomena such as Josephson supercurrent and Yu-Shiba-Rusinov states, will be described from an experimental point of view to provide the tools needed to comprehend and analyze the data presented in following sections.

2.1 Superconductors

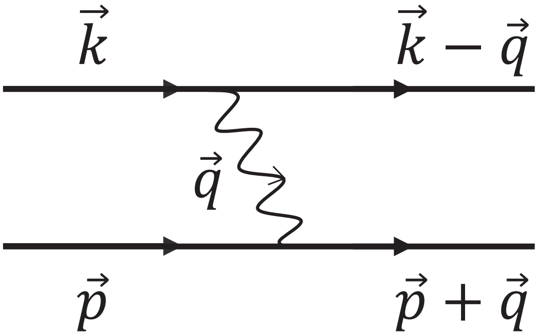

Figure 2.1: Two electrons with momenta $\vec{k}$ and $\vec{p}$, interact by exchanging a phonon of momentum $\vec{q}$. When the frequency corresponding to the energy the electrons exchange is lower than the phonon frequency ω, then the interaction causes an attraction of the two electrons.

Superconductivity is a fascinating phenomenon, where a material exhibits zero electrical resistance when cooled below a transition temperature T_c. The basic principle is that Cooper pairs

are formed by using two electrons of opposite spin and momentum. This results in the formation of zero spin particles, which are bosons. That allows them to condense on a single level, the Fermi level, as Pauli's exclusion principle is no longer valid. The net attractive force between these electrons is given by an electron - lattice interaction, effectively pairing the two electrons. Figure 2.1 describes the above interaction and the formation of a Cooper pair.
Bardeen Cooper and Schrieffer [8] described this interaction and wrote the BCS ground state

$$|BCS\rangle = \prod_{\vec{k}} (u_k + v_k c^{\dagger}_{-\vec{k}\downarrow} c^{\dagger}_{\vec{k}\uparrow}) |0\rangle$$

The intuitive idea is that when the momentum $k < k_f$ then $v_{\vec{k}} \rightarrow 1$ and we have a creation of a Cooper pair (the creation operators act on the vacuum state $|0\rangle$), while when $k > k_f$, $u_{\vec{k}} \rightarrow 1$ and we have no Cooper pair formation. $u_{\vec{k}}$ and $v_{\vec{k}}$ are normalized to give $u^2_{\vec{k}} + v^2_{\vec{k}} = 1$, since they basically provide the probability a state to be occupied or not.

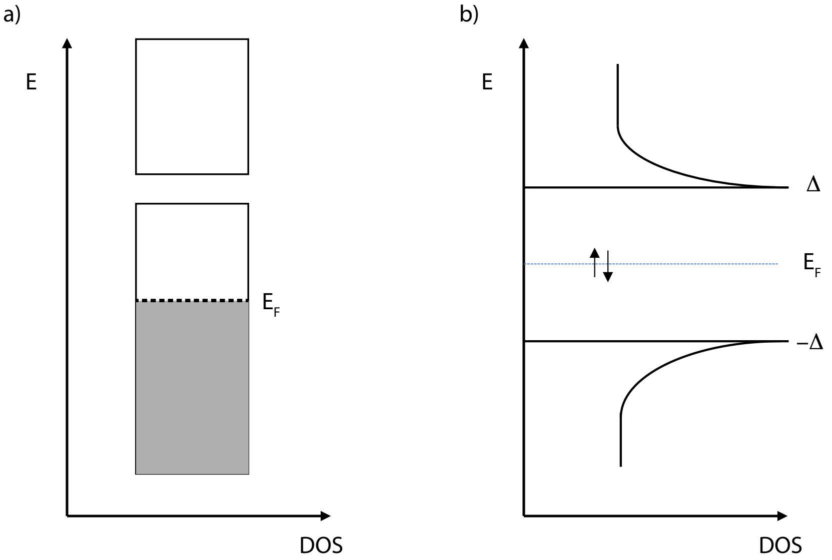

Figure 2.2: a) Schematic representation of density of states of a metal with respect to energy. In a metal, the Fermi energy E_F lies within a band. b) Below a specific temperature T_c, the material transitions from normal to the superconducting state, which has an energy band-gap of 2Δ with no available states. At the Fermi energy, Cooper pairs are formed.

Figure 2.2 shows the density of states of a metal in the normal and the superconducting state. A material is classified as a metal, insulator or semiconductor depending on the position of the Fermi level E_F, which indicates the occupied state with highest energy. In a metal, E_F lies within a band, while in other materials the band is filled and a energy band-gap is required to access new states. In the superconducting state, the density of states differs significantly, having a region around the

Fermi level which has no available states. That region is characterised by the superconducting gap Δ. From Fig. 2.2b we can see that Cooper pairs exist at the Fermi level and the energy required to 'break' a pair and excite a quasiparticle is Δ. The reason why there are more states at that energy compared to higher energies, is because Δ is the lowest energy required to excite a quasiparticle. A general expression of the density of states of a superconductor is

$$n_s(E) = n_F \frac{|E|}{\sqrt{|E^2 - \Delta^2|}} \Theta(|E| - |\Delta|)$$

Θ is a step function that gives 0 when its input is lower than 0, and 1 when it is higher.

BCS theory [8] predicts that a superconducting transition of a material is dependent on the temperature and the magnetic field applied. Superconductors are found in two types, Type I - which is also the material that we used for our experiments - and Type II [9], which will not be covered in this thesis. Figure 2.3 illustrates the magnetic field dependence versus the temperature of a type I superconductor. The interior of a superconductor cannot be penetrated by a magnetic field since the superconductor repels it, acting as a perfect diamagnetic material. This is known as the Meissner effect [10]. Superconductivity breaks down if a critical field larger than H_c is applied.

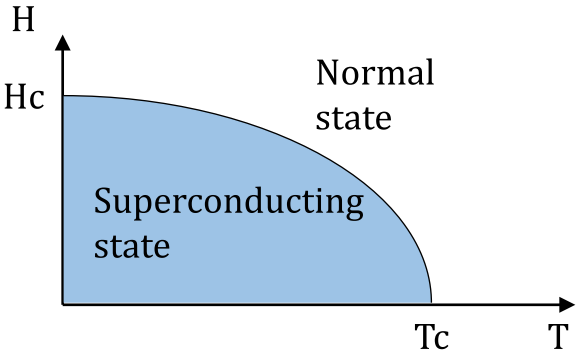

Figure 2.3: Magnetic field versus temperature of a superconducting material. As the applied magnetic field increases, the transition temperature T_c follows the black line.

Furthermore, superconductors exhibit zero electrical resistance when the condition $T < T_c$ is satisfied. That phenomenon happens because all the Cooper pairs are on the same ground state. In conventional metals, scattering and excitations occur during transport, but that is not the case in superconductors since excitations are forbidden unless there is enough energy to break a Cooper pair and excite a quasiparticle out of the superconducting gap Δ. Thus, there is no energy loss in Cooper pair transport, leading to zero electrical resistance.

2.2 Semiconductor nanowires

In order to study quantum transport phenomena, one can use a semiconductor nanowire as a channel due to the fact that it can be controlled by an electric field and be depleted, unlike a metal. That is essential if we want to be in the few electron regime. In particular, the nanowire quasi - 1D nature makes it much easier to confine electrons in all three dimensions, forming a quantum dot. This confinement can be achieved by using thin bottom gates below the nanowire that control the potential locally. In this thesis, InAs nanowires grown by Molecular Beam Epitaxy (MBE) in the [0001] wurtzite direction were used. With a hexagonal cross-section, these nanowires had a diameter of 100 nm and a few micrometers in length. The main reasons InAs nanowires are preferred in comparison to bulk semiconductors or other types of nanowires are:

- Low effective mass m^* of electrons which is translated to larger level spacing.
- Few lattice defects, boosting their mobility and overall transport properties.
- Small work function which allows easy contacting of the nanowires with metal, preventing Schottky barriers.
- Narrow band gap which allows the creation of carriers in the channel without applying too large gate voltages.

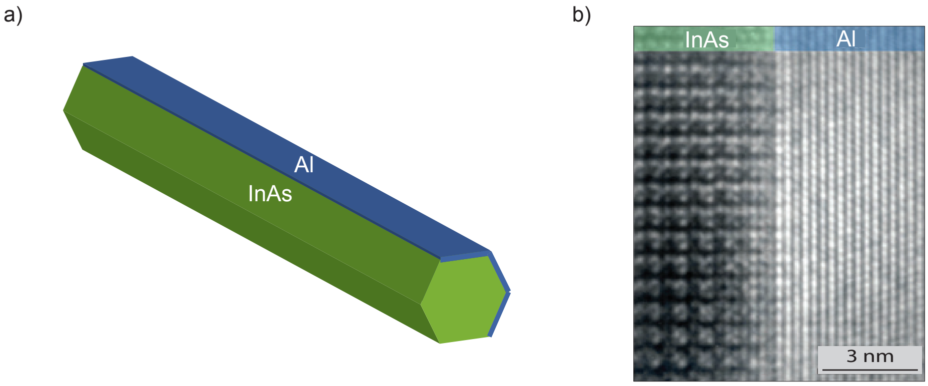

Figure 2.4: a) InAs nanowire (light green colour) with a three-facet epitaxial Aluminum film (blue colour). The film is 7 nm thick while the diameter of the nanowire 120 nm. b) A high resolution transmission electron microscopy image of an InAs nanowire with epitaxialy grown Aluminum. The uniform lattice match between the Al shell and the InAs core is clearly visible at the boundary between the two . Adapted from [11].

In 2015, Krogstrup et al. [11] succeeded in growing a new hybrid material. A semiconducting InAs nanowire with a thin shell of Aluminum of few nanometers. The important feature of these structures is the perfect lattice match between the semiconductor and the metal, which provides a fine interface for hybridization and a hard superconducting gap [12] in superconductor - insulator - superconductor (SIS) geometries. A material has a hard superconducting gap when the density of states go to zero for the range $-\Delta$ to Δ. A TEM image of such a nanowire can be seen in Fig. 2.4b. An illustration of these core-shell nanowire is shown in Fig. 2.4a. This breakthrough allowed the usage of these nanowires in quantum transport experiments [12, 13] and in our case, in coupling quantum dots to superconducting leads [14].

2.3 Quantum dots

This section will cover the basic principles and physics related to quantum dots. Energy scales, requirements to have a quantum dot and interaction between adjacent dots will be described in order to have the key ideas in mind when analyzing the results.

Single quantum dots

Let us assume that we have a semiconducting channel connected with two metallic electrodes that define the source and the drain. In order to pass an electron from the source to the semiconductor, a finite energy is required. One way is to apply a voltage V_{SD} between the two electrodes and shift the chemical potential by $-eV_{\mathrm{SD}}$. Another way, is to use a gate which is capacitively coupled to the semiconductor and can shift its energy bands. That is known as a metal oxide semiconductor field effect transistor (MOSFET) device which is widely used conventional electronics [15].

In the area of mesoscopic physics, it is helpful to have a system that exhibits quantized charge, in order to study specific phenomena. An example of such a system is a quantum dot (QD). Mesoscopic physics is the sub-discipline of condensed matter physics that studies materials in the micro or nano scale. Quantum dots are systems confined in all 3 dimensions, and can be considered as artificial atoms in the sense that they have very small capacitance due to their small size, which also gives rise to discrete energy levels. The energy scale that defines a quantum dot is the charging energy U. It is the energy needed in order to add an extra electron to the quantum dot. The nature of this interaction is the Coulomb repulsion among the electrons of the quantum dot. The charging energy is defined as $U = \frac{e^2}{C}$ with e being the charge of one electron and C the capacitance of the island. In order to observe this phenomenon, which is known as Coulomb blockade, certain criteria have to be met. Specifically,

- $U > k_{\mathrm{B}}T$ to prevent electron transport due to thermal excitations.
- The source drain voltage has to be lower than the charging energy $U > eV_{\mathrm{SD}}$.
- The resistance of the junction has to be larger than the quantum of resistance $R > \frac{h}{e^2}$.

The last bullet reassures that the system is in the tunneling regime. That means that there is small overlap of metal wavefunction with the semiconductor. Figure 2.5a shows a schematic of a quantum dot with two leads. A local bottom gate is used to control locally the potential, and tune the dot. In Fig. 2.5b a micrograph of a quantum dot which is defined on a semiconductor nanowire is illustrated. Gates that allow electrostatic control are used to create the tunnel barriers described above and also tune the levels of the quantum dots. Hence, if a semiconductor satisfies the bullet points noted above, then charge quantization is observed due to confinement, as illustrated in Fig. 2.5c. The schematic shows the energy in respect to position x of the system. The gray columns represent the tunnel barriers and the dashed line the Fermi energy, which is the highest occupied energy state. In the middle, a level of a quantum dot is depicted, having chemical potential $\mu(n-1)$, i.e. the energy to add the $n-1$'th electron to the system. In order to add another electron to the QD, energy equal to the charging energy U is required. This scenario is valid if the QD has odd number of electrons. Due to Pauli's exclusion principle, up to two electrons with opposite spin can occupy a state. That means that for even QD occupancy, n, the addition energy to add an additional charge includes the level spacing. As a result, $U + \Delta E$ energy is needed and this property is known as the even-odd effect in semiconductor quantum dots [16]. This process is illustrated in Fig. 2.5d. In the previous cases (panel c,d), transport is blocked through the system due to Coulomb blockade. To turn on the device, one could alter the voltage of the gate that tunes the QD, effectively shifting the chemical potential μ of the dot, as seen in Fig. 2.5e. That will bring the dot level in resonance with the source and drain chemical potentials. Alternatively, a source-drain bias would also provide the same result, depicted in Fig. 2.5f. The above methods describe sequential tunneling through a QD which occurs in the limit that the coupling to the leads is much smaller than the superconducting gap $\Gamma \ll U$.

Apart from the gates that control the quantum dot, barrier gates also serve the purpose of modifying the tunnel barriers. That parameter is known as coupling between the leads and the quantum dot, Γ_i, i=L, R. At the limit $\Gamma \gg U$, one can get a qualitative understanding of the conductance from the expression [17]

$$G = \frac{4e^2}{h}\frac{\Gamma_\mathrm{L}\Gamma_\mathrm{R}}{(\Gamma_\mathrm{L}+\Gamma_\mathrm{R})^2}$$

Γ describes the wavefunction overlap between a lead and the QD. It is clear by the formula, that if Γ is weak on one lead, then transport through that system will be suppressed. Hence, the coupling to the leads should be symmetric.

Figure 2.6 represents a typical measurement of a quantum dot system showing Coulomb peaks. Each peak reflects a resonance of a quantum dot level with the source and drain chemical potentials. As the plunger gate voltage increases, QD levels are pushed at lower electrochemical potential, alternating the channel between the off and the on state.

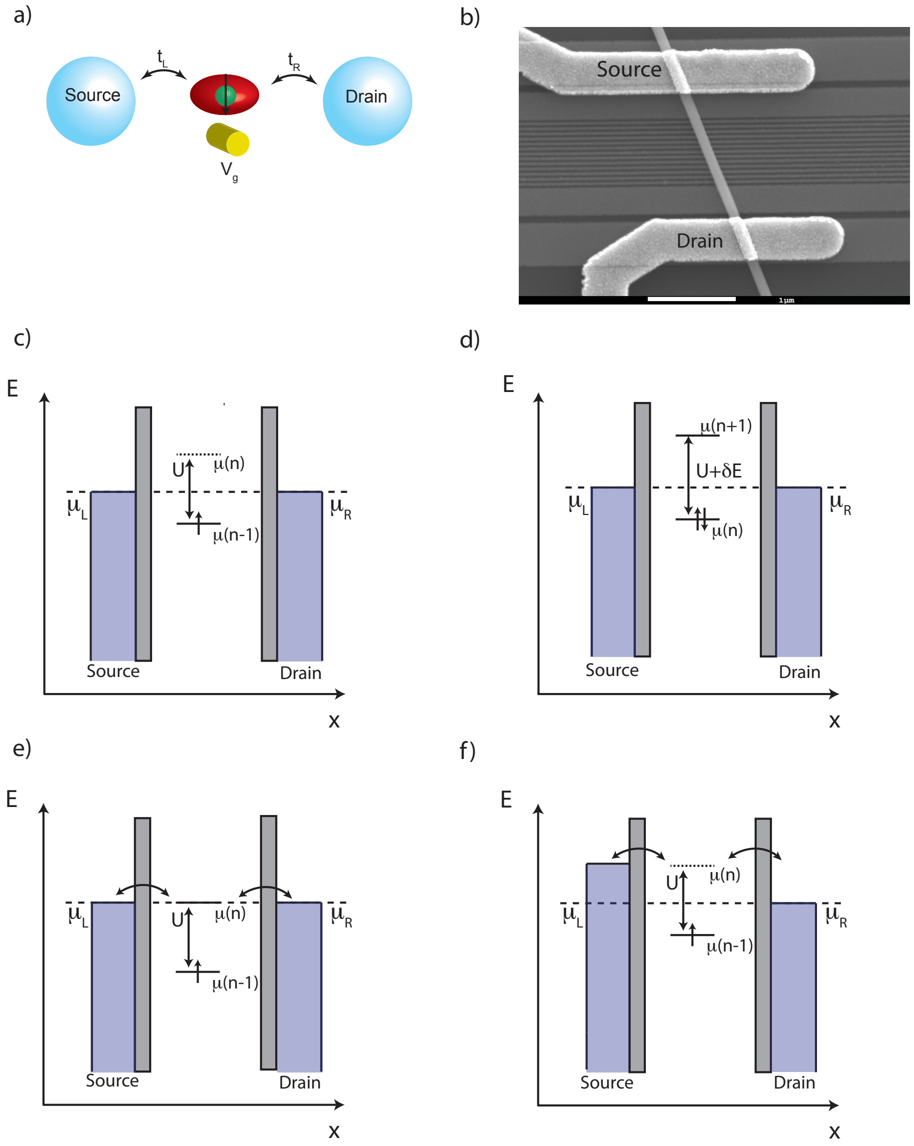

Figure 2.5: a) Schematic illustrating transport through a QD. The tunnel coupling to each lead - which is controlled by local gates - is described by t_L and t_R for the left and the right electrode respectively. Modifying the gate voltage V_g shifts the electrochemical potential of the QD. b) Electron micrograph of a nanowire based device. Bottom gates are used to define the barriers needed to form QDs. c) An energy diagram schematic illustrating the Coulomb blockade in a QD. The two metallic reservoirs (source and drain) have filled states up to the Fermi energy and their chemical potentials are equal $\mu_L = \mu_R$. Gray bars represent the tunnel barriers. The QD has $n-1$ number of electrons with $n-1$ being an odd number. The electron corresponding to the $n-1$'th level is singly occupying a state and as a result a charging energy U is needed to add an extra electron to the level. d) Now the QD has even number of electrons, meaning that the next electron will use the next orbital. The energy required now is the charging energy plus the level spacing of the orbitals $U + \Delta E$. e-f) These diagrams show the two possible ways of activating single electron transport in the channel, either by tuning the levels of the QD (e), or by applying a bias between the two leads.

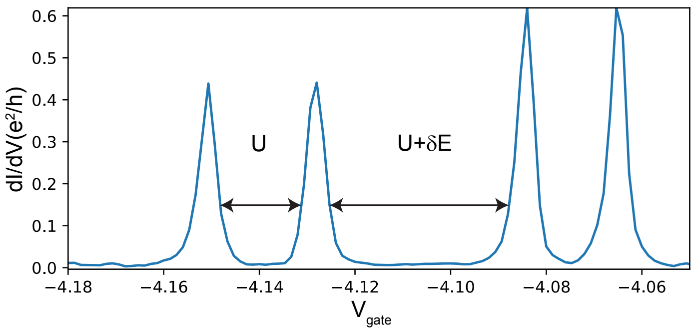

Figure 2.6: An example of Coulomb peaks of a QD. Zero bias conductance is plotted with respect to gate voltage. As the gate voltage changes, transport through the alternates between the off and the on state. The even-odd effect can be observed, which is a signature of level spacing presence in the QD. It is clear that the level spacing ΔE is not negligible.

To analyze a QD system, is it essential to study its ground state. In a quantum dot there can be either even or odd number of electrons. If the total number is odd, then the ground state of the system will be a doublet $|D\rangle$, because the unpaired electron will be free to be either spin up, or spin down, thus providing two degenerate states. On the other hand, if the total number of electrons is even, then all the levels will be occupied by two electrons which form a singlet ground state $|S\rangle = \frac{1}{\sqrt{2}}(\uparrow_1\downarrow_1 - \downarrow_1\uparrow_1)$. For simplicity, we will assume that the singlet ground state would only involve electrons in the same orbital, as it is also possible to create a singlet using two levels. The index on the $|S\rangle$ formalism notes that both electrons are on the same level. Excitations of the $|S\rangle$ are the following triplets:

$$\left.\begin{aligned} |T\rangle_1 &= (\uparrow_1\uparrow_2) \\ |T\rangle_0 &= \frac{1}{\sqrt{2}}(\uparrow_1\downarrow_2 + \downarrow_1\uparrow_2) \\ |T\rangle_{-1} &= (\downarrow_1\downarrow_2) \end{aligned}\right\} |T\rangle_S$$

These configurations are all degenerate for the $B = 0$ scenario. The indexes 1 and 2 show the level that an electron occupies.

Kondo effect

The interaction of magnetic impurities with metals has been an exciting phenomenon and has aided in the understanding of how magnetic impurities interact with superconductors. Using a quantum dot in close proximity to a metallic lead can trigger that effect.

When a quantum dot is strongly coupled to metallic leads, an interesting phenomenon known as the Kondo effect occurs [18, 19]. The requirements to observe this effect is to be in the intermediate coupling regime at which $\Gamma \sim U$ and to have an oddly occupied level in close proximity to the metal. The basic idea is that co-tunneling processes create spin fluctuations to the quantum level and it turns out that the metal can screen the impurity and form a singlet ground state. To observe this effect, the temperature should be less than a specific value known as Kondo temperature $T < T_{\mathrm{K}}$. For a quantum dot coupled to metallic leads, such level can be an oddly occupied quantum dot which has $|D\rangle$ ground state[citations]. Signature of the Kondo effect, is a zero bias peak that can be observed in bias spectroscopy of $S = \frac{1}{2}$ quantum dots.

Double quantum dots

The above section describes how electron transport operates through a quantum dot connected to metallic leads. We will now explore how that system behaves if there is another quantum dot connected in series with the first one. In analogy with the single quantum dot system, individual plunger gates tune each QD. The couplings between the leads and the QDs are defined by Γ_{L} and Γ_{R}. An essential variable of such a system is the inter-dot coupling t_{d} which is controlled by a barrier gate between the two QDs. This coupling describes how the wave-functions of the two quantum dots overlap, directly affecting the conductance of the system. Figure 2.7 describes the above interactions.

A way of analyzing a double quantum dot system is by using the charge stability diagram, which plots the conductance or the current that passes through the device in the linear bias regime, with respect to the plunger gates that control the quantum dots. As seen in Fig. 2.8a, there are two sets of parallel lines. Each set, represents the charge degeneracy points of each dot. The blue and red circles are degeneracy points of the dot which are controlled by V_{g2} and V_{g1} respectively. In other words, these lines are Coulomb peaks. Following the red (blue) arrow would add electrons in QD1 (QD2) as shown by the charge numbers (n,m). The (0,0), (2,0), (0,2) and (2,2) charge states will have $|S\rangle$ ground state while the (0,1), (1,0), (2,1) and (1,2) a $|D\rangle$. A special case is the (1,1) charge state. The two unpaired electrons of the QDs form a singlet ground state, which is governed by the exchange interaction $J \propto \frac{t_{\mathrm{d}}^2}{U_{\mathrm{d}}}$ between them. In addition, it can be observed that the degeneracy lines of each dot are not perpendicular to the gate axis that controls them, but they have a small angle, indicating that both QDs can be controlled by both electrostatic gates.

The point at which two degeneracy lines meet is called triple point. A triple point represents a degeneracy among three charge states, since both quantum dots are in resonance with the leads. Figure 2.8b shows a circuit describing a DQD which is known as constant interaction model. The tunnel barriers are modeled by capacitors and resistors and the plunger gates are capacitively coupled to the dots. Figure 2.8c shows an example of two triple points, tuning from the (0,0) to the (1,1) charge state. Along the line that connects two triple points, the two quantum dots are in resonance. From such a graph, one can extract U_{d} from the distance between the two triple points. Apart from the constant interaction model description, an electrostatic gate has also an effect to the wavefunction overlap of the two adjacent QDs. This can be described by the inter-dot coupling

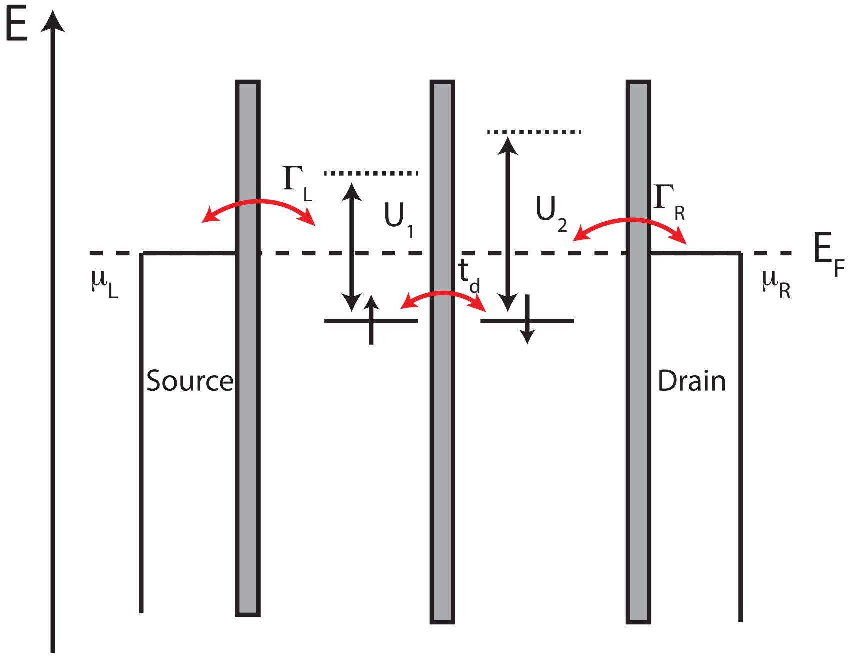

Figure 2.7: Energy diagram of a double quantum dot system. The gray shaded rectangles represent the potential barriers created by the electrostatic gates, which are required to reach the tunnel regime. The red double-arrowed lines represent the coupling $\Gamma_{\mathrm{L(R)}}$ between the source (drain) and the left (right) QD. The inter-dot coupling is described by t_{d}. U_1,U_2 describe stand for charging energies of the left and the right QD respectively.

factor t_{d}, as noted in the previous sections. In the case that t_{d} is finite, then the degeneracy lines tend to curve near the triple points as shown by the red arcs. The distance between a triple point and the arc provides t_{d}. Note, that for high t_{d} that curvature is expanding, effectively leading to a merged single dot system.

In a similar analogy to the Kondo effect in single quantum dots, this effect has also been observed and studied in a DQD geometry [21, 22]. It has been found that by increasing the coupling Γ_{i}, i = L,R, the doublet charge states can be screened and form Kondo singlets. When the electron is coupled with an electron of the second QD through inter-dot coupling, then even larger coupling to the lead is required to overcome t_{d}.

In the next section of this chapter we will discuss a different way of screening impurities by using superconductors instead of metals.

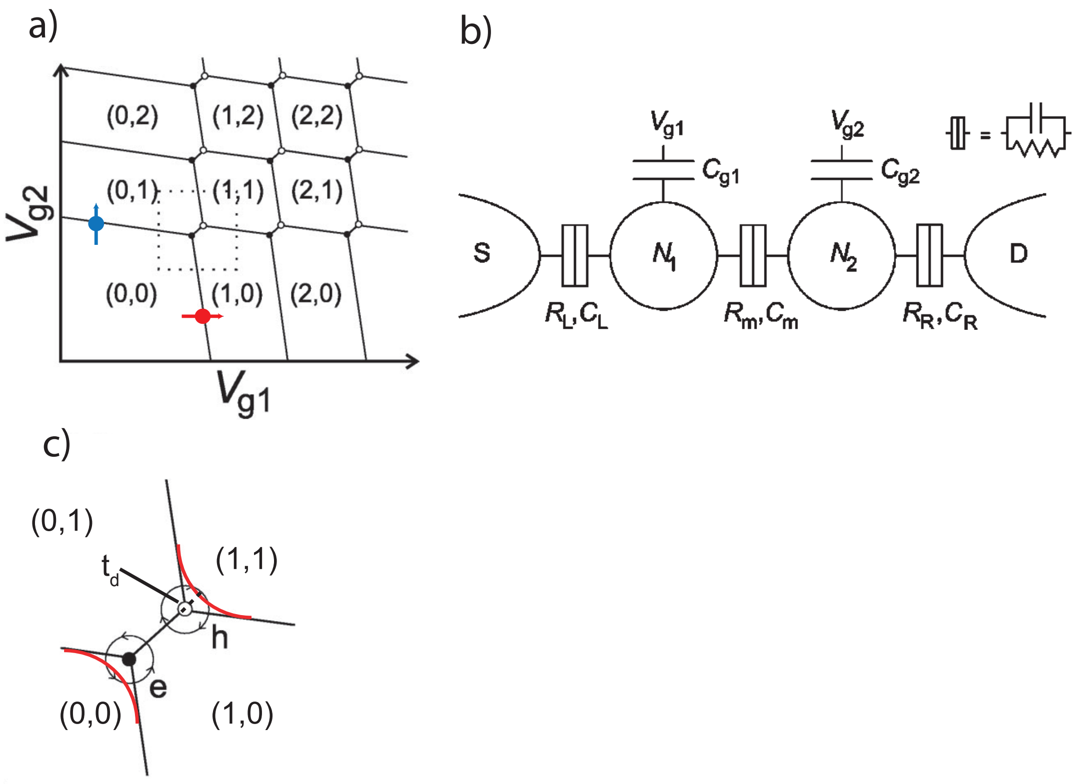

Figure 2.8: a) Charge stability diagram of a typical honeycomb double quantum dot (DQD). Each hexagon represents a Coulomb diamond in which the charge (n,m) remains stable. To add or remove a charge, one should cross through a charge degeneracy (Coulomb peak) to an adjacent hexagon. b) Constant interaction model of quantum dots connected in series. The tunnel barriers required to form a QD behave as capacitors and resistors as shown in the inset. For intermediate inter-dot coupling C_m or C_d, a DQD is formed as shown in a). c) Zoom in area of two triple points. On each triple point three charge states meet. The dashed line shows the magnitude of t_d, while the solid line connecting the two triple points U_d. As t_d increases, the arcs expand, eventually creating a single dot stability diagram. Adapted from [20].

2.4 Hybrid systems

A hybrid system is any system that is consisting of different materials i.e. metal-superconductor. Such geometries, have acquired more attention during the last years due to the topological and exotic phases that can be explored [23, 24]. In the context of this thesis, we are interested in a superconductor - semiconductor - superconductor junction. The following sections provide the basic principles that govern such a physical system.

Josephson Junction

Below, I will introduce the Josephson junction (JJ) that is a setup made of two superconductors separated by a weak link. In the area of electronics, these junctions are used in a wide variety of applications. During this project, we aimed to study a different type of geometry to observe how Cooper pair transport happens in a novel weak link. Hence, we fabricated a double quantum dot system between two superconductors. Before we have the chance to analyze that system, I shall first describe the principles of a Josephson junction.

Embedding a non-superconducting material between two superconductors gives rise to a current flowing through this junction without applying a voltage [25, 26]. This zero bias current is described by the formula $I_s = I_c sin(\phi)$, where $\phi = \phi_2 - \phi_1$ is the difference in phase across the device. This is known as the DC Josephson effect, and for $\frac{\pi}{2}$ phase difference, then the current is equal to I_c which is called Josephson critical current. If a voltage V is maintained across the circuit then the phase difference follows the relation $d(\phi)/dt = 2eV/\hbar$. Hence, an alternating current of amplitude I_c and frequency $f = 2eV/h$ emerges. The energy corresponding to that frequency is $2\,eV$, which is the energy of a Cooper pair that is transferred through the device [26]. This is the AC Josephson effect. A typical Josephson junction is shown in Fig. 2.9.

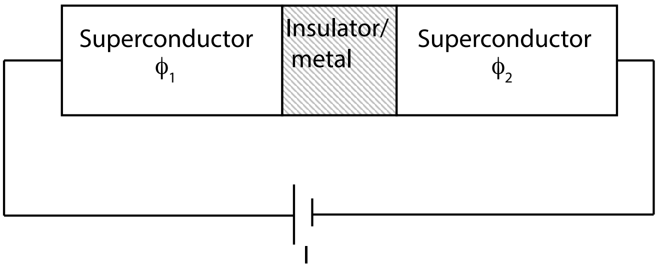

Figure 2.9: Circuit analogy of a Josephson junction. A current biased device of two superconductors with phase ϕ_1 and ϕ_2 are separated by a non superconducting material.

In order to describe a JJ, the resistively and capacitevly shunted junction model (RCSJ) [27, 28, 29] can be summoned. The equivalent diagram of a JJ is shown in Fig. 2.10a. We first start by breaking down the total current I flowing through a Josephson junction, which is given by [30] $I = I_s + I_N + I_D + I_F$. I_s is the Josephson supercurrent written above. I_N is Ohm's law current given by $I_N = GV$, while I_D is the displacement current which is a fictitious current appearing when a capacitor is biased with AC current. Last but not least, I_F is the current related to thermal noise in the junction. From the AC Josephson effect, the above formula can be rewritten to

$$I = I_c sin(\phi) + G_N(V)\frac{\Phi_0}{2\pi}\frac{d\phi}{dt} + C\frac{\Phi_0}{2\pi}\frac{d^2\phi}{dt^2} + I_F \tag{2.1}$$

We can simplify (1.1) by assuming that the conductance is constant $G = \frac{1}{R}$. We then arrive to the RCSJ model. Equation 2.1 can be rewritten as $\frac{\hbar}{2e}C\frac{d^2\phi}{dt^2} + \frac{\hbar}{2e}\frac{1}{R}\frac{d\phi}{dt} + I_c(sin(\phi) - \frac{I}{I_c} + \frac{I_F(t)}{I_c}) = 0$.

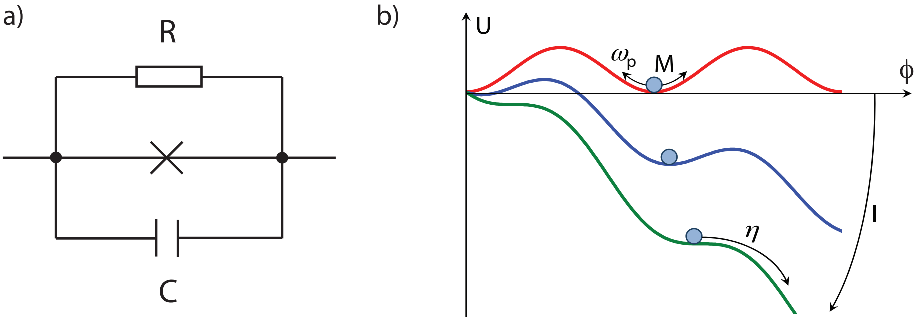

Figure 2.10: a) A circuit scheme of the RCSJ model. The capacitor and the resistor are connected in parallel with the ideal Josephson junction. b) Tilted washboard model for a Josephson junction. For $I = 0$, it is clear that the particle stays at a local minimum(red line), while for $0 \leq I \leq I_c$ (blue line) the particle is sliding downwards but gets stopped by local minima. Nonetheless, quantum tunneling is possible but we are not examining that case. For $I \geq I_c$ (green line) the minima have turned to inflection points. Adapted from [30]

It is possible now to compare this formula with the motion of a particle in a tilted washboard potential. The equation of its motion is given by

$$M\frac{d^2\phi}{dt^2} + \eta\frac{d\phi}{dt} + \frac{d}{d\phi}U(\phi) = 0 \tag{2.2}$$

By comparing eq. 2.1, 2.2 , we can identify the parameters:

- $M = (\frac{\hbar}{2e})C$

- $\eta = (\frac{\hbar}{2e})\frac{1}{R}$
- $U = E_J\left[1 - cos(\phi) - \frac{I}{I_c}\phi + \frac{I_F(t)\phi}{I_c}\right]$

It is clear, that U is the tilted washboard potential. There is a clear analogy between the mass of the particle and the capacitance of a Josephson junction, as well as the dampening and the resistance. On the third bullet point, the Josephson energy is defined as $E_J = (\hbar I_c/2e)$. I_c denotes the fluctuation-free critical current of the model. A scheme of the tilted washboard potential is given in Fig. 2.10b showing U in respect to ϕ for different applied current I. From the last bullet point, one can observe that when $I = 0$ we end up with a simple cosine function, with the particle being trapped in a local minimum. As the current increases, the slope of potential increases. If $I \geq I_c$, U has no longer local minima but instead inflection points. Hence, no stable point for the particle exists, meaning that the junction is no longer in the supercurrent regime, but has passed to the trivial linear I-V characteristic. However, the behaviour of a Josephson junction for $I \leq I_c$ varies depending to the quality factor which is given by $Q = \omega_p RC$, with $\omega_p = \sqrt{(2eI_c/\hbar C)}$ which is the plasma frequency. This factor determines if the junction is overdamped or underdamped.

- For $Q \gg 1$ the junction is underdamped due to high capacitance and/or resistance
- For $Q \ll 1$ the junction is overdamped due to low capacitance and/or resistance

For the overdamped case, the mass of the particle is small and the dampening is large. Moreover, as the resistance is low the inertia η is high. That means that the particle is more likely to stabilize faster on a local minimum. As a result, the phase of the Josephson junction will also stop evolving and the junction will return to the zero voltage state. When there is weak dampening, then the mass of the particle is large and in combination with the small dampening factor η, it makes the particle slide to the next local minima. Large reduction of the applied current (lower slope of the washboard potential) is required in order to stop the particle and return the Josephson junction to the zero voltage state. These features of the underdamped junction cause an interesting asymmetry in the I-V characteristic as seen in Fig. 2.11b. Starting from $I \geq I_c$, the junction is fully on the Ohmic phase and it requires the applied current to be set to zero in order to return in the supercurrent regime. The overdamped case shown in Fig. 2.11a has a symmetric I-V curve thanks to the small kinetic energy of the particle which allows it to stabilize on a local minimum when the current is reduced to $I \leq I_c$ [30].

We now consider thermal fluctuations in the model. To get an intuition, at the limit $k_B T \gg E_J$ it is possible for a particle to hop from one minimum to another due to thermal activation. In combination with the overdamped regime, this creates some interesting variations. Specifically, for $I \leq I_c$, the particle can be thermally activated and overcome the barriers of the washboard potential [28, 26]. Moreover, the presence of thermal fluctuations makes the theoretically divergent conductance of supercurrent converge at a finite value.

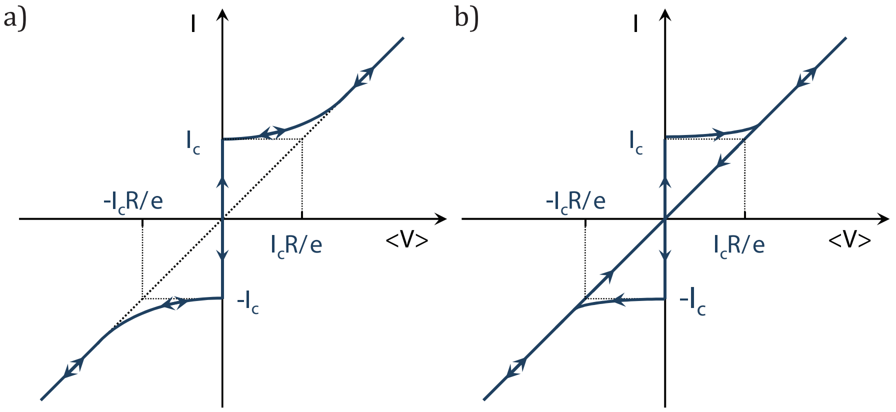

Figure 2.11: I-V characteristic curves for the a) overdamped and the b) underdamped case. a) The I-V curve is independent to the sweeping direction of the applied current. The supercurrent behaviour is clear for $|I| \leq |I_c|$ and the junction has an Ohmic behaviour after that. b) Depending on which direction the current is swept, the image of the I-V characteristic shifts, creating an asymmetric picture. Adapted from [30].

Quantum dots coupled to superconductors

By combining superconducting leads with quantum dots, one can design a superconductor - quantum dot - superconductor (S-QD-S) device geometry. Such a system is a perfect tool for studying the behaviour of Josephson current that would flow through that device. However, depending of the relation of the energy scales, various regimes which have different behaviour can be studied.

If $\Gamma \gg U$ then the effective probe of the leads is broadened, and we are in the resonant tunnelling regime [7], on which supercurrent can be measured. On the other limit when $\Gamma \ll \Delta$ then the supercurrent is suppressed and depending on the occupation of the QD, $0 \longrightarrow \pi$ transition can be observed in the current phase relation of the supercurrent [29, 31].

Supercurrent reversal

Experiments during the last decades [7, 29] have demonstrated that in S-QD-S devices in which supercurrent can be measured, the occupancy of the dot affects the sign of the supercurrent, owing to a π-shift in the Josephson relation. We can visualize the process of Cooper pair transport in such a system through annihilation and creation operations of spins. The idea is that if there is a Cooper pair in the source and we want to transfer it to the drain, that can be simply written with creation and annihilation operators as : $c_{\uparrow}^{\dagger} c_{\downarrow}^{\dagger} c_{\downarrow} c_{\uparrow}$, where $c^{(\dagger)}$ annihilates (creates) an electron. For the simple case when the dot has even number of electrons, the process of creating a Cooper pair in the drain can be described by the above operations. This maintains the sign of the supercurrent

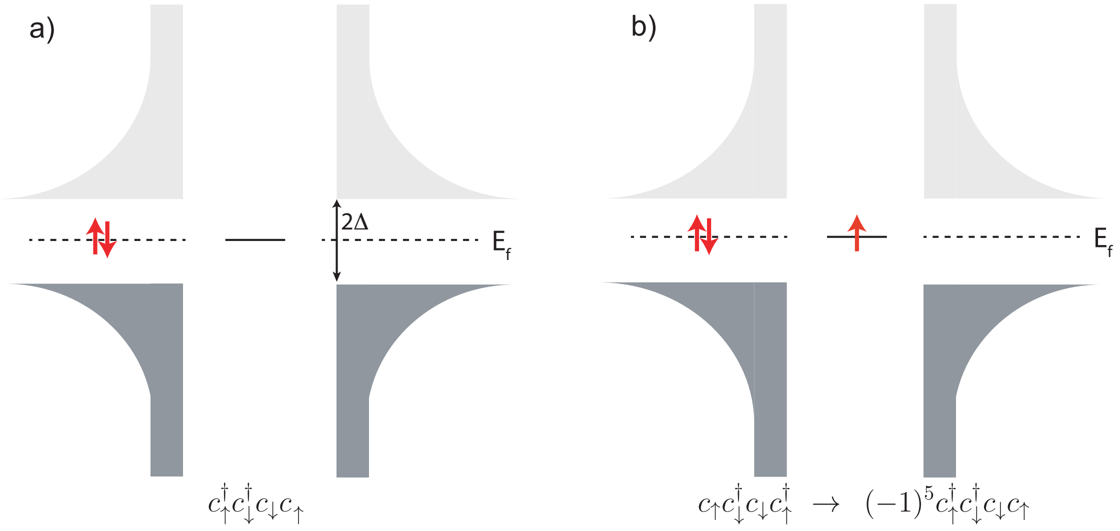

Figure 2.12: a) Cooper pair transport through a single level, evenly occupied quantum dot. The operations required to transfer a Cooper pair across is noted below the figure. b) Transport through an oddly occupied quantum dot. The same sequence of operations as in a) cannot be done because the electron occupying the dot prevents another spin up particle to jump on the level. The operations are now $c_\uparrow c_\downarrow^\dagger c_\downarrow c_\uparrow^\dagger \left|0\right\rangle$ which require 5 permutations to be written as the starting format. Since electrons are fermions, each anticommutation spawns a negative sign on the outcome.

through the device, which is called a 0 junction. That process can be viewed in Fig. 2.12a.

However, if the QD has an odd number of electrons as seen in Fig. 2.12b, the spin-ordering of the supercurrent is reversed, leading to an acquisition of a negative sign. That occurs because, if there is an electron in the dot, then due to Pauli's exclusion principle the operations $c_\uparrow^\dagger c_\downarrow^\dagger c_\downarrow c_\uparrow$ are invalid. A total of 6 different transport sequences can happen, which all involve an odd number of permutations. Fig. 2.12b shows one of the six cases. Initially, the spin up electron is created on the right lead, then the spin down is annihilated on the left, followed by the creating of the spin down on the right lead. The last operation is the annihilation of the spin up electron on the lead in order to have the same picture as the starting one. Five permutations are required to reach the starting state, which provide the negative sign $c_\uparrow c_\downarrow^\dagger c_\downarrow c_\uparrow^\dagger \rightarrow (-1)^5 c_\uparrow^\dagger c_\downarrow^\dagger c_\downarrow c_\uparrow$. We name that sign change a π-shift in the current phase relation $I_s = I_c sin(\phi + \pi)$, which leads to negative supercurrent. Interestingly, it can be shown that the global ground state of the system is the cause of π shifts. When a QD has even number of electrons the ground state of the system would be a $\left|S\right\rangle$, while for odd number there is a doublet ground state $\left|D\right\rangle$. In the analysis chapter we will explore whether the addition of a second QD in series would alter the behaviour of the supercurrent.

Screening regime

The physics of superconductors in close proximity to magnetic impurities had been studied extensively by Yu, Shiba and Rusinov [1, 2, 3]. In recent years, advances in technology have allowed the fabrication of nanoscaled devices with the aim of observing and studying the sub-gap states that are created in the superconducting gap, due to the interaction of a superconductor with a magnetic moment. Scanning Tunnel Microscope (STM) experiments in single atoms such as Ni [32] have shown signatures of these sub-gap states, as well as transport experiments involving quantum dots which are coupled to superconductors [14].

Assume that we have a system with a quantum dot embedded between two superconducting leads. Let the quantum dot have odd number of electrons, giving it spin $\frac{1}{2}$. If the conditions $\Delta \ll U$, $\Gamma \sim U$ are satisfied, then screening of the spin can occur[1]. As the tunnel coupling is increased, then it becomes more favorable for the superconductor to screen the impurity and form a singlet ground state $|S_{YSR}\rangle$. That happens because the excited state of the $|D\rangle$ crosses zero energy and eventually becomes the ground state. On the other hand, if the coupling is weak, then the ground state does not change and it remains a degenerate $|D\rangle$. The above cases can be visualised in Fig. 2.13 [5]. The ground state of the system is influenced not only by the QD occupation, but also by the coupling. Γ_A describes the case on which the coupling to the superconductor has caused a shrinking of the $|D\rangle$ area. On the other hand, Γ_B is sufficient enough to tune the QD to a region where it is $|S\rangle$ for even and odd QD occupation.

Experiments demonstrating the tuning of sub-gap states in S-QD-S device [5] are shown in Fig. 2.13b,c. The sub-gap states are crossing zero bias when there is a ground state transition, $|S\rangle \rightarrow |D\rangle$. However, for larger coupling Γ_B, the $|D\rangle$ region has vanished and the sub-gap states are anti-crossing, hinting that the ground state is the same for all three charge sectors.

---

[1] Note that this limit is known as Yu-Shiba-Rusinov screening, which we examine in this project. For $\Delta \gg U$ then the sub-gap states are known as Andreev bound states (ABS). There, a hybridization of no spin in the QD ($|0\rangle$) and doubly occupied QD ($|\uparrow\downarrow\rangle$) becomes the ground state [33].

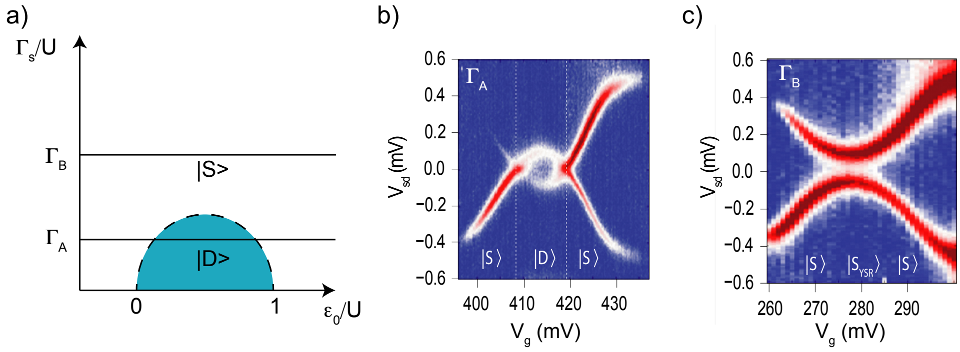

Figure 2.13: Phase diagram showing on the x axis the occupation of the QD normalized with the charging energy U, while the y axis describes the coupling to the superconductor normalized to U. As Γ increases, then the area at which an oddly occupied dot has a $|D\rangle$ ground state shrinks. It is observed that for high enough coupling, the system has a $|S\rangle$ ground state independently to the dot occupation. b) Sub-gap states spectroscopy demonstrating gate dispersion over a source-drain bias. At a finite coupling, the $|D\rangle$ region is well defined. c) For larger coupling, the sub-gap states anti-cross hinting a ground state transition $|D\rangle \rightarrow |S\rangle$. Adapted from [5].

Chapter 3

Fabrication and measurement setup

In this chapter, the process of creating the nanowire based devices is reported. The first sections will cover the substrate preparation of the samples. Furthermore, the nanowire deposition and contacting of the nanowires will be explained. The goal of the following fabrication procedure was to create a double quantum dot system with superconducting contacts as source and drain. This device would allow us to explore various regimes of a double quantum dot, by studying the coupling dependence Γ, as well as explore the supercurrent through that peculiar Josephson junction. A detailed description of the fabrication recipes can be found in the Appendix B of the thesis. The final part of the chapter contains a summary of the measurement configuration and of the dilution refrigerator used for the experiments.

3.1 Sample Fabrication

In this section we will go through the steps of fabricating the device, from the substrate cleaving to the final step of bonding the chip and connecting it to the QDev chip carrier.

Substrate Preparation

To start with, I shall describe briefly the concept of lithography and the techniques used to create microscopic devices in the nanoscale. Electron beam lithography (EBL) is a technique that transfers a pattern from a design program onto a silicon or other substrate, by employing a focused beam of electrons. The process of lithography and metalization -or etching- is illustrated in Fig. 3.1. By spin-coating a resist on top of the wafer, typically Poly(methyl methacrylate) (PMMA), we can then use a focused electron beam to break the polymer chains in the desired pattern. The areas with the broken chains are now fragile, and by using a developer solution (typically MIBK:IPA 1:3) it is possible to remove these areas and form a cast. As seen in Fig. 3.1, etching of the unprotected wafer or metal evaporation can be achieved. Finally, the removal of the leftover resist is performed.

The exact fabrication recipe is noted in Appendix. Most of the following fabrication steps follow the above procedure.

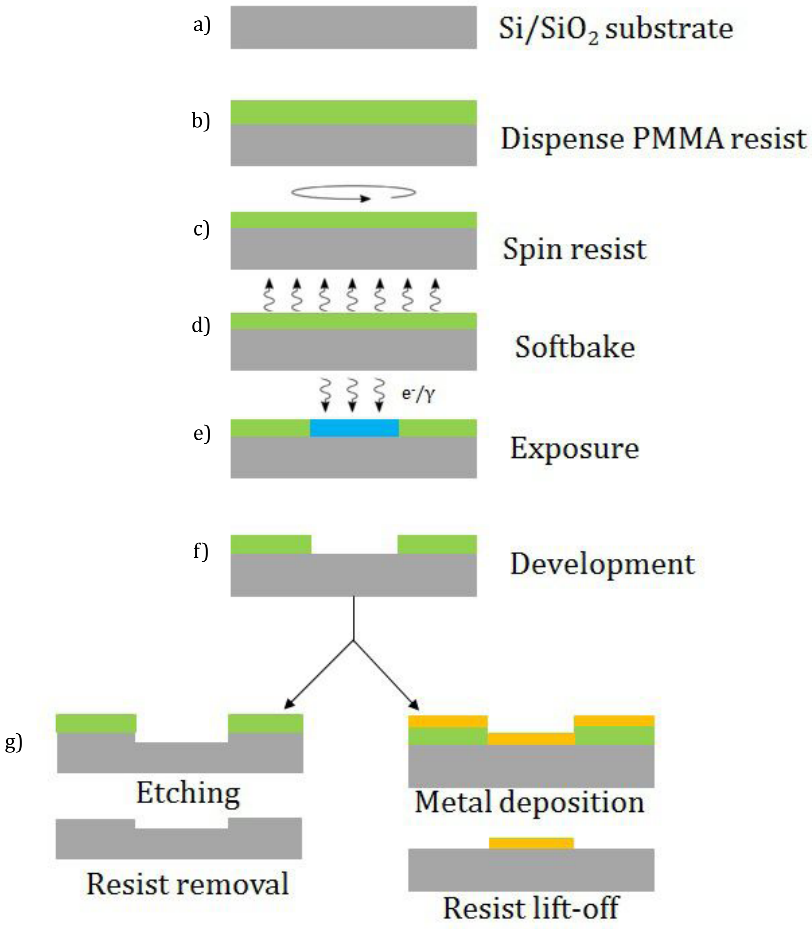

Figure 3.1: Principles of electron beam lithography. a) a Si/SiO$_2$ substrate is cleaned with Isopropyl alcohol (IPA) and acetone before processing. b) A PMMA resist is dispensed on the substrate followed by c) spin-coating. d) Baking the substrate for a few minutes ensures that the liquid turns into a glass-like material. e) EBL or UV exposure of the desired design. f) A specific chemical is then used to dissolve the resist that has been exposed and form the design. g) The last step is either metal evaporation of the design or selective wet etching of the substrate. [adapted from cleanroom nbi]

The substrates that we used were highly doped Si with a 200 nm thick SiO$_2$. 2-inch sized wafers were cleaved using a manual scriber into 15x15 mm^2 squares. A square of such dimensions could be cut into 9 smaller pieces of 5x5 mm^2 surface area. Each of these, would function as a sample on which the next fabrication steps would build upon.

To expose coarse features, we used a Heidelberg μPG 501 ultraviolet (UV) lithography instrument. The ability to expose faster than EBL makes this process vital in the fabrication of objects larger than 1 μm. Due to the diffraction limit of light, UV lithography is unable to expose smaller features with the desired accuracy. Thus, we use EBL for fine features such as contacts and gates of devices. Figure 3.2 illustrates the base design for the outer leads which were exposed using a UV lithography system. Alignment marks were also exposed on the same lithography step to align the following exposures.

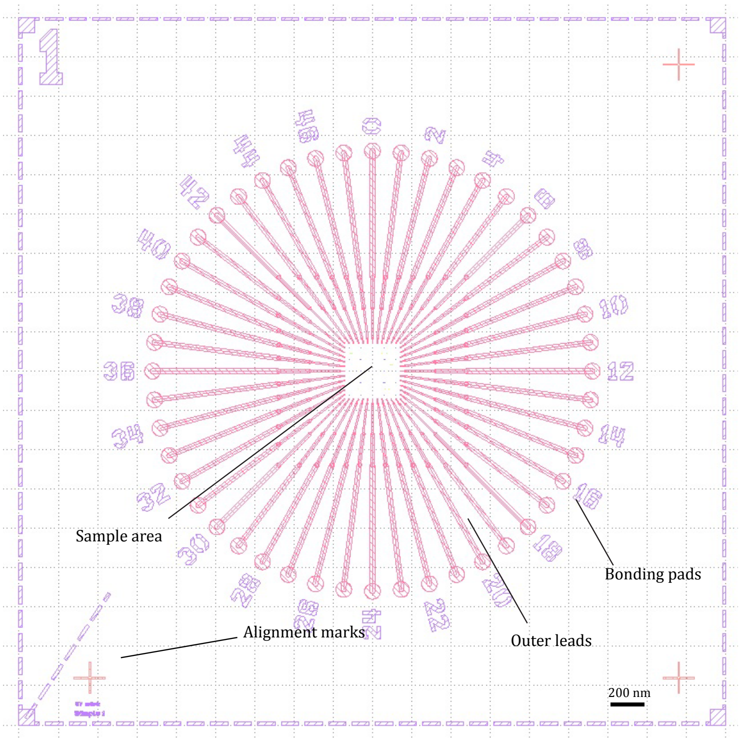

Figure 3.2: Base design made with UV lithography. On the corners the three alignment marks are shown which are used for the following exposures. The outer leads are in a circular pattern to make bonding of the chip less cumbersome. The bonding of the chip is done on the circular end of the leads (bonding pads).

The next step was to create the bottom gates which will define the barriers needed, to form the quantum dots on the nanowires. The width of the bottom gates is 20 nm and the pitch 60 nm. This stems from the fact that we want to confine as small quantum dots as possible in order to have large charging energy U and be able to observe shell filling. On each chip a total number of sixty four (64) sets of bottom gates were exposed using electron beam lithography. A Scanning Electron Microscopy (SEM) image of the bottom gates can be viewed in Fig. 3.3. The complete recipe followed to create the bottom gates can be found in Appendix B.3.

To isolate the metallic gates from the semiconducting nanowire, which will be deposited on top of them, a dielectric layer of HfO_2 is deposited via atomic layer deposition on the bottom gates. On the samples measured, two layers of 10 nm each were deposited by my group members, using a Cambridge ALD instrument. High quality of dielectric is essential to provide stability in

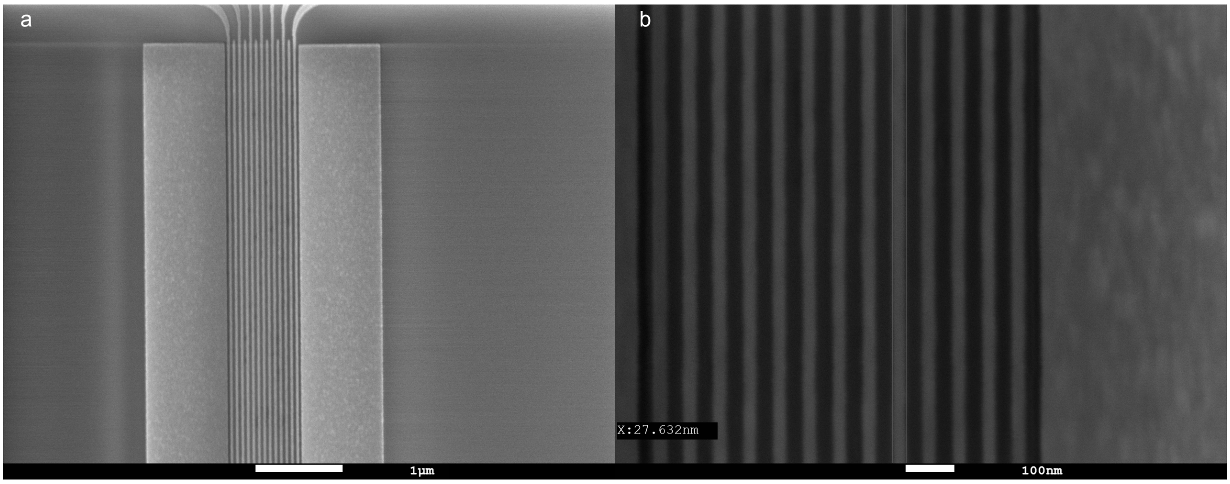

Figure 3.3: a) SEM image of a set of bottom gates. Out of the 13 bottom gates, the 5 central of them are selected to contact in order to define the double quantum dot on the nanowire. The contacting of the gates is being made from the exceeding parts. Half of the gates are leading to the top side of the set, while the rest to the bottom as seen in the image.b) a closer look to the bottom gates. Their width can be measured to be around 27.5 nm.

measurements and minimum leakage of the electrostatic gates. In the case that water or other substances are trapped between the gates and the dielectric layer, these molecules could charge up when voltage will be applied on a gate. As a result, this phenomenon could cause perturbations in the stability of the device.

Nanowire Deposition and Processing

After the base substrate is configured, deposition of nanowires follows. This subsection will cover the fabrication steps towards a superconductor - double quantum dot -superconductor (S-DQD-S) device. To achieve that, the nanowires were deposited with a 90 °angle to the bottom gates. The instrument used to conduct the nanowire deposition is an *eppendorf TransferMan 4r* micromanipulator. The idea is that by using a microscope and a needle, which is controlled in x,y and z direction by a joystick, one can pick up a nanowire lying on the nanowire-growth wafer and through Van der Waals forces, attach the nanowire to the needle. By moving the needle with caution it is possible to gently deposit the nanowire on the desired surface. It is important to deposit the nanowires as smoothly as possible to prevent any damage on the dielectric. It is also recommended not to move the nanowires with the needle after they have been deposited since that can cause bending, and damage to the crystal. In the case that the nanowire is bend or one of its sides is not completely touching the surface there is the chance that after metal deposition, the contacts break. That happens due to the strain of the nanowire.

A challenging part of fabrication was the etching of the epitaxial aluminium. The nanowires we are using are InAs with three of the six facets covered by a 7 nm layer of aluminium, epitaxially grown in the molecular beam epitaxy chamber. Hence, to electrostatically control an area of the semiconductor and form the quantum dots, it is required to remove the superconducting metal in a length of 330 nm along the wire. On the other hand, it is not wise to remove a large length of the aluminium shell because the shell itself acts as source and drain contacts. That means that the closer the two superconducting leads are, the better the superconducting properties of the device i.e. hard gap and Josephson supercurrent. To selectively remove the aluminium from the nanowire, a resist is spin coated on the sample and an EBL exposure follows exposing only the area that is to be etched. This way it is possible to remove the metallic shell of specific length by dipping the sample in the acid Transene - D for 9 seconds at 50^o C. Several recipes were tested before optimizing the results. The main issue was the fact that the etchant solution would not only remove the metal on the developed area of the chip, but it would also pass below the PMMA resist and eventually etch a much larger area. The over-etching estimation for this recipe was around 50%. To overcome this problem a different resist was used which has better adhesion, the copolymer Ethyl-Lactate, which is basically PMMA in Ethyl-Lactate solution and not in Anisole. With this resist, in combination with decreasing the exposed area to be etched, we achieved consistent etched windows in the desired length of around 330 nm. Figure 3.4 shows two etched nanowires, the right with the EL resist and a 287 nm etch window, and the left with PMMA in asinole and 512 nm etch window. The light gray colour is the epitaxial aluminum and the etched gap is clearly seen. The over-etching on Fig. 3.4b is estimated to be around 25 nm on each side, while on Fig. 3.4a around 100 nm for each side. The difference between the two recipes is significant. In some cases, instead of a continuous aluminium film, grains were observed. A speculation is that these grains could

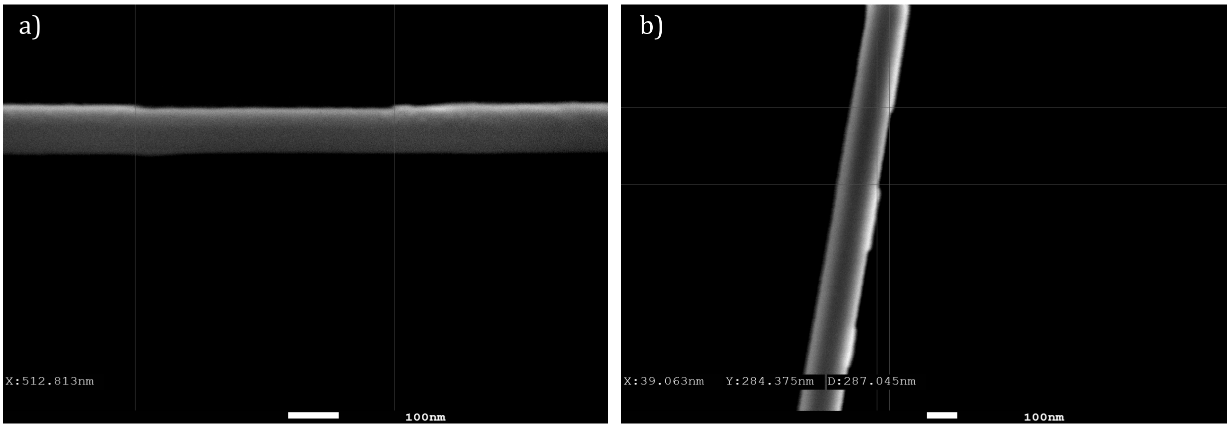

Figure 3.4: SEM images of etched aluminium shell in InAs nanowires. a) The light gray color is the non-etched aluminum. The etched window is clearly measured to be 512 nm in length, hence the over-etching on this nanowire makes it unable to use for double quantum dot devices, because the superconducting effects will be impaired due to the large distance of the two leads. b) Successful etching of the epitaxial shell. The 287 nm channel can be tuned using 5 or 6 bottom gates and define superconducting quantum dots.

affect transport properties, in particular superconducting effects of the aluminium, such as the presence of hard gap.

Contacting the nanowires with source and drain leads had been a rather interesting part. After the nanowires have been deposited and etched, an EBL exposure of the leads takes place. Typically the mininum number of bonding pads required for a S-DQD-S device is 7, two for source drain and 5 for the bottom gates below the etched channel. 5 nm of titanium and 200 nm of gold were evaporated to ensure that the nanowire is properly contacted. The purpose of titanium is to provide a sticking layer for the gold to attach and be stable metallic piece. However, by simply depositing Ti/Au on top of the Al-InAs nanowire does not provide good contact because a native aluminum oxide and InAs oxide form on the surface of the nanowire on contact with air. Hence, by evaporating metal on top of that oxide shell would not make a good ohmic contact, but a tunnel junction that cannot be used as source or drain. To cope with this problem, the metal deposition chamber is equipped with an argon milling system. While the sample is loaded in the evaporation chamber - and still being in vacuum- argon milling is performed to remove the oxides and provide a good interface for the upcoming metal. Right after the milling, the evaporation takes place, preventing the nanowire from forming a new oxide layer. Fig. 3.5 shows an SEM image of a device.

An important step of the device processing is the removal or lift-off of the remaining resist that covers the substrate, after the evaporation is complete. Placing the sample in hot bath in N-Methyl-2-pyrrolidone (NMP) helps to dissolve the PMMA resist. However, sometimes the lift-off process can be cumbersome and the leftover resist might not dissolve. There are several ways to enhance the lift-off process. Sonication at low frequency and power could be used

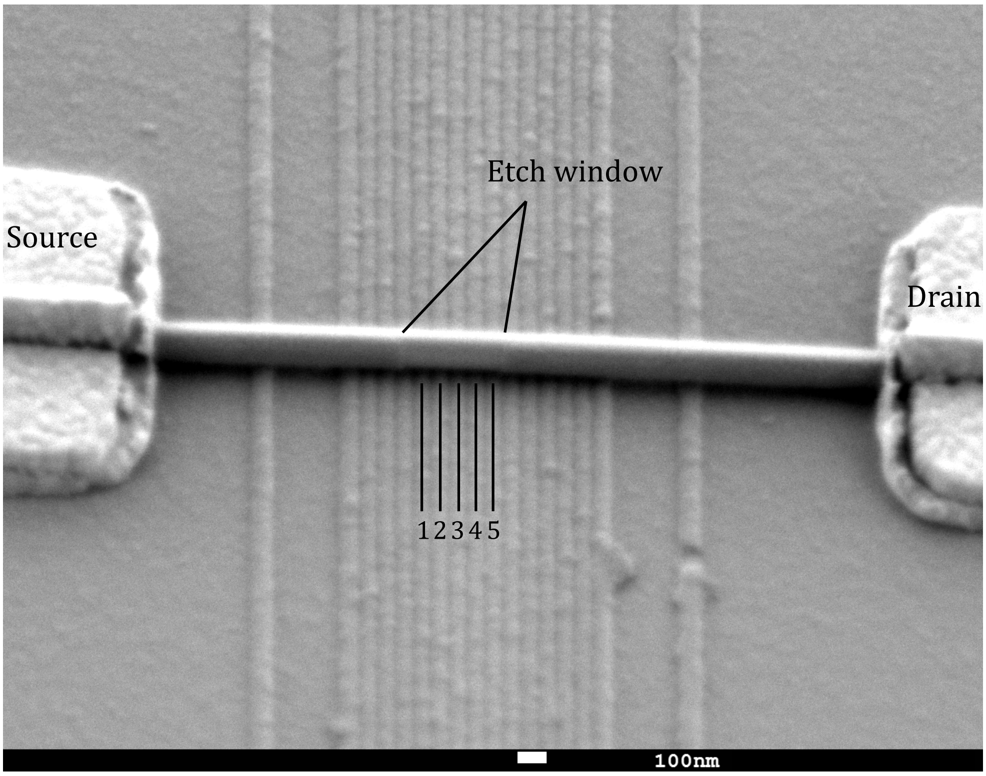

Figure 3.5: An SEM image of a working S-DQD-S device. It should be noted that these substrates were designed for more complex devices such as Cooper pair splitters, and that is why they have more bottom gates. On our experiments, we left the unused bottom gates floating. The source and drain electrodes are made of evaporated Ti/Au. The epitaxial aluminum is selectively etched from the central region, creating a Josephson junction with the aluminum shell on each side acting as superconducting lead.

to enhance NMP's outcome, though I do not recommend it because it damages the nanowires. Alternatively, I used PMMA resist with lower molecular weight, which makes lift-off faster.

A crucial problem that emerged is too thin metal deposition which caused bad or no contact to the nanowires. A typical diameter of the nanowires we used for these devices is 120-130 nm. As a result, the total evaporated metal that is deposited should be at capable of holding the nanowire in place, overwhelming the tension forces and stress. We found out that at least 185 nm of metal should be deposited to assure that there is good contact between the metal and the nanowire. Figure 3.6 shows a poorly contacted device.

The final step of device fabrication is to connect the contacts via the outer large leads with the outside world. By glueing the sample on a 'daughterboard' seen in Fig. 3.7a, we can connect the bonding pads with the pins of the board using a bonder. After that procedure is complete, we may install the board to the special puck of the dilution refrigerator and load it to the load lock. Figure 3.7b illustrates the puck that we are using for our measurements.

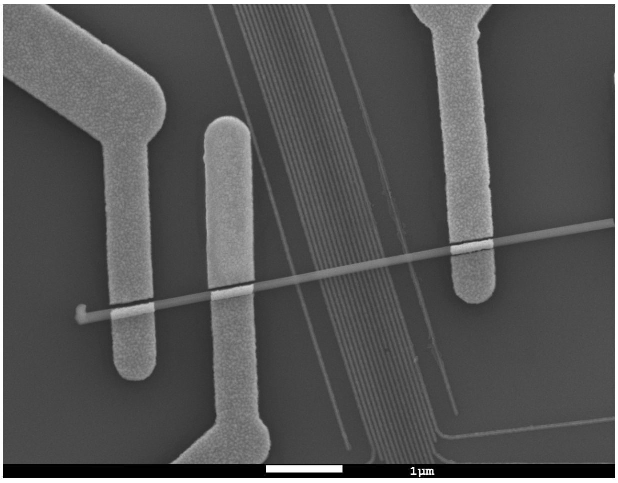

Figure 3.6: An SEM image of badly contacted device. A gap is clearly visible at the points of contact between the metallic leads and the nanowire. After the metal deposition and lift-off took place, the nanowire broke the leads causing to insufficient contacting.

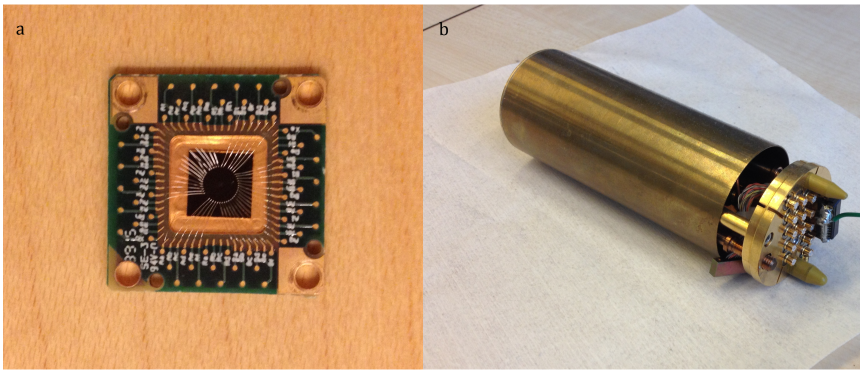

Figure 3.7: a) A photograph of a bonded device on a QDev Daughterboard. Aluminum wire was used to connect the bonding pads with the board pins. b) An image of the puck which holds inside the sample. A nanoD adapter connects the pins with the cables of the dilution unit.

A disadvantage of using nanowires as semiconducting channels, is the fact that they are quite sensitive and fragile to sudden voltage changes. By not being properly grounded while handing a nanowire based device, or placing it on an instrument that is not grounded, enhances the possibility of electrical shock. If it is floating (not grounded) it may accumulate charge from the environment, forming a potential. Mounting the device in the dilution refrigerator after that event causes it to be near a different voltage and this sudden change can run a high current through the nanowire, eventually damaging and possibly destroying the device. In order to increase the yield, we made sure that the devices are properly grounded while we are bonding them to the boarding chips. After the bonding of a sample is complete, we load it to a Faraday cage which has been grounded. The box used for this step is illustrated on Fig. 3.8a.

The goal of this procedure is to maintain the potential of the sample minumum (grounded)

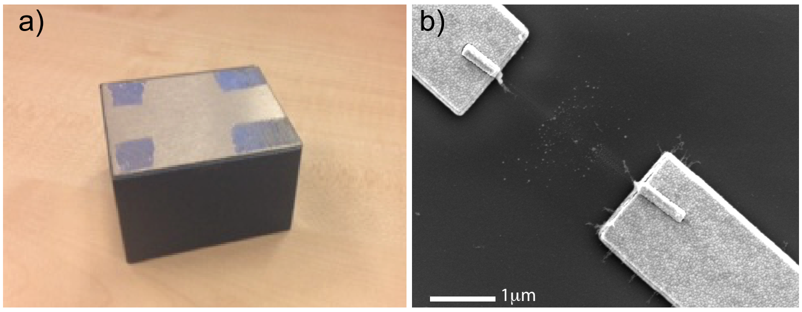

Figure 3.8: a) The box on which the sample is carried from the bonding instrument to the loading on the puck. The fact that it is made of metal serves as a protection to external electromagnetic fields. b) An SEM image of a destroyed device. A significant voltage different between source and drain (thereby creating a current), caused the nanowire to blow up leaving only the contacted area intact.

while it is transferred from the bonding machine to the puck, and finally to the load lock. During the loading process, we found out that it is important to use the same ground for both the load lock and the sample which is mounted on the puck, to minimize the chances of experiences voltage differences. By systematically following these steps and being always grounded while handling a sample, we had our device yield increase. An SEM image of a damaged device is demonstrated in Fig. 3.8b.

3.2 Experimental Setup

This section includes the description of the dilution refrigerator that was used to perform the experiment at low temperatures, as well as the setup of the voltage supply instruments used to measure the devices.

The Dilution Refrigerator

In the area of condensed matter physics the energy scales play an important role at how a system will behave. A quantum dot for instance, is defined by the charging energy, which is the value that determines how much energy the dots needs to ”host” another electron. That energy can be given by any means, voltage bias or even thermal energy by the environment. At room temperature, $k_B T$, or thermal energy, would be the dominant energy scale, because the values of charging energy are in the order of few meV, while the thermal energy is 25 meV.
We can now understand the importance of diminishing the thermal energy by installing the device in a 20 mK base temperature refrigerator. Low temperatures allow us to study quantum phenomena which are obscured at normal circumstances.

The fundamental circuit of a dilution refrigerator can be viewed in Fig. 3.9. Figure 3.9a shows the different temperature plates that a dilution refrigerator has. The process of ^{3}He diluting in ^{4}He drains heat from the environment and provides cooling power to the so called mixing chamber. That happens because the entropy increases when the dilution happens, thus absorbing heat. To have an equilibrium between the two volumes of He isotopes, a 6.6% of ^{3}He should be diluted. To exploit this phenomenon, a pump can be used to drain the mixture and disturb the equilibrium, eventually causing more ^{3}He to dilute. Another main component of the dilution unit is the still. After the mixture has been pumped, it has to be distilled in order to extract the diluted isotope and send it again to the mixing chamber to dilute. That process is achieved by using a heat source to evaporate it. The above is illustrated in Fig. 3.9b. The base temperature of a dilution refrigerator is 25 mK. Lower values are practically impossible to get due to the thermal boundary resistance that increases in a cubic dependence with temperature, and prevents heat transfer within the dilution refrigerator.

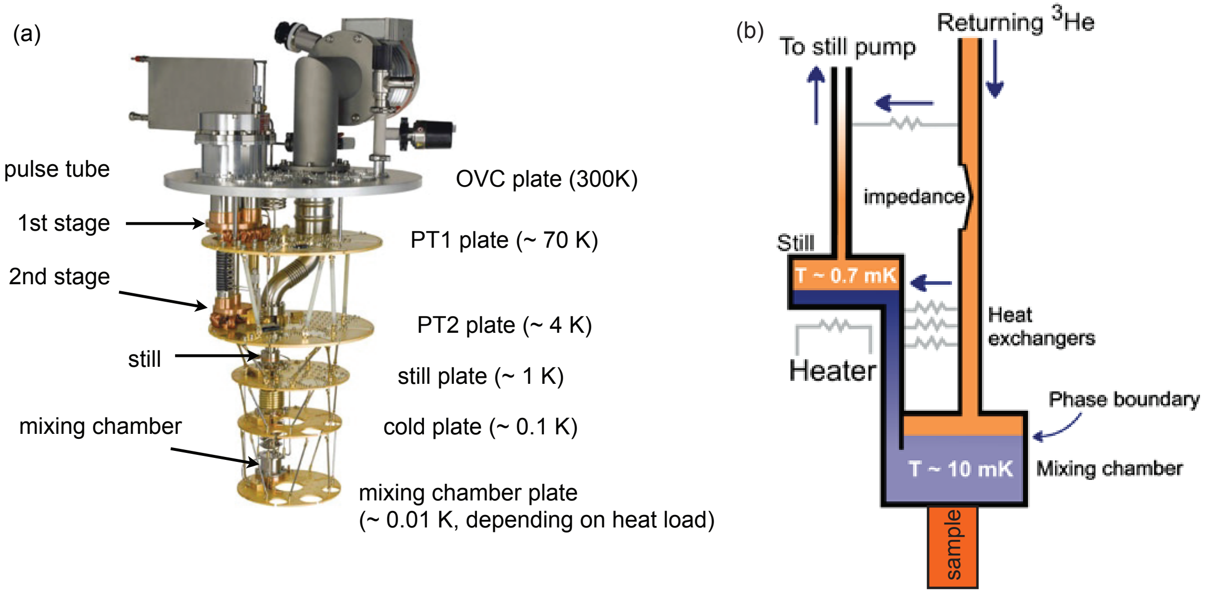

Figure 3.9: a) An image of how the dilution refrigerator looks without the radiation shields. From top to bottom, the different cold plates can be seen with their according temperatures when the refrigerator is at base temperature. b) A sketch of the operation of the lower parts of the dilution unit when the mixture is circulating. ^{3}He is diluting to ^{4}He and the mixture is pumped to the still to trigger further dilution, and cooling down of the sample space. Adapted from [34].

Measurement Setup

An essential part of the project was the measurement of the current and differential conductance of the devices. To successfully do that, a wide range of instruments were used to send signal to the nanowire based devices, amplify the current received, convert to conductance, and of course control the voltage values of the bottom gates. The complete instrument setup is depicted in Fig. 3.9. A lock-in amplifier produces an AC voltage, while a digital to analog converter (DAC) produces the DC component. The two signals are then divided by 10^4 and 10^3 respectively, to create an excitation not larger than the thermal noise $k_B T$ and allow the study of the device in small voltage fluctuations. The combined signals enters the breakout box and finally reaches the electrode noted with S, after it has passed by a series of RC filters in the cryostat. Furthermore, as the signal transfers through the device, it moves from the breakout box to a current amplifier which amplifies the voltage by 10^8 and converts it to current. The amplification is essential as the signal is very faint and it would be difficult to distinguish from noise. A digital multimeter (DMM) is used to measure the AC component of the current while the lock-in amplifier measures the DC component we use to extract the differential conductance. To control the voltage of the gates, a DAC was used to supply DC voltage for each gate separately. The model we were using is a 16 bit DAC, which is translated to a resolution of 300 μV. The higher the resolution, the better since it allows fine tuning of a delicate device such as a double quantum dot.

Such measurements would be inaccurate without the usage of a lock-in amplifier. This tool is used as an AC waveform generator that sends a signal to the measured device, having a frequency f. When the excitation reaches the dilution unit, it will trigger a series of waves of various signals. A lock-in relies in the orthogonality of sinusoidal functions. When a sinus of frequency f_1 is multiplied with a sinus of frequency f_2 and integrated over a certain time the product will be zero unless f_1=f_2. Hence, all the not desired signals are discarded and we end up with a DC signal which has the same frequency as the reference.

The acquisition software that we used to extract and analyze data is Matlab-qd, a program designed in the University of Copenhagen for high level communication and control of various instruments including the dilution unit, deca DACs and the superconducting magnet. Using that program, we could extract the values measured by the instruments, as well as control the voltages of the bottom gates and the source-drain bias. With that data the differential conductance was calculated.

The communication between the computer and the instruments is carried out by using the General Purpose Interface Bus (GPIB), which is an interface system that allows communication among several devices [35]. By using that protocol we could control the DAC, Keithley DC voltage source, lock-in amplifiers, Agilent DC current supply as well as the superconducting magnet and the cryostat temperature from one computer.

For easier data plotting, we used a python program ‘Folderbrowser’ designed by a former PhD student in the group.

Typically a sample would have several devices so a way to boost the speed of testing and studying them, we developed a twin measurement setup that allowed us to measure simultaneously two devices using the same dilution unit.

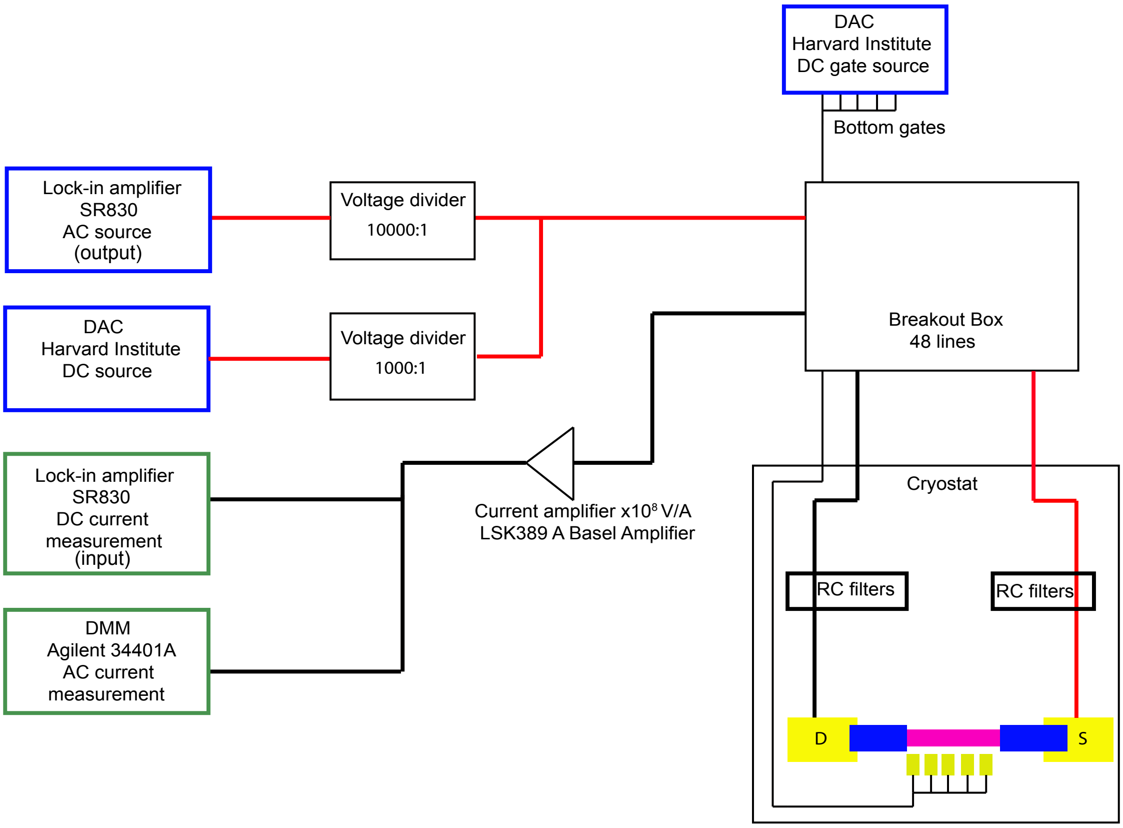

Figure 3.10: The measurement setup. A DC signal which is supplied from a DAC and a AC signal from a lock-in waveform generator and both divided before arriving to the sample. The RC filters equipped in the lines of the fridge have a series resistance of $R_s = 4.12\,k\Omega$. The signal from the drain electrode is then amplified in order to be distinguished from noise. The model that we used was a LSK389A Physics Basel current amplifier. The signal is then measured by a DMM Agilent 34401A for the AC component and by a SR830 lock-in amplifier for the DC component. The gates that control the electric field locally are also controlled a 16bit DAC.

Chapter 4

Supercurrent through a Double Quantum dot

4.1 Introduction

Embedding a non superconducting material (weak link) between two superconductors triggers a current that flows through that device without any applied voltage. This device geometry is known as a Josephson junction [25]. Josephson junctions have been studied extensively the latest years, with a focus on one-dimensional materials employed as weak links, such as carbon nanotubes or nanowires [36]. Recent experiments[29, 7] involving single quantum dots coupled to superconductors have shown that the total spin of the system affects the current phase relation of the supercurrent $I = I_c \cdot sin(\phi + \phi_0)$, modifying its sign. In our project, we defined a double quantum dot system embedded between two superconducting leads (S), creating a tunable two magnetic impurity system. This geometry is interesting, since by changing the occupancy of the dots one can trace the shifts of the critical current I_c, providing the option of changing the phase of the supercurrent on demand. This chapter will cover the first-ever reported set of supercurrent measurements through a serial double quantum dot (DQD) defined in a nanowire.

My personal contribution to this work was to fabricate the device that was used, as described in the fabrication chapter. Additionally, I was part of a team of two people that handled the loading of the device to the dilution unit, performed the measurements, and which held the supercurrent analysis. The following findings will result in a publication.

In the beginning of the chapter, I remind briefly the device fabrication, and how the sample is tuned to the DQD geometry. Then, I refer to the fundamental properties of the device and I extract energy scales such as the charging energy U and the level spacing ΔE. In the next sections, I characterize the superconducting properties of the leads and extract the superconducting gap Δ. In addition, I talk about the supercurrent fitting process and finally, the supercurrent measurements of the double quantum dot are introduced.

4.2 Defining a DQD in a nanowire device

The device we studied can be seen in Fig. 4.1a. Of the total number of bottom gates that lie below the nanowires, only 5 of them are contacted and used during the experiments. These gates are noted as g_i with i=1...5. Gates g_1 and g_5 have the role of creating the tunnel barriers between the superconducting leads and the quantum dots. Gate g_3 adjusts the inter-dot coupling, while g_2 and g_4 are the plunger gates which tune the levels of each dot. The gates are separated from the nanowire by a thin HfO_2 layer. The InAs nanowire we used has a 7 nm epitaxially grown aluminium shell, and was deposited to the substrate using a micromanipulator. The area of the nanowire above the five bottom gates was wet-etched to remove the aluminium layer, creating a Josephson junction. The last part of processing was the design and deposition of the leads which were made of titanium/gold. Standard electron beam lithography steps were used to fabricate the device and the bottom gates on the substrate. The complete fabrication recipe is included in Appendix B.

Moreover, the chip is also equipped with a backgate which allows us to deplete the nanowire in the areas with no connected bottom gates. This option of tuning turned out to be very useful since it helps to explore different regimes of the double quantum dot, by either applying negative backgate voltages to fully deplete the nanowire, or applying positive voltage with the aim to populate the nanowire leads with electrons.

Figure 4.1b shows the analogous picture of the DQD sketch shown in Fig. 4.1a in the energy-position space. Each QD has one electron on their highest energy orbital. Gates g_1, g_3 and g_5 form tunnel barriers which can be described by the tunnel couplings t_L, t_d and t_R.

4.3 Stability diagram of the DQD

This section introduces the charge stability diagram of our superconductor-double quantum dot-superconductor (S-DQD-S) device. Double quantum dot systems with normal leads have been studied extensively [20] in the past, however the equivalent system with superconducting contacts has been an unexplored area of quantum transport.

Figure 4.1c shows the linear conductance versus plunger gates V_{g_2} and V_{g_4}, also known as charge stability diagram, of our S-DQD-S device. To obtain the DQD configuration of the system, the barrier gates and the backgate were tuned to the following voltages: $V_{g_1} = -9.2\,V$, $V_{g_3} = -9.3\,V$, $V_{g_5} = -0.25\,V$, $V_{bg} = 10.4\,V$. The plunger gates controlling the right and the left dot are at far more positive values because we want to create two quantum wells that can host quantum dots.

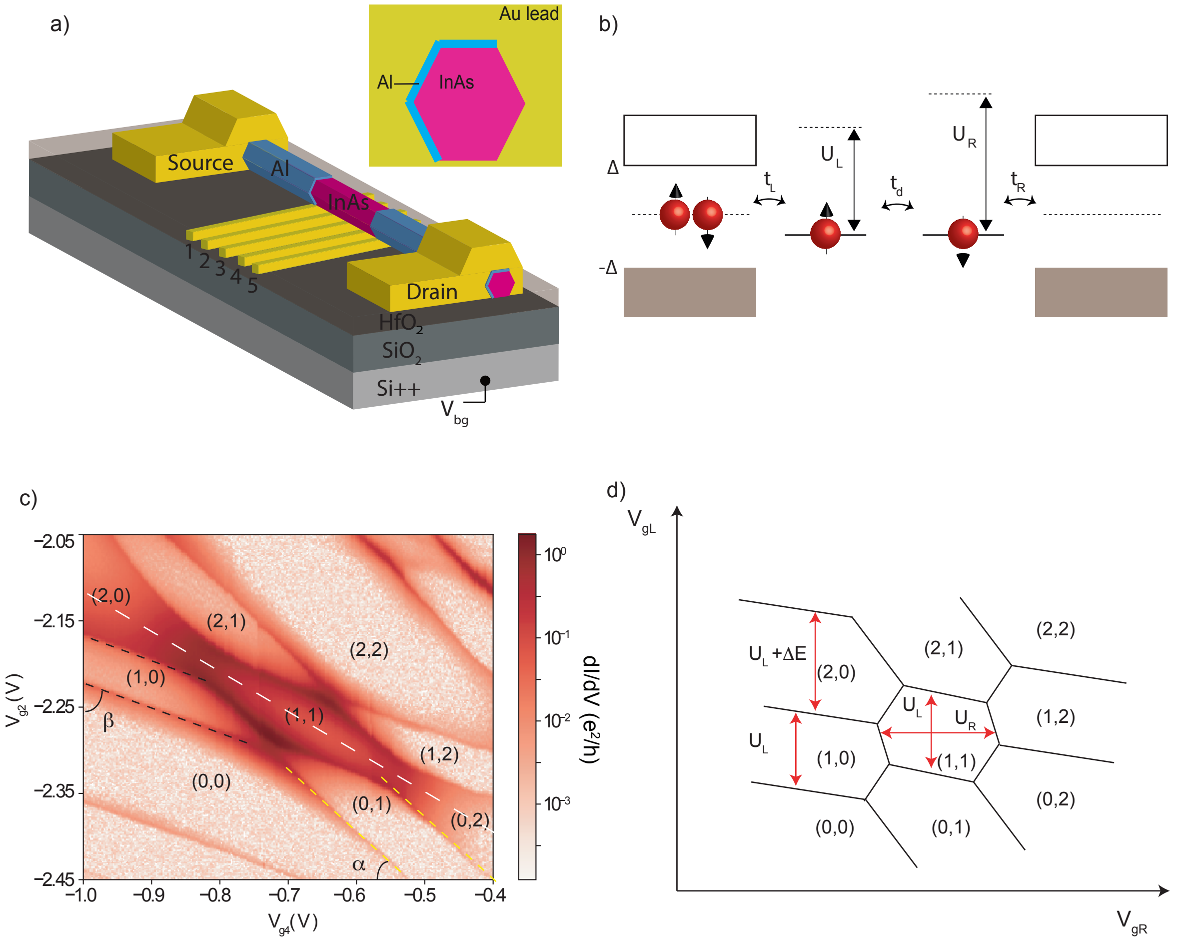

Figure 4.1: a) A sketch of the measured device. The substrate consists of a highly doped Si layer on top of which thin bottom gates are fabricated, which are covered by a thin HfO_2 layer. A single nanowire is deterministically deposited on top of them. Apart from the five bottom gates that are capable of tuning the nanowire, a backgate was also used. Note that the leads are the 7 nm epitaxial Al shell. The inset shows a cross section of the InAs nanowire with the 3 facet epitaxial aluminium. b) Schematic illustrating transport through a S-DQD-S device. t_L and t_R represent the tunnel coupling to the left and the right lead respectively, while t_d is the inter-dot coupling. Red spheres represent spin up or down electrons. The quantum dots have charging energies larger than the superconducting gap Δ and their significant level spacing allows us to treat them as single levels. c) Charge stability diagram of the zero bias conductance. The x axis represents the modulation of the gate that controls the right dot, while the y the modulation of the left one. The numbers (n,m); n,m=0...2, represent the occupancy of the left and the right dot respectively. The black dashed lines follow the parity change lines for the left dot, while the yellow ones for the right dot. Electron-hole symmetry is depicted, as the white dashed line shows a mirroring symmetry in the DQD. d) Simplified charge stability diagram of a DQD coupled to normal leads. For Coulomb diamonds with odd occupancy, the energy required to add another electron to the level is U, while if there is even number of electrons it is $U + \Delta E$.

On the other hand, the barrier gates are negative enough to ensure that the coupling to the leads is sufficiently low. The diagram hints that both plunger gates have an effect on both dots, due to capacitance coupling between the gates. However, judging from the slope of the degeneracy lines-as shown with the dashed lines-, g_2 predominantly controls the left dot while g_4 the right one. It can also be determined how strongly a gate affects a QD by the angles α and β. The closer to 90°, the stronger the influence a gate has to a QD.

There are many similarities between this charge stability diagram and a charge stability diagram of a DQD in the normal state, which is described in the theory chapter. A distinctive difference though is that the (1,1) charge sector is much more conductive compared to the other regions of the map. That is because the zero bias conductance that we observe is related to supercurrent, and on that charge sector, Cooper pair transport is more favoured because there are more co-tunnelling processes available. Moreover, near the triple points, the degeneracy lines acquire a small curvature, which is a sign of significant inter-dot coupling t_d [20].

Furthermore, the charge stability diagram is symmetric around the white dashed line shown in Fig. 4.1c, meaning that the (0,0) and the (2,2) charge sectors are similar. That proves that the system is electron-hole symmetric, as it treats a fully occupied level in the same way as an unoccupied one.

4.4 Basic characterisation

When studying a double quantum dot, it is essential to define a system where each dot consists of a single level. That way, transport processes are simplified, as there is only one available path for electrons. If we succeed in defining such a system, then it is important to identify the (1,1) charge sector, in order to map all the adjacent ones and be able to further study and analyze it. Several ways can be used to achieve that, such as spin blockade [37] or simply by defining a system that has shell filling [38]. The latter, involves quantum dots with energy levels that have a significant energy difference between them. In other words, the level spacing ΔE should be in the same order of magnitude with the charging energy U. Since only two electrons can occupy a level, the addition energy to add a 3rd electron is equal to $U + \Delta E$, whereas if a level is occupied by only one electron, only U needs to be paid. These situations describe the even and the odd QD occupancy respectively [16]. It is easy to understand now why the (1,1) hexagon is the smallest in size. Both dots are singly occupied, resulting in energy U between the parity change lines in both directions. These lines are the points where charge fluctuations happen, being equally favorable to have n, or n+1 electrons when a QD is tuned accordingly. If one QD has odd number of electrons and the other has even, such as the (2,1) sector, then adding a charge on the left QD would require $U + \Delta E$, while adding on the right one U. As a result, by identifying the smallest charge sector it is easy to label all the other parts of the charge stability diagram. Figure 4.1d shows an ideal

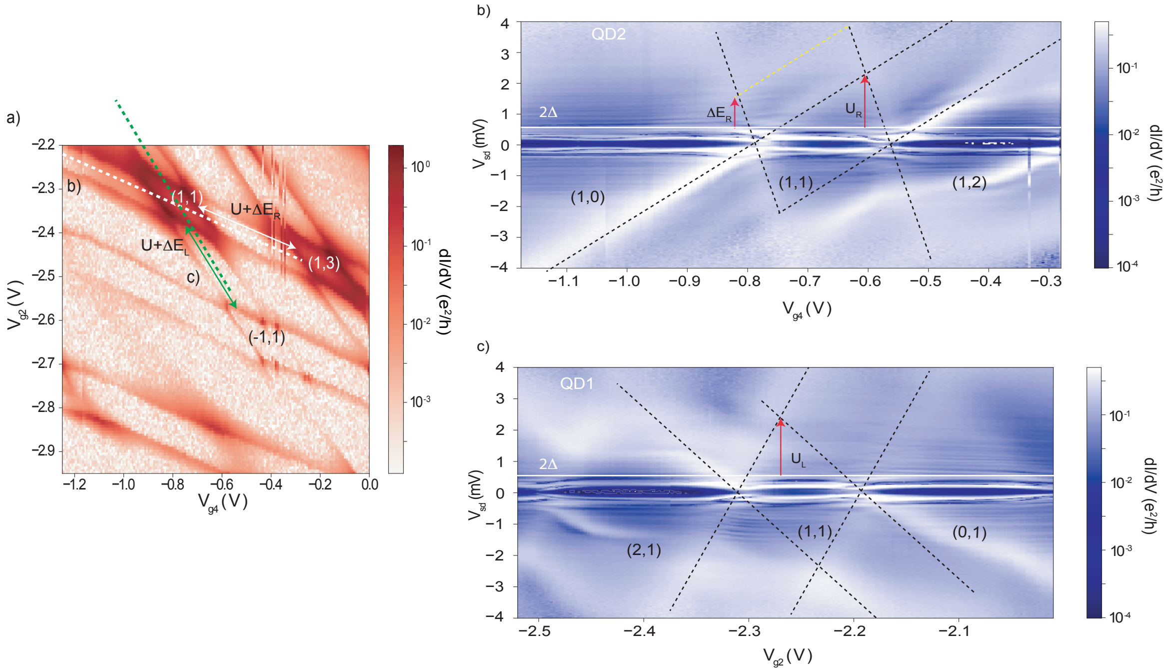

Figure 4.2: a) A larger overview of the studied honeycomb pattern, showing two adjacent 1,1 sectors. Dashed lines indicate the cut directions of b (white) and c (green). Arrowhead lines show the U + ΔE for the left (green) and the right (white) dot respectively. It is easy to see the similarities with the DQD schematic of Fig. 4.1d, as the (1,1) sectors are well defined and the level spacing is significant. b) High bias spectroscopy of the right QD revealing a Coulomb diamonds pattern. The white solid line indicates the energy of 2Δ in the device. Dashed lines are used as a guide to the eye for the Coulomd diamonds. The lever arm is found $\alpha_R = 0.009$ c) High bias spectroscopy for the left dot. The lever arm is found $\alpha_L = 0.02$.

charge stability diagram of a DQD with $t_d = 0$ for simplicity. The energy separation of two charge sectors is shown by the distance two parity change lines have. For instance, to drive the DQD from the (1,0) to the (2,0) sector, energy equal to U_L has to be paid. That is because the left QD has an odd number of electrons. However, moving from the (2,0) to the (3,0) requires the usage of the next unoccupied level of the left QD, as the one previously used is filled. As a result, apart from the charging energy U the level spacing energy ΔE is also to be paid.

Figure 4.2 illustrates the two different methods of extracting the charging energy and the level spacing. Figure 4.2a, shows an overview of three (1,1) sectors. Comparing the plot to Fig. 4.1d verifies that there is shell structure in our DQD, as the level spacing is significant for both QDs. Figures 4.2b,c show differential conductance in logarithmic scale versus V_{g_4} and V_{g_2} respectively, which define Coulomb diamonds along each dot. The white dashed lines sketch the Coulomb diamonds, while the yellow shows the excited level of the right QD. The distance sketched with the red arrow pointing to the yellow dashed line provides us the level spacing. Note, that for low bias, there is no conductance due to the presence of the superconducting gap Δ. To correctly estimate the parameter ΔE, we are subtracting 2Δ from the calculation because the measurement is valid for the normal state regime. The superconducting properties of the junction will be analysed in the following section. In a similar pattern to ΔE, U is extracted by measuring the distance from the center of the Coulomb diamond to the top of the diamond. However, in our case we do not measure from the center, because the plunger gate is capacitively coupled to the other gates, modifying the picture of Coulomb diamonds. For the specific charge sector that we studied extensively, we extracted $\mathrm{U_L} \approx 1.85$ meV, $\Delta \mathrm{E_L} \approx 1.64$ meV for the left dot and $\mathrm{U_R} \approx 1.62$ meV, $\Delta \mathrm{E_R} \approx 1.76$ meV for the right one. In Fig. 4.2c there are no visible excited states of the left dot, hence the level spacing was measured with an alternative way, by calculating the lever arm $\alpha_{\mathrm{L}} = 0.02\,\mathrm{eV/V}$, and then extracting the ΔE from Fig. 4.2a. The lever arm shows the relation between the plunger gate and the bias applied to the device. It is given by dividing the charging energy to the gate difference between two Coulomb peaks.

Clearly, our DQD system can be modelled as a two lateral *single levels* as $\Delta \mathrm{E_{L,R}}$ is found on the same order of magnitude with $\mathrm{U_{L,R}}$.

Characterisation of the superconducting gap

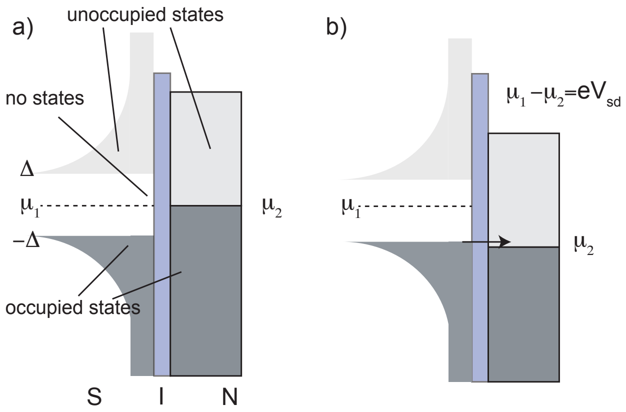

Figure 4.3: a) Energy schematic in respect to position for a superconductor-insulator-normal (SIN) junction. For bias voltages $|V_{\mathrm{sd}}| < \Delta/e$ tunneling processes are prohibited due to the absence of available states in the superconductor. Dark gray areas represent occupied states while light gray unoccupied ones. b) For $V_{\mathrm{sd}} > -\Delta/e$ then the filled states of the S are in the same electrochemical potential with unoccupied states in the metal. Thus electron transport occurs.

In this subsection, we want to characterise the superconducting properties of the leads, since an estimate of the superconducting gap Δ is essential for analysing our system. To achieve that, we tuned the DQD to a regime with much weaker tunnel couplings to the leads.

Typically the superconducting gap can be extracted by tunneling spectroscopy which probes the density of states (DOS) in the superconductor. A basic geometry that allows the identification of the superconducting gap is a normal-insulator-superconductor (NIS) junction. The energy diagram of a SIN junction is shown in Fig. 4.3a. When the normal metal DOS are probing the superconducting DOS through a tunnel barrier, then the coupling is very low. For spectroscopy, that is an advantage, since we can study fine features as the probe is not broadened. Hence, by modifying the electrochemical potential of the normal lead, starting from $-\Delta$ to Δ, and by calculating the differential conductance $\frac{dI}{dV_{sd}}$ one can measure the density of states of the superconductor. When $V_{\mathrm{sd}} < -\Delta/e$ then there is electron transport since the N has filled states and the S has unoccupied states. As the bias increases, a peak in $\frac{dI}{dV_{sd}}$ is seen at $-\Delta$ followed by zero $\frac{dI}{dV_{sd}}$ since there are no available states on the S up to Δ. Therefore, spectroscopy is a way of visualising the DOS of a superconductor, and extracting its gap. In a similar pattern, probing of the DOS of a superconductor has been demonstrated in S-QD-S devices [23] and we also follow the same method in our S-DQD-S device. However, now the system has a level between the two S contacts that should not be in resonance with the electrochemical potentials of the leads in order to do spectroscopy of the superconducting gap. Hence, the QD levels should be in co-tunneling regime (Coulomb blockade), meaning that they should be away from E_{F}. A S-QD-S junction with the QD level in co-tunneling is illustrated in Fig. 4.4a.

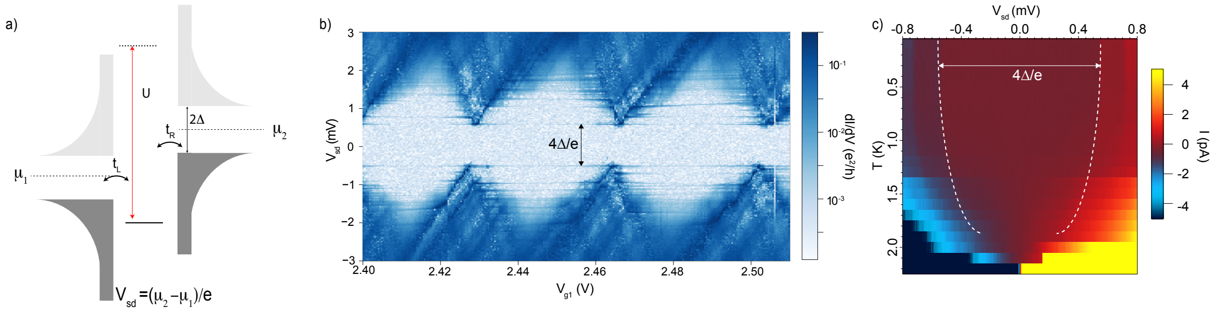

Figure 4.4: a) Schematic of two superconducting DOS probing each other. An example of a S-QD-S junction with the level of the QD tuned in co-tunneling mode. This way, $\mu_{\mathrm{L,R}}$ are not in resonance with the level, and we can probe the DOS of the superconductor. The tunnel couplings to the leads are described by $t_{\mathrm{L,R}}$ and the charging energy U is noted. b) Coulomb diamond spectroscopy of the opaque-tuned regime. Note that due to the small level spacing in the quantum dot, many co-tunelling lines are appearing inside the diamonds, verifying the small distance to excited states.These co-tuneling processes are present due to the multi-level nature of the dot. The distance noted by the two-headed arrow dictates shows the 4Δ with $\Delta = 0.27\,\mathrm{meV}$. c) Temperature dependence of the superconducting gap. The two BCS peaks are suppressed by the increase of T and eventually close down at approximately T = 2.2K.

To study sub-gap spectroscopy is it helpful that the superconductors have a ‘hard-gap’ [12], meaning that the density of states go to zero within ±Δ and not at a finite number. Alternatively, local density of states within the gap might disturb spectroscopy and analysis of the sub-gap states or supercurrent. To measure the value of the superconducting gap, the device was tuned to a weak tunnel coupling regime, with the backgate at a much more negative value $\mathrm{V}_{\mathrm{bg}} = -15\,\mathrm{V}$ to deplete the nanowire. Figure 4.4b shows a color plot of conductance with respect to source-drain voltage and plunger gate voltage,. A clear Coulomb blockade pattern is observed, which is lifted by a finite value (see arrow) due to the two superconducting DOS probing each other. $4\Delta/e$ is given by the distance dictated by the line in the graph. It is 4 times the superconducting gap is because we are probing a superconductor with another superconductor, meaning that in the extreme case that the one BCS peak on the left SC is probing the lower BCS peak of the right one, the energy distance is 2Δ, as shown in Fig. 4.4a. Likewise, on opposite bias, the distance is again 2Δ and by summing these two we receive 4Δ Fig. 4.4c shows the temperature dependence of the superconducting gap. The critical temperature is found $T_c = 2.2$ K, consistent with earlier findings in thin Al films [12]. That value is larger than typical bulk aluminium which is $T_c = 1.2$ K.

4.5 Supercurrent characterisation and fitting procedure

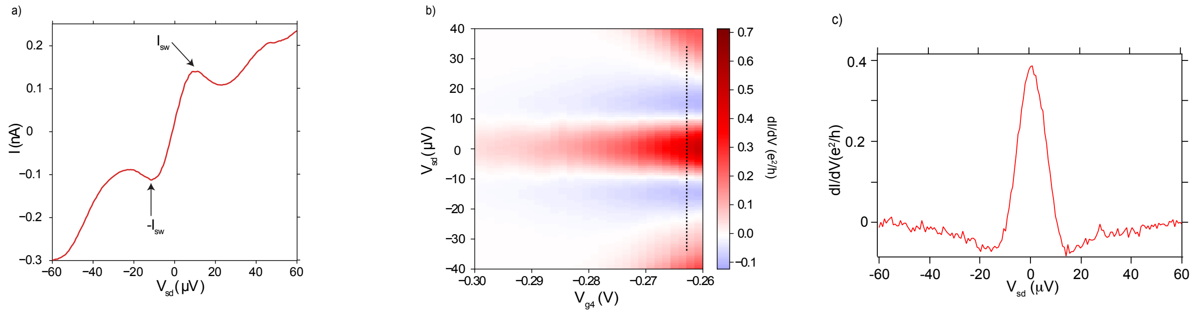

Figure 4.5: a) I-V curve of measured supercurrent of our S-DQD-S device. The point where the supercurrent ceases and the Ohmic I-V behaviour of the semiconductor takes over is shown with the two arrows. These points are known as switching current of the junction. b) Differential conductance measurement revealing supercurrent. The y axis is the source-drain bias and the x the plunger gate voltage. In differential conductance, the supercurrent behaviour is transformed to a zero-bias peak, while for $I > I_{sw}$, NDC features are observed, which are a signature of a Josephson junction, as the decrease in current is providing negative conductance. c) the equivalent plot of panel a in differential conductance. It is clear that the zero bias peak has adjacent dips in conductance that create NDC features, which are a signature of supercurrent.

To study supercurrent flowing through the DQD, the device was tuned again to the regime shown in Fig. 4.1c.

It is well established that a device of two superconductors separated by a weak link gives rise to a non-dissipative current which flows through the junction without any applied voltage. However, measurements of such a device in a lab are made at a finite temperature and the metallic leads that are used to probe the device carry significant resistance due to the RC filters that are connected to the leads. The combination of these two factors lead to the non-ideal case of a dissipative supercurrent.

To examine and analyze the supercurrent data, it is important to first characterise our junction. An example of a supercurrent measurement can be seen in Fig. 4.5a. Note that the supercurrent is not perpendicular to the bias axis, but it has a finite slope, owning to thermal noise. That causes the theoretically divergent conductance to converge at a finite value. That is also what we observe in Fig. 4.5b which is the conductance picture of supercurrent. As seen in Fig. 4.5c, a zero bias peak is observed, followed by negative differential conductance (NDC) features adjacent to it. The negative differential conductance is appearing when the device shifts from the Josephson supercurrent regime, to the classic Ohmic behaviour. That point is known as the switching current of the device, and is noted as I_{sw}.

Extended RCSJ model

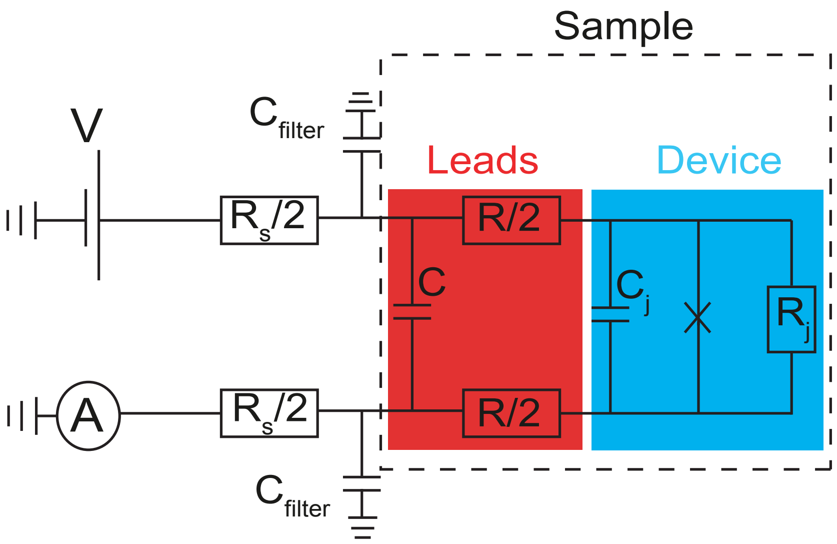

Figure 4.6: A schematic of the measurement setup showing in detail each component used in the quality factor. The system is voltage biased and on both lines of source and drain there is an *RC* filter with $\frac{R_s}{2} = 4.12\,k\Omega$. Then, the leads of the sample are modelled with a resistance R and a capacitance C, included in the red dotted frame. Finally, the RCSJ analogue of our device is framed in the light blue box, consisting of the resistance and the capacitance of the junction C_j and R_j respectively, which are set in parallel to our Josephson junction.

In order to model our junction and characterize the supercurrent, we use the extended RCSJ model [39, 27, 36] which is based on the RCSJ model described in the theory chapter. The circuit equivalent is shown in Fig. 4.6. As our junction has metallic leads, they hold a certain resistance and capacitance R,C that should be accounted in the supercurrent extraction. The resistance of the leads is connected in series to the junction, while the capacitance in parallel. Hence, the plasma frequency is modified to

$$\omega_p = \sqrt{\frac{2eI_c}{\hbar(C(1+\frac{R}{R_j})+C_j)}}$$

and the quality factor is now written [39]:

$$Q = \frac{\sqrt{\hbar(C(1+R/R_J)+C_J)/(2eI_c)}}{RC+\hbar/(2eI_cR_J)}$$

with C,R the capacitance and resistance of the leads and C_J, R_J the capacitance and resistance of the junction itself. C_J can be extracted by modelling the junction as two parallel metallic plates. We obtain $C_J = 0.46\,\mathrm{aF}$. The junction resistance was estimated to be $R_J = 1\,\mathrm{G}\Omega$ since all the measurements were conducted in the Coulomb blockade regime in a hard superconducting gap. Through the fitting process that will be described below, the resistance of the leads was found to be $R = 3\,k\Omega$, while the capacitance can be modelled as a parallel-plate capacitance between the leads of the device and the backgate of the chip, which is separated by a thin $\mathrm{SiO_2}$ layer of 300 nm. We estimate the area of that capacitor to equal with the surface area that the leads have. Hence, $C = \varepsilon_r\varepsilon_0\frac{A}{d} = 9\,pF$. During our measurements, the critical current was found oscillating between 200 to 2000 pA, depending on how near the system was to a degeneracy and to the (1,1) charge sector. As a result, an average estimate of the quality factor with $I_c = 1000\,\mathrm{pA}$ gives $Q = 0.16$, which makes the junction overdamped since $Q \ll 1$. The quality factor remains in that limit for I_c varying from 50 pA to 2 nA, showing that the device remains in the overdamped regime despite the fluctuations of conductance. Moreover, an argument that supports the overdamped sign of our junction is that the current-voltalge characteristic is symmetric as shown in Fig. 4.5.

I_c extraction

Since our Josephson junction interferes with the environment, we have to take into account thermal noise caused by it. Hence, to extract the critical current we are using a formula developed by Ivanchenko et al [27], and used by other research groups [39, 29]. Through this formula, it is possible to extract the critical current $\mathrm{I_c}$ as a function of source-drain voltage, temperature and resistance of the leads and the junction for every value of the gate voltage measured.

$$I(V_{\mathrm{sd}}) = \frac{R_J}{R_J+R}\left(I_c Im\left[\frac{I_{1-i\eta(V_{\mathrm{sd}})}(\beta)}{I_{-i\eta(V_{\mathrm{sd}})}(\beta)}\right] + \frac{V_{\mathrm{sd}}}{R_J}\right)$$

As we are measuring differential conductance, we differentiated the formula to turn it into a function of $\frac{dI}{dV_{\mathrm{sd}}}$. $I_\alpha(x)$ is the modified Bessel function of complex order α while $\eta(V_{\mathrm{sd}}) = \frac{\hbar V_{\mathrm{sd}}}{2eRk_BT}$, and $\beta = \frac{I_c\hbar}{2eRk_BT}$ involves the ratio between the Josephson energy E_J and the thermal energy. An example of the fitting process can be seen in Fig. 4.7, where real data is fitted using the above function. Note, that it is required to have Josephson energy much smaller than thermal energy

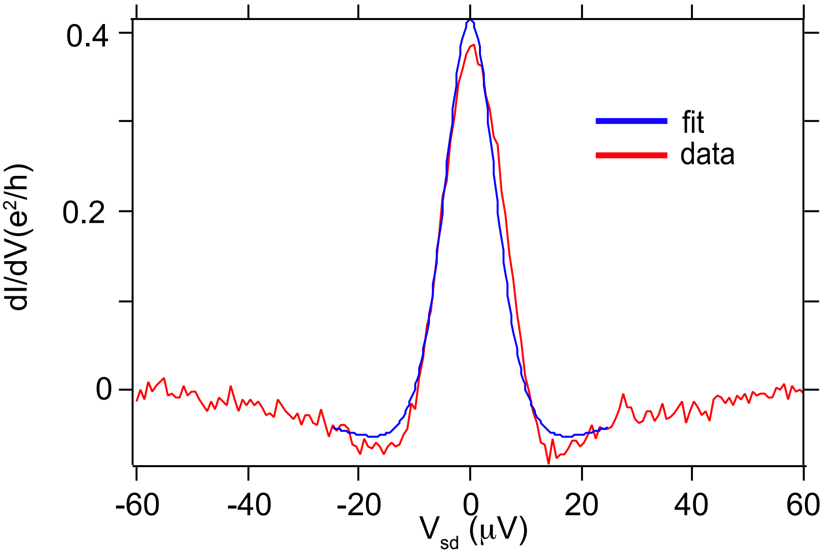

Figure 4.7: An example of a fitted supercurrent. The x axis is the source-drain voltage and the y is conductance in $\frac{e^2}{h}$. The blue curve is the fitting using the Ivanchenko formula[27]. The success of a fitted supercurrent lies in the accuracy of the width and the peak height of the fitted curve in comparison to the actual data.

in order for the fit to be valid $\mathrm{E_J} \ll \mathrm{k_B T}$, since that provides a convergent zero bias peak that corresponds to the measurements [27]. Ideally, we should observe a divergent supercurrent peak, but thermal fluctuations caused by electron temperature create a dissipative zero bias peak. In the fitting process, 4 parameters are used with 3 of them being fixed for all the fits that took place in the different charge states and regimes. The fixed parameters were $R_J = 1\,\mathrm{G\Omega}$, $R = 3\,k\Omega$ and $T = 80\,\mathrm{mK}$ which is the temperature of the electrons that pass through the device. The base temperature measured on the mixing chamber was $T = 25\,\mathrm{mK}$, however it is not possible to cool down electrons at base temperature, and as a result we expect their temperature to be higher. The only parameter that is free to fluctuate for different plunger gate voltage is the critical current I_c. From each data point, the peak of the fitted curve is extracted and then the map of supercurrent versus V_{gate} is retrieved.

4-Terminal vs 2-Terminal

The optimal way of measuring a device is by using a 4-terminal technique in order to discard any unwanted resistance from the filters and the leads. However, the need of increasing the device yield forced us to decrease the number of bonding pads for each device, to fit more devices in a single sample. Hence, we measured all our devices using two leads. As we are measuring with a standard 2-terminal technique, we had to find a way to discard from the measured source-drain voltage and differential conductance the series resistance of the filters in the dilution unit, which were $R_\text{s} = 8.24\,k\Omega$. The corrected values were

$$V_\text{SD} = V_\text{SD measured} - IR_\text{s}$$

and

$$\frac{dI}{dV_\text{sd}} = \frac{1}{(\frac{1}{\frac{dI}{dV}} - R_\text{s})\frac{e^2}{h}}$$

If the device is in a low conductance regime i.e. low current, then the corrections to V_SD and $\frac{dI}{dV_\text{sd}}$ are negligible, while for higher conductance regions such as near the (1,1) sector, there is a significant correction.

4.6 Supercurrent as a function of QD occupation

Previous works involving Josephson junctions and quantum dots have demonstrated that the QD occupation plays a significant role on the magnitude of supercurrent, inducing $0 \rightarrow \pi$ transitions depending on the ground state of the system. In this project, we expanded the studied S-QD-S geometry [29] by including a second QD connected in series. It is interesting to study how the ground state of each charge state affects the sign of the supercurrent, as well as how the supercurrent behaves in the hybridised states near the triple points.

In this section we investigate how supercurrent flowing through a double quantum dot behaves at different dot occupancy combinations, as well as show the fitted supercurrent traces through different charge states of the DQD.

Figure 4.8 shows a zero bias conductance map versus the two plunger gates of double quantum dot shell with occupancy indicated by (n,m) for the left and the right dot respectively. The dashed lines indicate cuts in gate space, where the supercurrent is investigated. By keeping the level of one dot out of resonance, we tuned the other QD to study the behaviour of the zero bias peak at different QD occupations. Moreover, supercurrent is stronger near the parity lines and in particular, near the triple points. That arises because the co-tunneling processes that allow Cooper pair transport are enhanced when the QD levels are near resonance with the leads. Note that the conductance is stronger in the (2,0) than in the (0,2) charge sector which indicates that V_gL has a significant effect on the tunnel coupling to the lead. Specifically, for more negative V_gL the overall conductance decreases. Furthermore, it is important to remember that the occupation of the DQD has a direct influence to the ground state of the system. Specifically, for even number of electrons the ground state is a singlet $|S\rangle$, while for odd number a doublet $|D\rangle$ ground state. This information will be handy on the next sections of the chapter when we will discuss ground state transitions.

Figure 4.9 shows the traces noted with white-dashed lines in Fig. 4.8. Each panel shows a conductance color map in respect to V_SD and gate voltage. In Fig. 4.9a the right quantum dot is

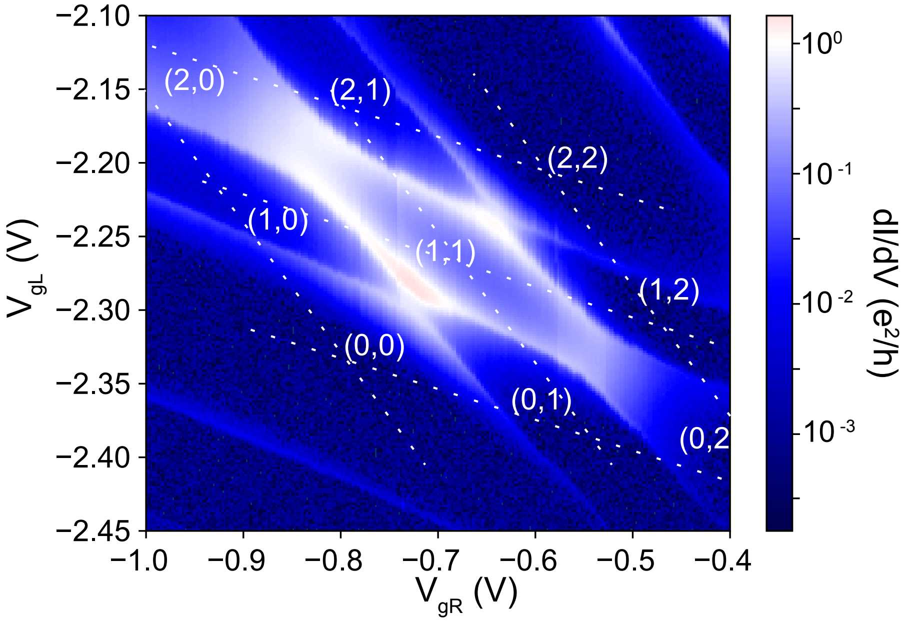

Figure 4.8: A color map of zero bias conductance revealing supercurrent in a double quantum dot. V_{gL} and V_{gR} are the plunger gates of the left and the right dot. The numbers on each charge hexagon represent the occupancy of the highest level of each dot. Each dashed line shows the trajectory of a cut measuring conductance over a finite source-drain window. Zero-bias conductance (supercurrent) is enhanced near the triple points due to resonance between the levels of the dots and the leads. Note that this measurement is the same shown in Fig. 4.1c, but the colour code has changed to see better the changes of conductance in the triple points.

tuned while the left is being fixed at 2 electrons on its highest occupied level. As V_{gR} is swept the DQD is transiting from the (2,0) to the (2,1) and finally to the (2,2) charge state. As the system is approaching a parity change line, the zero bias conductance is enhanced, owing to enhanced co-tunneling processes. At the transition point, we observe an abrupt decrease in the magnitude of the conductance peaks, and at the next transition point (2,1) → (2,2) another abrupt increase. Figure 4.10b is a line-cut through the (1,1) charge sector, while keeping the left dot occupancy fixed. In contrast to panel a, the abrupt sharp drops in the zero bias peak amplitude are now facing the opposite direction. Moreover, the conductance is higher compared to other panels due to the fact that the line is passing through the (1,1) sector. Panel c shows a trace starting from the (0,0) sector, then to the (0,1) and finally to (0,2). Similarities can be seen with Fig. 4.9a. The conductance peak is again strong on the (0,0) and (0,2) charge states, while it diminishes in the oddly occupied (0,1). On Fig. 4.9d,e and f the gate that controls the left quantum dot is now swept, while the occupancy of the right dot is fixed. These traces are qualitatively similar to the left column panels. Again, the supercurrent drops are facing towards the charge states with odd number of electrons, and we also observe the same behaviour at the (1,1) sector.

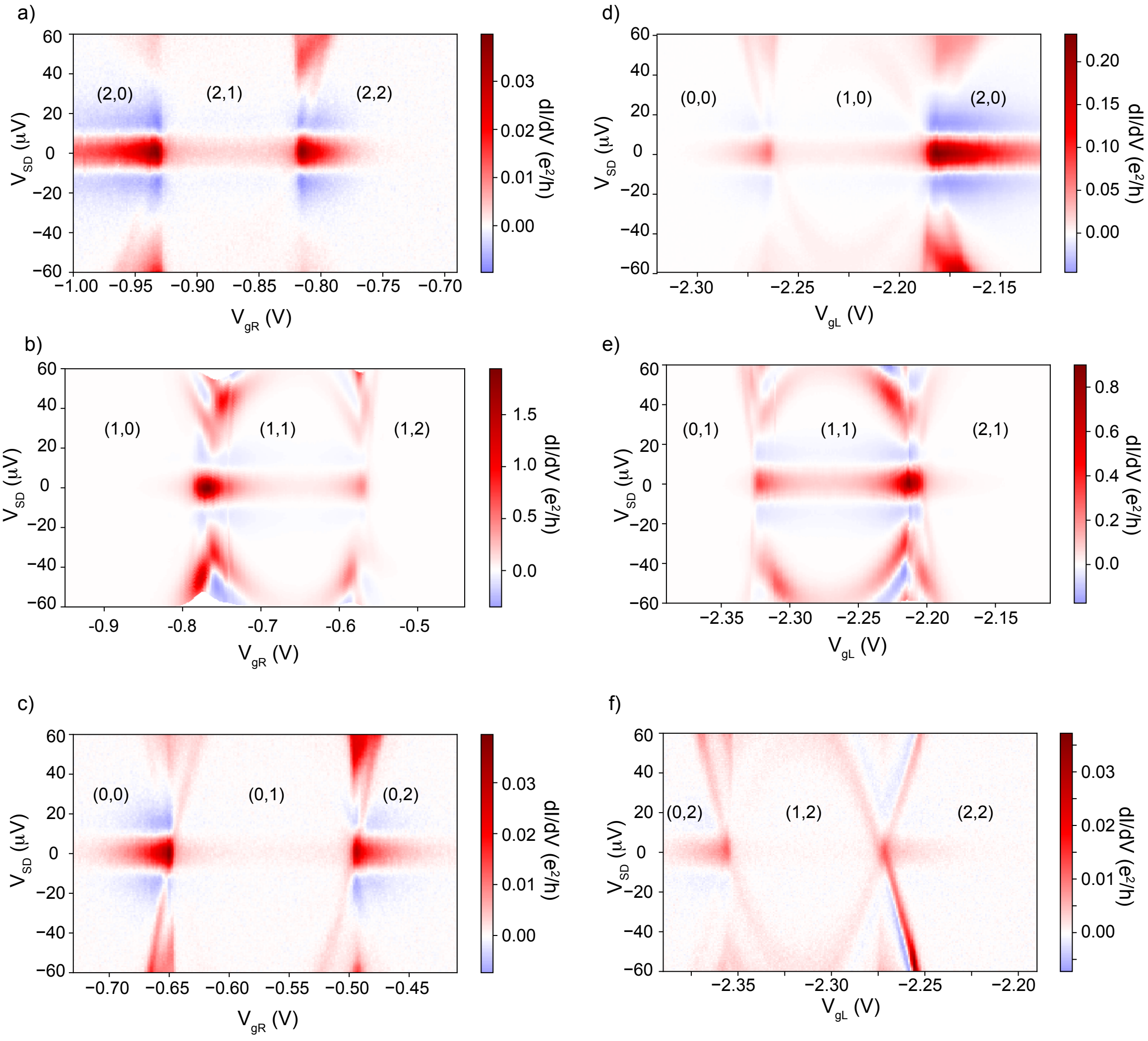

Figure 4.9: Bias spectroscopy of the zero-bias peak versus plunger gate over a source-drain window of 120 μV. a) A trace passing through the (2,0), (2,1) and (2,2) charge hexagons. The presence of NDC (blue colour) adjacent to the zero bias peaks verifies that it is a supercurrent feature. b) Conductance peak measurement through the (1,1) charge sector. The drops in conductance are facing towards the doublet ground state diamonds. c) Measurement through the (0,0), (0,1) and (0,2) charge sectors. d,e,f) Analogous measurements of zero bias peaks with the difference of sweeping the gate that controls the left dot.

These measurements show a pattern in the zero bias peak through a DQD system. For Coulomb diamonds with singlet ground state, the conductance peak is strong while at the doublet ones, the peak is much weaker. Moreover, on every $|S\rangle \longrightarrow |D\rangle$ transition an abrupt decrease in the zero bias conductance occurs and vice versa. That behaviour hints a $\phi_0 = \pi$ shift in the current-phase relation of the supercurrent $I_s = I_c \cdot sin(\phi + \phi_0)$.

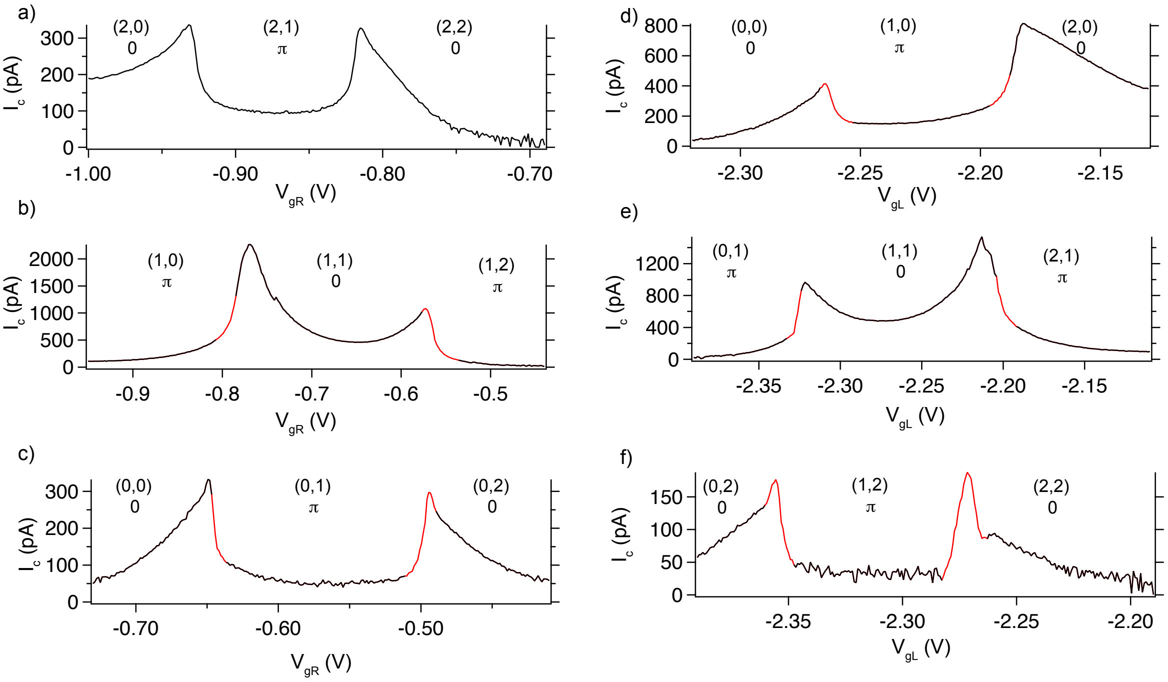

Figure 4.10: a-f panels correspond to the respective ones of Fig. 4.10, revealing supercurrent via fitting the zero bias conductance peak of the measurements. Note that the points with red colour are fittings which were not optimal to the width and height of the peak, due to the fact that non supercurrent features (sub-gap states) are crossing $V_{SD} = 0$ and eventually alter the zero bias peak. The numbers above each region show the occupancy of the left and the right dot respectively, while 0 and π refer to the phase shift of the current-phase relation.

The measurements indicate peaks in differential conductance which hint supercurrent physics, thus to correctly analyse and interpret our results, we fitted the zero bias peak with the formula from Ivanchenko et al. [27] as explained in the last section. The fitting is extracting the supercurrent I_c for each source-drain trace. Figure 4.10 shows the equivalent fitted supercurrent of the differential conductance plots. Each point of a graph corresponds to a fit of a zero bias curve, as shown in Fig. 4.7. The abrupt drops observed in conductance at the transition points are also visible in the supercurrent fits, verifying the claim that a $0 \longrightarrow \pi$ transition occurs. Similar features have been detected by other works in S-QD-S devices [29, 7]. Note, that in theory the supercurrent in the π regions should be negative, however the fitted supercurrent is positive throughout the V_{gate} range, as we can only measure the amplitude and not the sign of current. Another observation is that I_c is indeed stronger near the (1,1) charge sector, as it is visible from Fig. 4.10b,e. Moreover, for some gates voltages the fit does not work as intended. Specifically, when other conductance features (sub-gap states) are approaching zero bias, they interfere with the zero bias supercurrent peak, resulting in a superposition of peaks. That creates an unreliable fitting of the zero bias peak. Such a fit is shown in Fig. 4.11.

To summarize, we attribute the transitions of supercurrent to ground states transitions $|S\rangle \rightarrow |D\rangle \rightarrow |S\rangle$ of the DQD. I_c fits come in accordance to the conductance maps, revealing the relation of the zero bias peak to the extracted critical current. The abrupt drops are captured by the fit, as well as the magnitude of the I_c corresponds to the conductance level. In the conclusion of this chapter I will show that recently developed theory is consistent with these experimental findings.

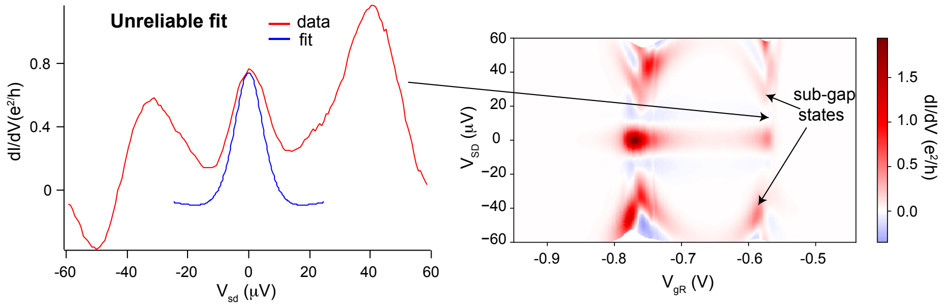

Figure 4.11: An example of an unreliable fit taken from Fig. 4.11b. The arrow is pointing at the point where the trace was taken, at $V_{\text{gR}} \approx -0.57\,\text{V}$. Near zero bias, there is a superposition of three peaks, the central one which corresponds to supercurrent, and two others of the sub-gap states which are crossing zero bias. Two black arrows show the sub-gap states that are crossing zero-bias. Hence, the fitting fails since it is not meant to capture other features than supercurrent.

Molecular regime

An area of study that is rich in information about the DQD is the 'molecular' regime of the double quantum dot, in the vicinity of two triple points [20]. There, the orbitals of two charge states i.e. (0,1) and (1,0) form a bonding orbital that has the lowest energy $|D(1{,}0) - D(0{,}1)\rangle$, and an anti-bonding $|D(1{,}0) + D(0{,}1)\rangle$ with a higher energy [1].

If the DQD system is well coupled, then the eigenstates become delocalised and there is a global ground state of the system. In such a case, it is interesting to study how supercurrent

---

[1] These wavefunctions refer to the spin part of the total wavefunction $\Psi = |X\rangle\,|S\rangle$, with $|X\rangle$ being the spacial part and $|S\rangle$ the spin part. Since electrons are fermions, the total wavefunction should be asymmetric. Hence, for asymmetric spin part, the spacial part of the wavefunction should be symmetric, creating a σ orbital, which is a bonding orbital. On the other hand, for symmetric spin part, the spacial part has to be asymmetric, creating a p-orbital which is anti-bonding.

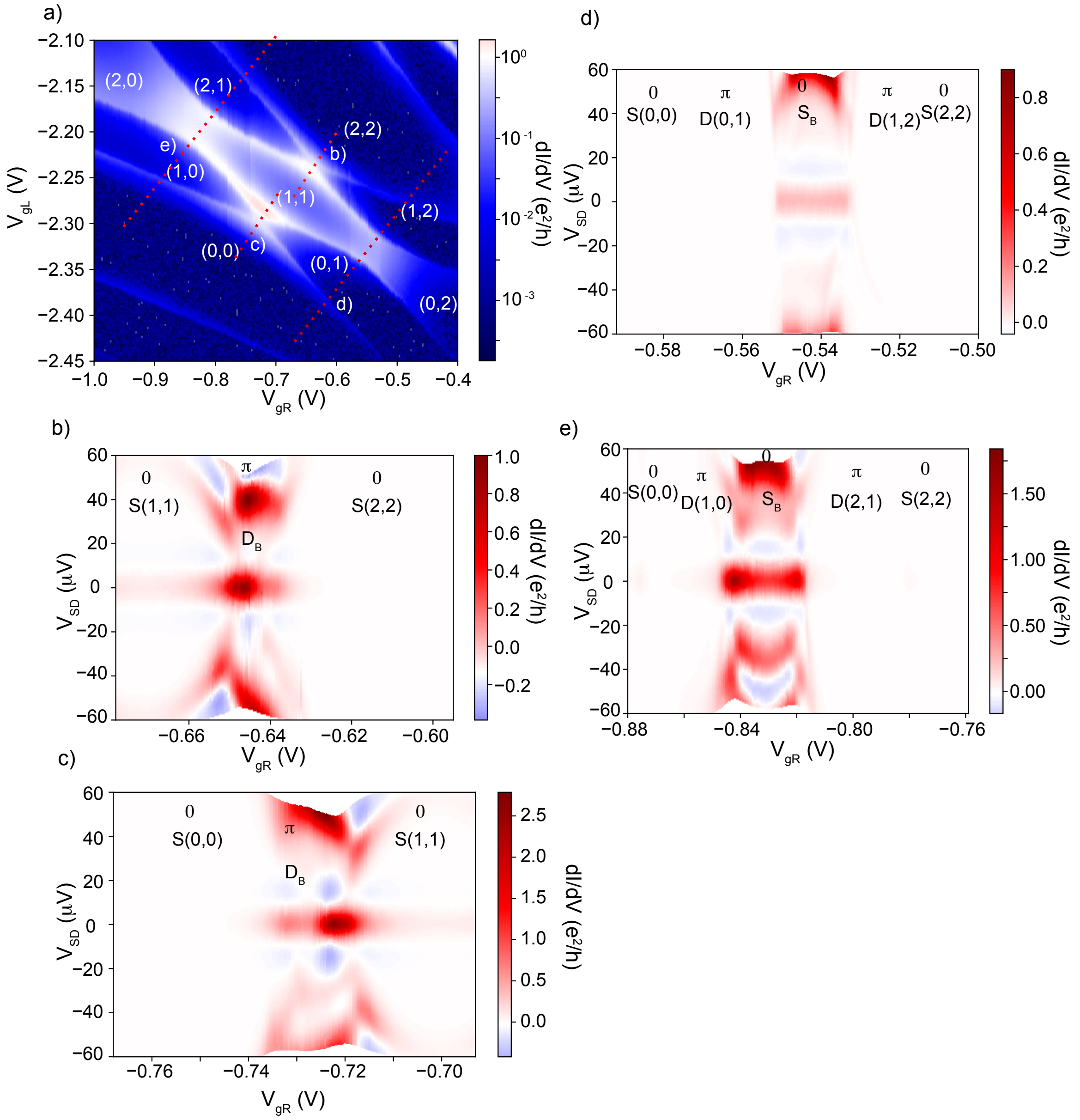

Figure 4.12: a) Charge stability diagram of the DQD. The dashed lines indicate the direction of the shifting traces shown in the following panels. b-c) Bias spectroscopy of supercurrent with the system transiting from a singlet ground state to another singlet ground state through a molecular doublet region. 0 and π correspond to the phase shift of the supercurrent. Panel b) is saturated in conductance at $1\,e^2/h$. d-e) Spectroscopy of supercurrent for the system passing through charge states via a molecular singlet ground state. Supercurrent shows abrupt drops towards the π regions.

would flow through the triple points. Figure 4.12 shows line cuts taken along the four sets of triple points of a (1,1) charge sector. Starting from Fig. 4.12b, the device is initially in the S(1,1) charge state, then enters the hybridized state $|D(2,1) - D(1,2)\rangle$, that is a doublet ground state, and finally reaches the S(2,2) diamond. Interestingly, even though there is a π shift in the current phase relation, the supercurrent is stronger in the molecular region compared to the 0 areas. That behaviour is observed because in the surroundings of the (1,1) sector and mainly in the triple points, the conductance is dramatically enhanced, due to increase in probability of co-tunneling processes. A similar picture can be seen in Fig. 4.12c, which is mirrored since now the trace is moving towards the (1,1) charge sector. Figure 4.12d,e show a different behaviour in the zero bias peak. The system is now tuned from a $|D\rangle$ ground state to another $|D\rangle$, passing through a molecular singlet which is $|S(1,1) - S(0,2)\rangle$ and $|S(2,0) - S(1,1)\rangle$ for Fig. 4.12d and Fig. 4.12e respectively. There are clear transitions in these figures, while on the previous panels we could see an enhancement of the supercurrent in the central region, with the absence of abrupt drops. Qualitatively, the two panels show a similar picture which is expected since the same ground states transitions occur with the same sequence. However, the level of conductance is significantly different, owing to the effect V_{gL} has to the coupling.

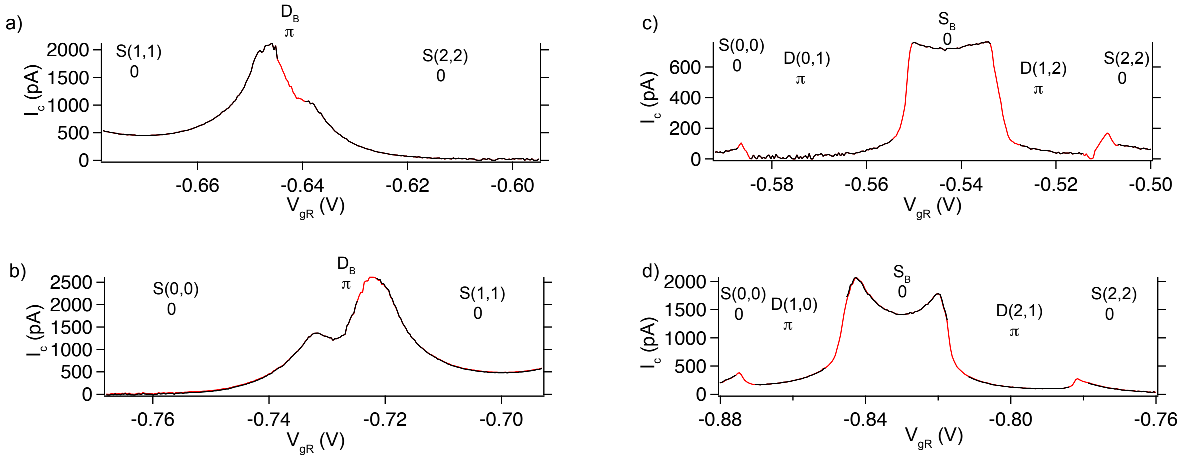

Figure 4.13: a) Fitting of the supercurrent for the plots of Fig. 4.12 with the same sequence as they are presented there. a-b) A strong $I_c \approx 2200\,\mathrm{pA}$ is observed in the doublet region, owing to the fact that it belongs to a triple point area of the (1,1) sector. The supercurrent does not increase abruptly while the system transits from the (1,1) to the D_{B} charge state. c-d) Equivalent traces of Fig. 4.12d-e. Abrupt jumps in supercurrent are now visible when transiting from a doublet ground state to the molecular singlet.

To extract the dependence of I_c in the hybridised states, we fitted the zero-bias peak which confirms the analysis above. Figure 4.13a shows the a trace with the system transiting from the (1,1) charge state, to the molecular $|D(2,1) - D(1,2)\rangle$ and finally reaching the (2,2) hexagon. Supercurrent is maximized in the bonding region with a maximum $I_c = 2000\,pA$. Interestingly, the slope of supercurrent is not so steep, compared to other $\pi \rightarrow 0$ transitions on which an abrupt drop is observed. That is due to an enhancement of the I_c in the triple points. A similar pattern can be seen in Fig. 4.13b, with the DQD now moving towards the (1,1) sector. Note, that there are two strong I_c peaks in the D_B region, with the strongest one belonging to the region closest to the (1,1).

Supercurrent through the other two pairs of triple points is shown in Fig.,4.13c,d. Transitions with low signal such as $S(0{,}0) \rightarrow D(0{,}1)$, $D(2{,}1) \rightarrow S(2{,}2)$ are now captured by the supercurrent, while they were hard to see on the conductance maps. A much more symmetric picture can now be seen in I_c on the S_B region, compared to the respective ones in Figure 4.13a,b. The red parts of the plots are again points on which sub-gap states are corrupting the zero bias peak. Comparing these results to the previous I_c fits of Fig. 4.10 we detect a similar behaviour in the ground state transitions as the abrupt drops are facing the $|D\rangle$ ground state sectors.

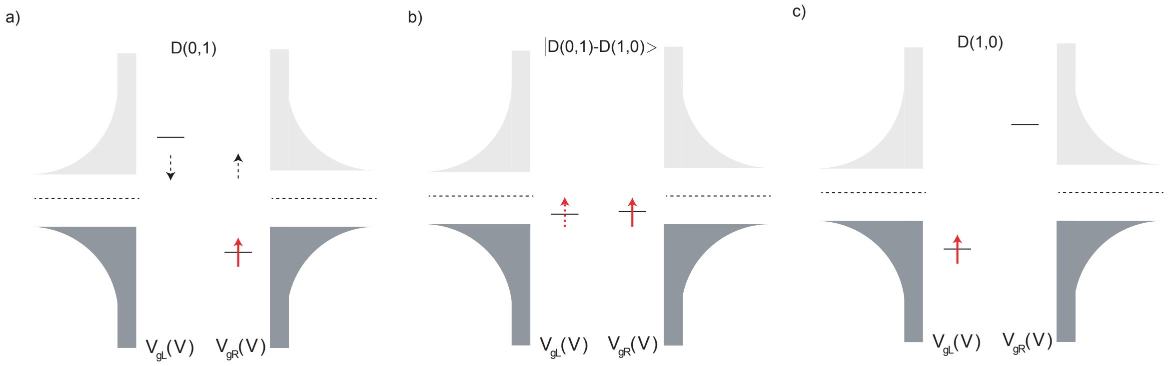

Figure 4.14: Energy diagrams showing the three intermediate steps of a detuning line cut. a) The system is tuned in the D(0,1) charge sector. The two levels represent the highest occupied orbitals, and the red arrowed line represents a spin up electron occupying the right QD. Dashed arrowhead lines show the direction the levels move. The plunger controlling the left QD is increasing in voltage, while the one controlling the right is decreasing. b) The two levels are aligned in the vicinity of the triple points. In the hybridised molecular state, the electron fluctuates between the two QDs. That process is described with a dashed red arrow. c) D(1,0) charge sector. The two levels are again out of resonance as the DQD is tuned away from the triple points line.

In addition to the tuning cuts, we have also measured the dependency of the supercurrent through the detuning lines of the DQD. In the tuning plots shown previously, both levels of the QDs are aligned, leading to enhanced conductance between the triple points. However, if we are detuning a DQD, we are having the levels in diametrical positions. As the sweep begins, one level is pushed at lower electrochemical potential, while the other is pushed at higher. As sketched in Fig.4.14. Figure4.14b shows that near the triple points the two levels are aligned, enhancing transport processes. Specifically, we measured the supercurrent as the system transits from the D(0,1) charge sector to the D(1,0), passing through the molecular doublet ground state D_{B}. The magnitude of I_c showed a significant increase on the molecular doublet region, owing to more active transport channels in that gate-space in comparison to the D(1,0) and D(0,1) hexagons.

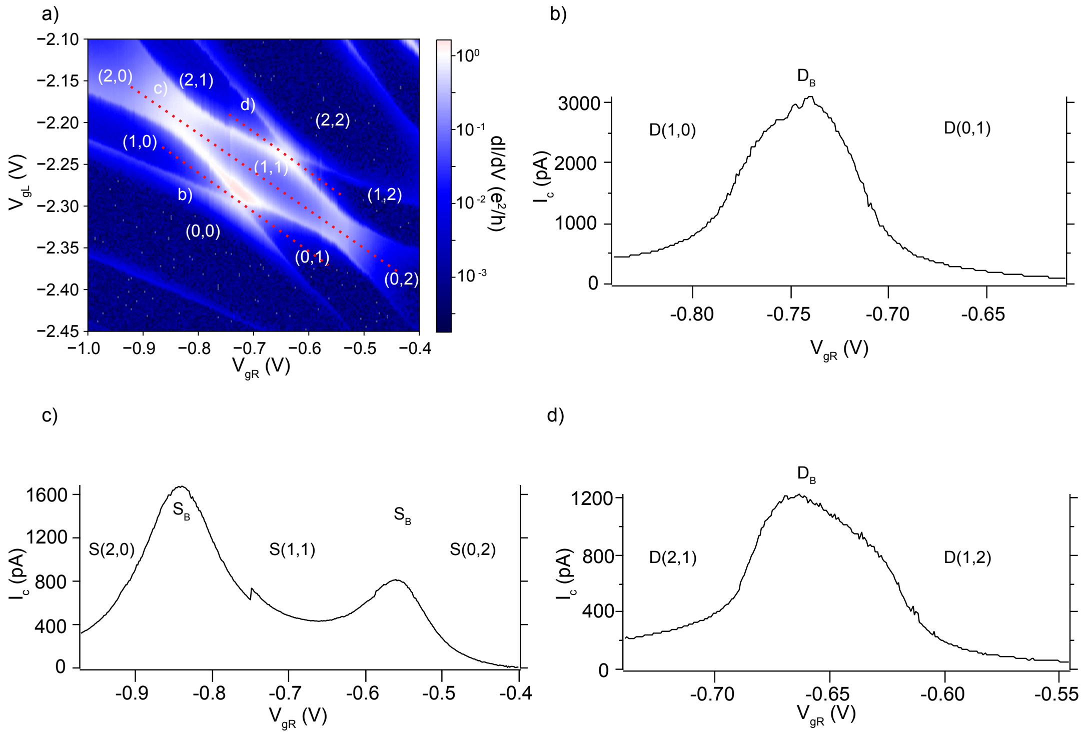

Figure 4.15: a) Zero bias conductance map of the studied DQD. Dashed lines indicate the direction of the fitted I_c cuts shown in the following panels. b) Fitted I_c for the device transiting from the D(0,1) to the D_B and finally to the D(1,0) charge state. I_c shows a peak on the molecular doublet region. c) Fitted I_c through the (1,1) charge sector. Again, I_c shows peaks when the device is in the molecular singlet state. d) The last detuning cuts shows analogous behaviour to panel a) for the three electron case.

Similarly, the behaviour of the supercurrent shows same qualitative results through the other molecular doublet between the D(1,2) and D(2,1) charge sectors. Moreover, we measured the supercurrent dependence along the detuning line crossing the S(1,1) sector, to study the 2 electron regime. In a similar pattern, supercurrent is enhanced near the triple points at the singlet bonding area S_{B}. The bias spectroscopy measurements are included in Appendix A.

Fig. 4.15 shows the supercurrent cuts for the detuning measurements of the DQD. It is observed that although each measurement does not show any I_c transition, the supercurrent shows local maxima on the hybridized regions. In Fig.4.15a the device is tuned through the hybridised doublet state. Supercurrent is enhanced showing a clear peak, even though the ground state is maintained. Moreover, Fig. 4.15b shows supercurrent the cut through the (1,1) charge sector, that demonstrates similar behaviour to the previous panel, as I_c is strong in the vicinity of the triple points. These results underline the difference of a serial double quantum dot in comparison to a single QD. The fact that I_c is enhanced near the triple points indicates that the behaviour of the DQD is not trivial, as the addition of a second quantum dot is not simply the addition of another level, but it adds extra complexity and new properties on the system.

4.7 Sub-gap states spectroscopy

A different way of identifying ground state transitions in a quantum dot system is by studying the sub-gap states and how they behave on the charge degeneracy points. In the proximity of a single level (i.e. quantum dot) near a superconductor, discrete levels are formed inside the superconducting gap, which are known as sub-gap states. For the device that we studied, the superconducting gap is much weaker than the charging energy $\Delta \ll U$, giving rise to Yu-Shiba-Rusinov sub-gap states [1, 2, 3]. As we have discussed in Chapter 2, we expect sub-gap states to create a loop as they cross zero-bias, for $|S\rangle \rightarrow |D\rangle \rightarrow |S\rangle$ ground state transitions. However, in our case the presence of the superconducting gap has pushed the features away from zero-bias. We no longer see crossings of sub-gap states but the loop-like behaviour indicates the ground state transition.

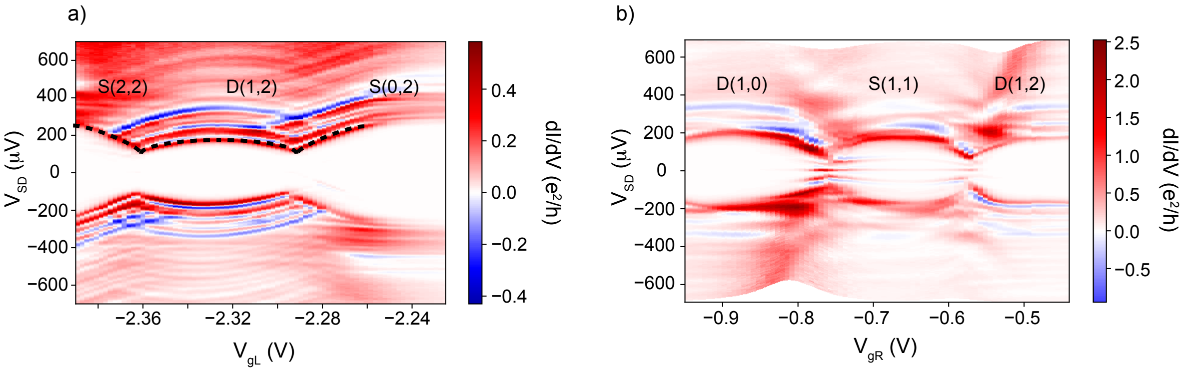

Figure 4.16: High bias conductance maps corresponding to the supercurrent measured in Fig. 4.9. a) Bias spectroscopy through the D(2,2), S(1,2) and D(0,2) charge states. The sub-gap states follow a loop structure indicating the same transitions shown by supercurrent. It can be seen that a large number of sub-gap states exist above 300 μV, which are separated by thin lines of NDC. The green line is a guide showing the loop-like behaviour of the sub-gap state. b) The DQD is transiting through the D(1,0), S(1,1) and D(1,2) charge sectors. The sub-gap states are again forming a loop indicating a $|D\rangle \rightarrow |S\rangle \rightarrow |D\rangle$ transition.

In this section I will present the higher bias measurements that show the sub-gap state behaviour when the DQD is transiting through charge states, i.e. $|D\rangle \rightarrow |S\rangle$. Figure 4.16 shows two equivalent conductance traces of supercurrent shown in Fig. 4.9, but for a larger source-drain window $V_{SD} = \pm 0.7\,\mathrm{mV}$. Figure 4.16a shows the DQD transiting through the S(2,2), D(1,2) and S(0,2) charge states, while Figure 4.16b the device is tuned from the D(1,0), to the S(1,1) and finally to the D(1,2) sector. On each panel, a loop is formed indicating ground state transitions. These findings support the findings of the fitted I_c, as both methods give signatures of transitions.

In addition, on Figure 4.16b in the S(1,1) sector, sub-gap states crossing zero are visible, which cause the bad fittings of the supercurrent as seen in the previous figures.

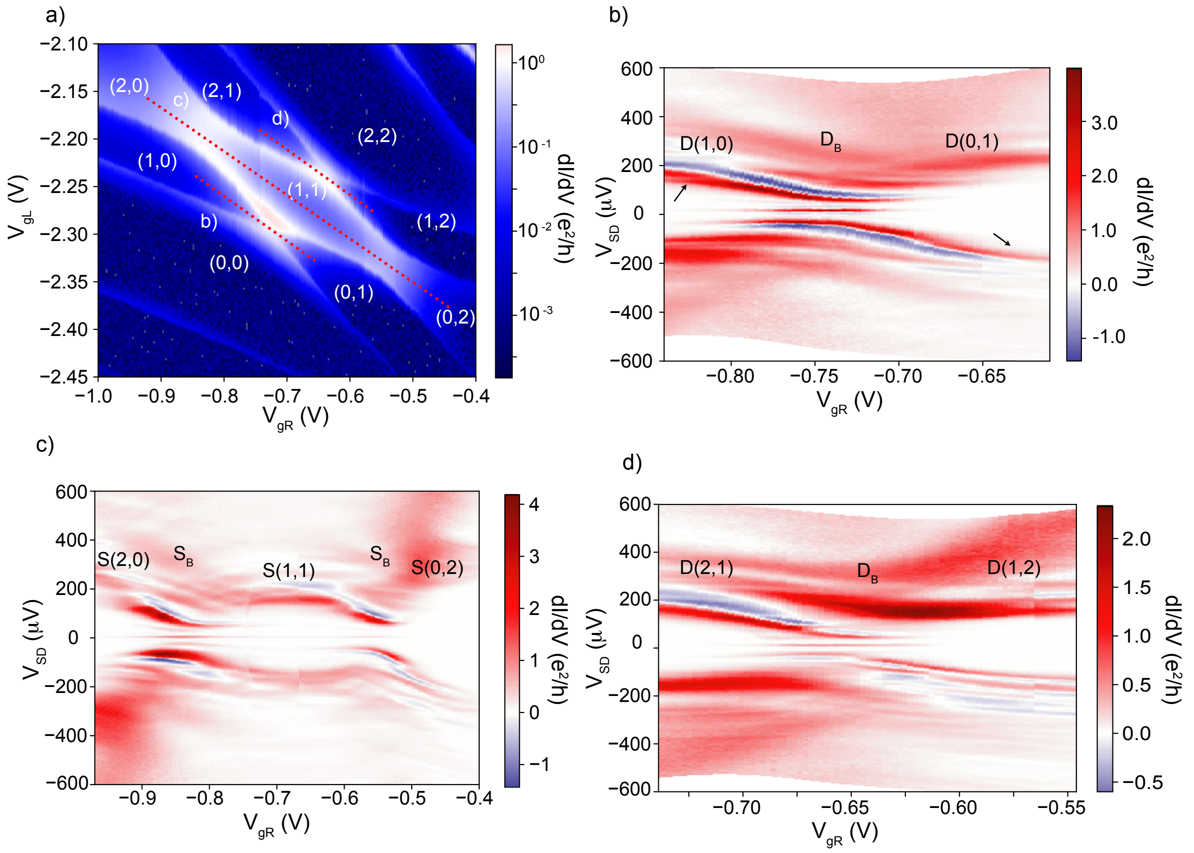

Figure 4.17: a) Charge stability diagram of our DQD. Red dotted lines show the trajectories of the next panels, measuring the dependance of the sub-gap states at the detuning lines. b) sub-gap states spectroscopy along the detuning line connecting the D(1,0) and the D(0,1) charge states. As the system passes through the molecular doublet ground state $|D(1,0) - D(0,1)\rangle$, the sub-gap states have an avoided crossing. Interestingly, the sub-gap states are not symmetric in respect to applied bias. Black arrows show the points at which the sub-gap states are much more conductive with comparison to opposite bias. c) Detuning line for the 2 electron regime passing through the (0,2) (1,1) and the (2,0) charge states. The ground states is a singlet across the line, and the sub-gap states are anti crossing verifying that there is no ground state transition. d) Detuning cut for the last set of triple points. The results are similar to panel b, as we see the sub-gap states anti-crossing. The asymmetry in bias is also present here.

Moreover, in Figure 4.16a a large number of sub-gap states is visible, especially at high bias, giving the impression of ‘replca’. Frolov et al. [40] speculate that a presence of a soft gap on both leads can produce such a picture, however our superconducting gap spectroscopy showed a ‘clean’ gap with no visible states between ±2Δ. Due to high complexity and number of the sub-gap states, it was much harder to interpret and analyze each and every feature, especially with applied magnetic field, since that would split the sub-gap states and create an even more complex picture.

Furthermore, measurements of the detuning lines at high bias are shown in Fig. 4.17. These are the measurements for the lines depicted in Fig. 4.15a. Panels b and d show a new feature concerning the sub-gap states in comparison to the previous figure. Away from the molecular bonding state, there is a distinctive asymmetry in the conductance of sub-gap states in respect to bias. The left black arrow in Fig. 4.17b reveals that the sub-gap state at positive V_{SD} is much more conductive in comparison to the negative one. This behaviour could hint an electron-hole asymmetry for the system. Specifically, we speculate that relaxation processes trigger that effect. Quasiparticles in the sub-gap state could relax to the continuum of the superconductor and that can cause conductance enhancement. Similar indications of bias asymmetry have been studied in other S-DQD-N devices [14].

4.8 Conclusions

To summarize, we studied a S-DQD-S junction defined in a nanowire with epitaxial Al leads. By measuring the conductance of the system while it transits to different charge sectors, we have seen a consistent increase in the supercurrent when a $|S\rangle$ sector is near a parity-change line. On the other hand, when the system transits to a $|D\rangle$ ground state sector, supercurrent abruptly decreases, indicating a $0 \longrightarrow \pi$ transition in the current-phase relation $I_s = I_c \cdot sin(\phi + \phi_0)$. In general, when the total charge in the dots is an odd (even) number, the ground state is a doublet (singlet). Fitting of supercurrent verified the claim of these transitions, and it is also in accordance with a theoretical model shown in Fig. 4.18, developed by our collaborators.

Ongoing work by our collaborators Gorm Steffensen and Jens Paaske has shown very good agreement in modeling the critical current I_c, using the same parameters we extracted experimentally (U, Δ).The transitions are well captured and show consistent behaviour in all traces. Note that in Fig. 4.18a,c the red colour implies positive I_c while the blue negative.

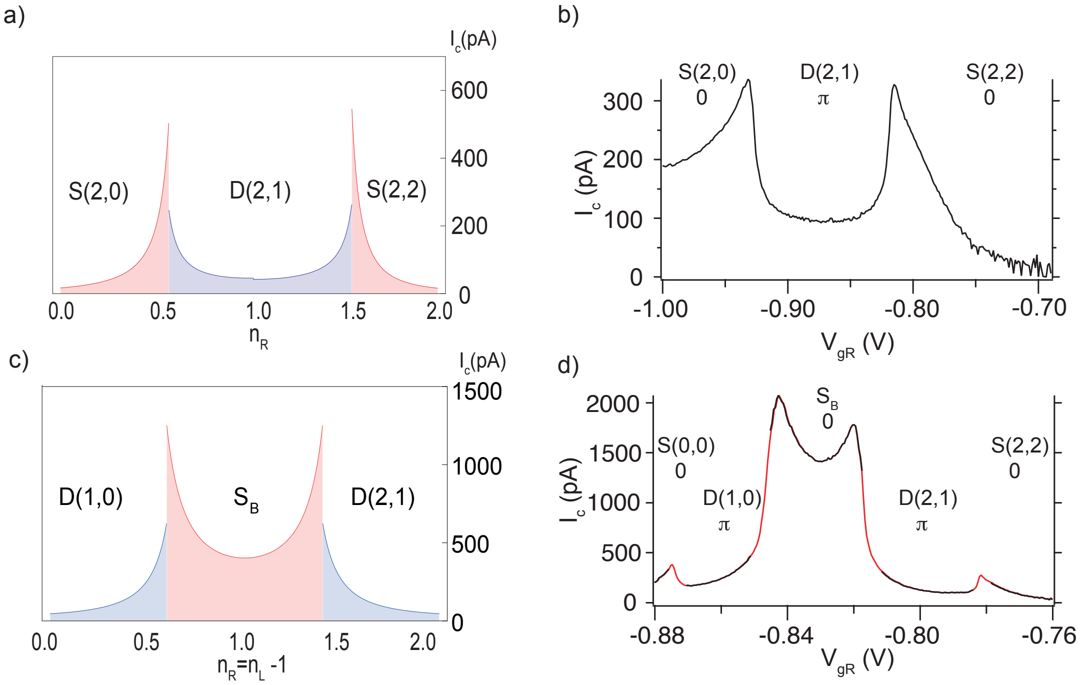

Figure 4.18: Direct comparison of $|I_c|$ calculated by fourth order perturbation theory (a,c) to the fitted supercurrent from our measurements (b,d). n_R, n_L refer to the occupation of the right and the left QD respectively. a) Line-cut of $|I_c|$ calculated with fourth order perturbation theory for the DQD transiting from the (2,0) to the (2,1) and finally to the (2,2) charge sector. Red colours implies positive critical current, while blue negative. b) Extracted $|I_c|$ via the extended RCSJ model for the corresponding charge states of panel a. c) Fourth order perturbation theory line-cut through the 'molecular' singlet ground state. d) Equivalent fitted $|I_c|$ of panel c. Interestingly, there is a clear qualitative similarity of the transitions between theory and experiment. In the theoretical model the drops of I_c show the same behaviour as in the fits.

Chapter 5

YSR screening of spins in a Double Quantum dot

5.1 Introduction

This chapter will cover the first set of measurements regarding screening of spins in a double quantum dot (DQD), realising the two-impurity Anderson model [41] coupled to superconducting (S) leads. The physics of impurities in close proximity to superconductors has been studied extensively [1, 2, 3] and a variety of interesting physics have been explored when coupling such an impurity to a superconducting material. In 2017 and 2018, the first studies involving DQDs coupled to superconducting leads in nanowire based devices were reported [14, 37]. These nanowires, being made of semiconductors whose charge density can be modified through gating, give the possibility of tuning the inter-dot coupling and exploring its influence on screening effects. In our project, we defined a DQD system embedded between two superconducting leads, creating the opportunity to screen both QDs. By measuring the supercurrent through the device we could identify the ground state transitions that happen via the phase changes $0 \rightarrow \pi \rightarrow 0$ of the supercurrent. Thus, we could determine whether the magnetic impurity (spin 1/2 of a QD) was screened by quasiparticles in the continuum of a superconducting contact. The following findings will result in a publication.

In the beginning of this chapter, I shall introduce again the honeycomb regime of a DQD with superconducting contacts. Then, I will talk about the steps we made to increase the coupling to the superconductors and observe screening of spins in the DQD. Specifically, we studied three cases:

- Screening of a single spin in the left QD
- Screening of the $|T_{11}\rangle$ by the left S
- Simultaneous screening of both QDs

5.2 Tuning the device

It should be noted that the device used to demonstrate the screening is the same one used to study the honeycomb regime of the double quantum dot. In fact, the same set of nine charge sectors shown there will be tuned here. However, in order to tune it to the screening regimes it was required to increase the coupling to the leads Γ_L,Γ_R to be in the intermediate regime $\Gamma \sim U$. In the honeycomb regime, the condition $\Gamma \ll U$ was satisfied. Our first goal during this experiment was to increase the coupling to one of the two leads and by measuring the zero bias conductance of V_{gL}-V_{gR} maps, observe how the honeycomb pattern behaves. Hence, we started by increasing the voltage of the gate controlling the tunnel barrier to the left lead, which will be abbreviated as V_{g1}. We should also keep in mind that our system is not ideal, and that bottom gates communicate with the two QDs with cross-capacitance. As a result, for every small voltage change of a tunnel barrier, the closest QD is also affected, 'moving' the V_{gL}-V_{gR} position of the DQD. Moreover, as we have also discussed on the previous chapter, the coupling throughout the gate-space is not constant, leading to conductance shifts across the DQD, and in some cases to curved parity change lines -which should not be seen according to theory. To visualise the system, a schematic is illustrated in Fig. 5.1. For the scenario that the left dot has 1 electron in its highest level and the right one has none, then the ground state is a degenerate doublet $|D\rangle$. However, if the coupling to the left lead increases, quasiparticles of the S lead screen the magnetic impurity and the excited state -Yu-Shiba-Rusinov (YSR) singlet $|S_{YSR}\rangle$- becomes the ground state [14, 42, 43]. As seen in Figure 5.1 the quasiparticle at energy E_b couples with the spin of the QD forming the excited state $|S_{YSR}\rangle$, depicted with the cyan ellipse. Hence, by increasing the tunnel coupling to the S lead, the sub-gap state moves closer to zero bias, and it becomes the ground state when it crosses the energy of the degenerate doublet $|D\rangle$.

5.3 Screening of single spin in left QD

Figure 5.2a-c shows subsequent charge stability diagrams with a stepping V_{g1}, increasing its voltage by 0.1 V for each plot. Initially, the gates are set to the following configuration: $V_{\mathrm{g1}} = -9.2\,V$, $V_{\mathrm{g3}} = -9\,V$, $V_{\mathrm{g5}} = -0.36\,V$, $V_{\mathrm{bg}} = 11\,V$ while the other two gates are the QD plungers. The superconducting gap remains in the limit $\Delta \ll U$ which is a requirement to see YSR sub-gap states. It is important to first remind ourselves of the ground states of each charge hexagon in the honeycomb regime. As we have discussed in the previous chapter, the occupation of the QDs alter the ground state of the system. Even number of electrons in each QD provide a singlet ground state, while odd a doublet. An exception is the (1,1) charge sector as the two electrons couple with exchange interaction and form a singlet ground state. In this section, we demonstrate screening of singly occupied QDs with the aim of reducing their spin via coupling with the superconducting leads.

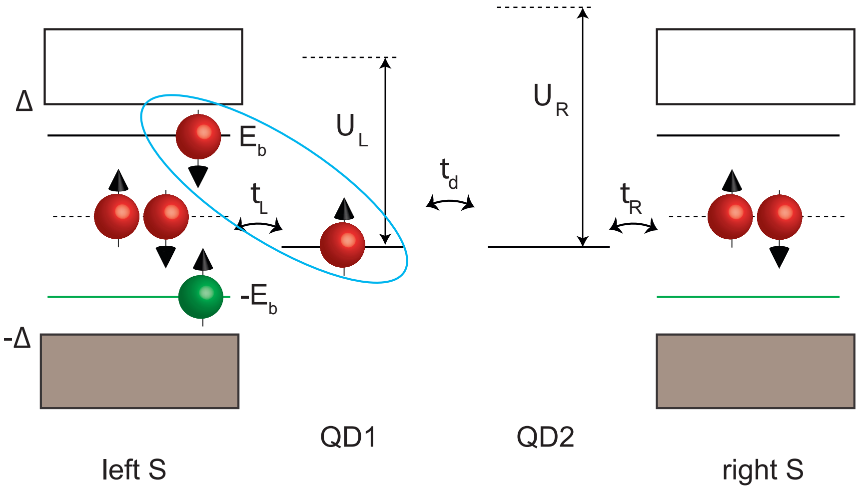

Figure 5.1: Energy diagram for a double quantum dot. The left and the right QDs, noted as QD1 and QD2 respectively, are contacted by two superconductors (S). At energies $\pm E_b$ sub-gap states are formed which are filled with a quasiparticle. The green sphere represents a hole. t_{L} and t_{R} represent the tunnel coupling to each lead and t_{d} the inter-dot coupling. The total charge number of the DQD is (1,0), as the left dot has 1 electron on its highest orbital while the right one has none. However, the system moves from its ground state $|D\rangle$ to the first excited $|Y_{YSR}\rangle$ as the quasiparticle at the bound state couples with the electron and forms a singlet.

Figure 5.2a shows the DQD stability diagram, where the white arrows indicate the transition for changing the ground state. Increasing the coupling to the left S makes these lines go closer(panel b, see arrows) and eventually disappear (panel c). That implies that there is a ground state transition, (D(1,0)→ S_{YSR}) which is induced by increasing the tunnel coupling, as described in the theory section. As shown in Fig. 5.2c, the ground state through the (2,0),(1,0),(0,0) line is maintained to a $|S\rangle$. Moreover, an interesting observation in Fig. 5.2c is that there seems to be a parity-change line between the S_{YSR} and the S ground state of the (1,0) and (1,1). Due to the Josephson junction nature of the system, supercurrent is enhanced when the current-phase relation is on the 0-phase. Hence, when the (1,0) sector suffers a ground state transition $|D\rangle \rightarrow |S_{YSR}\rangle$, then co-tunneling process are enhanced and we observe stronger conductance in comparison to panel a where the (1,0) sector has a $|D\rangle$ ground state. It is important to remember that the zero bias conductance maps not only reveal ground state transitions, but also include signatures of supercurrent.

To support the claim of screening, we measured bias spectroscopy of the supercurrent (zero-bias peak) flowing through the DQD, as well as fitted the critical current I_c with the same fitting procedure followed in the previous chapter [27]. In fact, we now use the supercurrent as a tool of identifying ground state transitions. Figure 5.3 shows traces passing through the (2,0), (1,0) and (0,0) sectors following the dashed lines of Fig. 5.2a-c. The left column of Fig. 5.3 presents a clear V_{g1}-gate dependence of the doublet region. As the tunnel coupling increases, the distance between

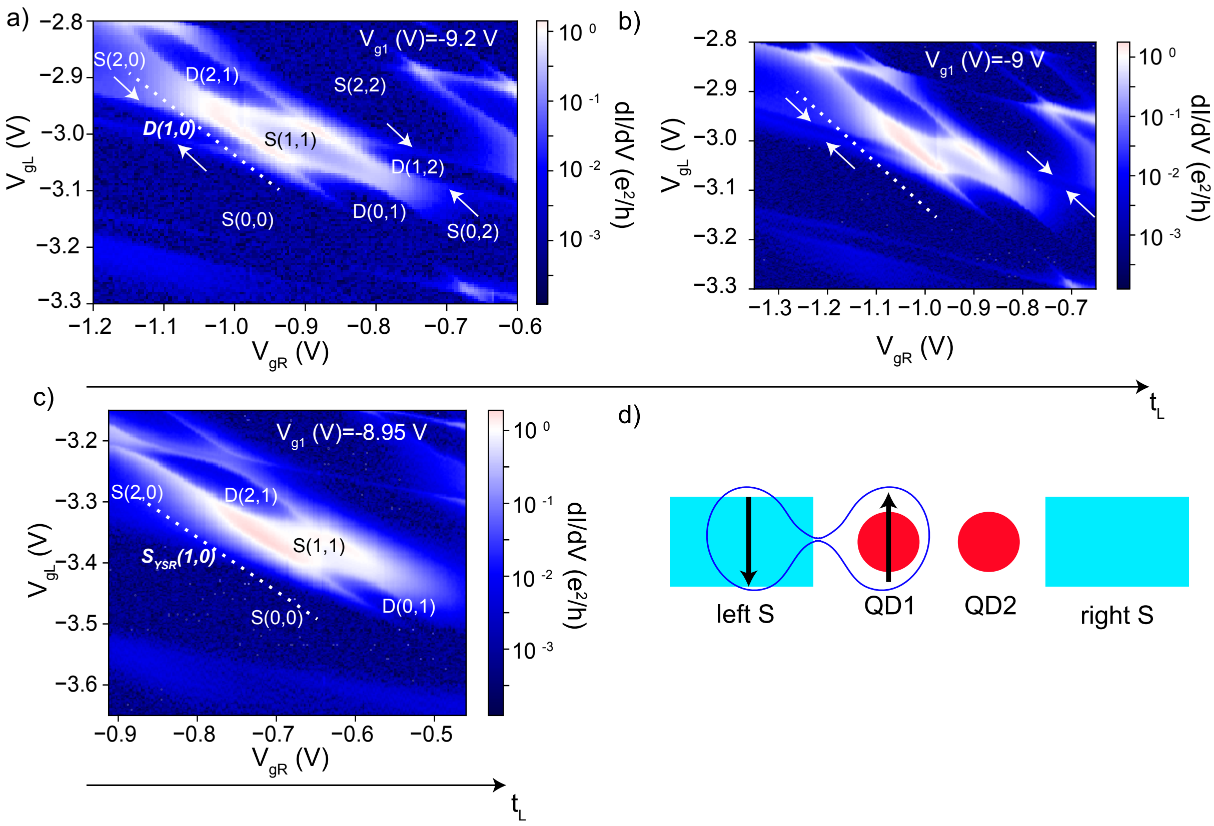

Figure 5.2: Zero bias charge stability diagram for different t_L which is controlled by V_{g1}. Numbers in parentheses (n,m) indicate the charge number of the left and the right QD. S and D correspond to singlet and doublet ground state. a) Initially $V_{g1} = -9.2\,V$ and it is clear that the DQD is on the honeycomb regime, as the parity lines are well separated. b) $V_{g1} = -9\,V$; an increase of the tunnel coupling to the left lead pushes the parity lines separating the (2,0)-(1,0) and (1,0)-(0,0) sectors closer together. c) $V_{g1} = -8.95\,V$. No clear zero bias peak resonance can be seen through the (2,0)-(1,0)-(0,0) line and to the analogous one (2,2)-(1,2)-(0,2). This is a hint of successful screening of the spin on the left QD. The dashed lines show the direction of the bias spectroscopy plots that are presented in the next figure. d) Schematic illustrating the screening of the left QD by the left superconductor, resulting in a singlet ground state.

the two singlet sectors (0,0) and (2,0) decreases, eventually merging on panel c (see red arrows). Note how the visible sub-gap states at high bias no longer cross $V_{SD} = 0$ but they anti-cross on Fig. 5.3c.

The right column of Fig. 5.3 shows the corresponding critical current of the zero bias peak, as calculated in the previous chapter [27, 36]. The fits verify the intuition that a coupling induced phase transition occurs, as it is clear that the doublet region shrinks. Moreover, on Fig. 5.3e it is observed that the critical current in the doublet region has significantly increased, hinting the merging of the two singlet regions. The maximum I_c measured is significantly stronger when the screening is complete. Both the conductance in Fig. 5.3c and the fitted I_c in Fig. 5.3f are much higher compared to the previous panels. We attribute this supercurrent enhancement to the $\pi \rightarrow 0$

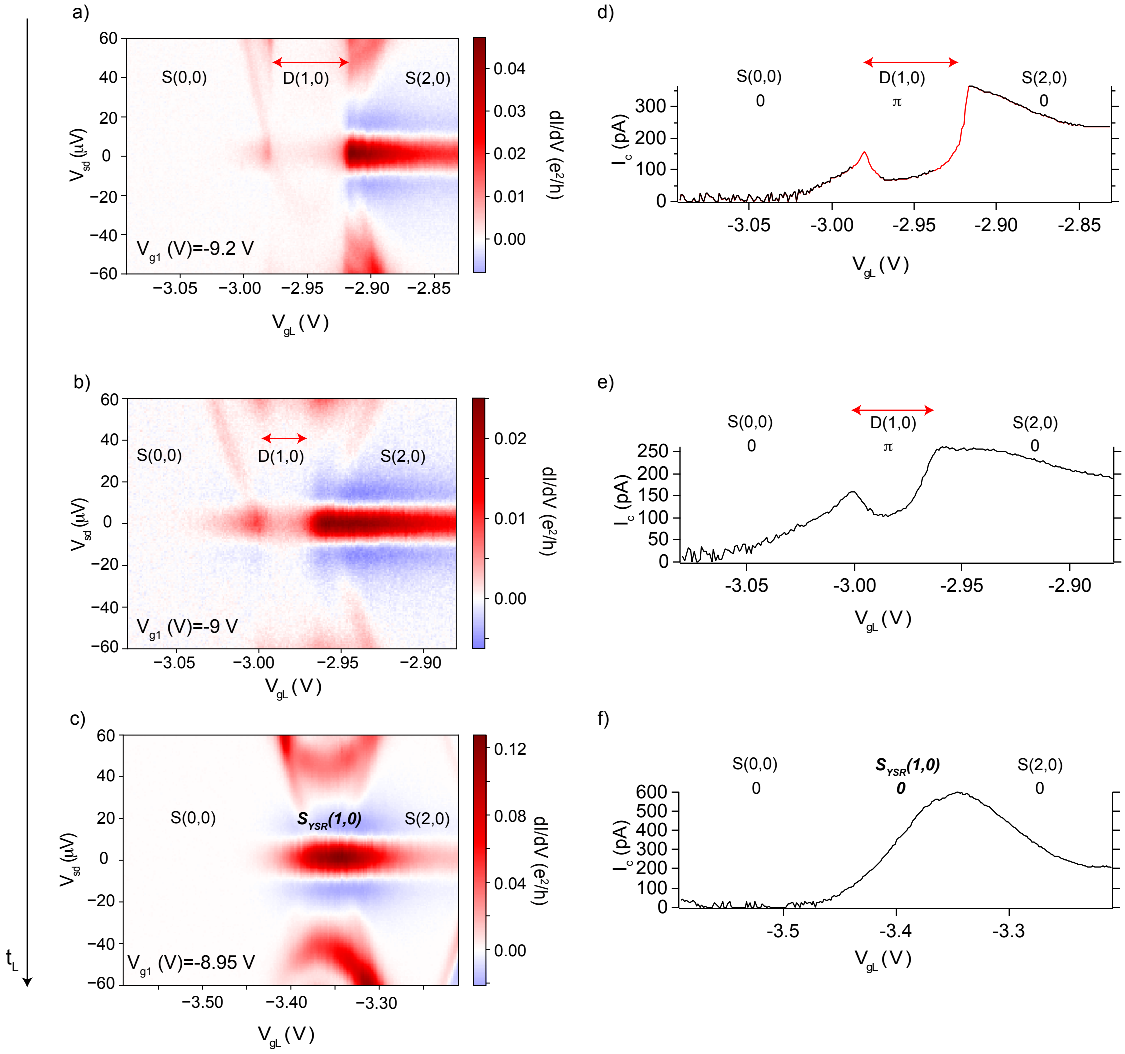

Figure 5.3: a-c) Bias spectroscopy revealing the dependence of the zero-bias supercurrent peak to the change of tunnel coupling. a) Initially the device is tuned to the honeycomb regime, where $\Gamma \ll U$. Here, the doublet ground state (1,0) is well defined. As the device is tuned from the (2,0) to the (1,0) and finally to the (0,0) charge sector, abrupt walls of conductance are seen which indicate $0 \longrightarrow \pi$ transitions. b) An increase of the tunnel coupling has made the D(1,0) region smaller, as it is also observed in the zero bias conductance map. c) Screening of the left QD spin is observed. At $V_{g1} = -8.95\,V$, the ground state of the (1,0) sector has changed to a Shiba singlet S_{YSR}, as the zero bias peak is continuous without abrupt changes. d-e) Equivalent I_c fits of the first column panels. d) Red points show traces where the fitting was not optimal due to sub-gap states crossing zero bias. e) I_c fitting of panel b. The shrinking of the doublet region can be seen and the abruptness of the I_c transition has been decreased significantly. f) Fitted I_c for panel c. No sign of $0 \longrightarrow \pi$ transition is visible. We attribute this change to a $|D\rangle \longrightarrow |S_{YSR}\rangle$ transition of the (1,0) charge sector.

transition of the current-phase relation $I = I_c \cdot sin(\phi + \phi_0)$. Note, that as the (1,0) sector is tuned towards the screened singlet, the sub-gap states move away from zero bias and the fitting becomes more accurate (no red points on Fig. 5.3e,f.).

In summary, by increasing the tunnel coupling to the superconducting lead it is possible to screen the $S = \frac{1}{2}$ state ((1,0) charge sector) and create a YSR singlet state, which was proven by identifying the current-phase relation of the supercurrent. This regime is called partly screened (PS) regime of the left dot [14]. Demonstrating the intermediate steps between the honeycomb regime and the screening of a singly occupied QD, is consistent with Fig. 2.13 which shows a gradual modification of the parity change lines when Γ_s increases for a S-QD-S system.

5.4 Screening of the triplet excited state by left S

It is interesting to study the behaviour of the S(1,1) charge sector under influence of t_L and inter-dot coupling t_d. One might wonder why would a superconductor get involved in screening a $S = 0$ state, as it cannot be considered as a magnetic impurity. However, by tuning the coupling to the S lead it is possible to screen the excitation of the S(1,1) which is the triplet T(1,1) with $S = 1$ [14]. The exchange energy J provides the difference in energy between the singlet and the triplet state. That way, a reduction of spin happens by $S = \frac{1}{2}$ and the ground state is a $|D_{YSR}\rangle$. It is now more clear why the (1,1) sector is special compared to the doublet ground state charge sectors (1,0), (1,2). In this project, we have managed to demonstrate screening of either the left, or the right QD by tuning the t_L or t_R respectively. Of course, the inter-dot coupling plays an important role to this process. t_d governs the magnitude of the exchange interaction, and thus for smaller t_d, the easier it is to screen one of the electrons of the (1,1). Figure 5.4 shows two qualitative energy diagrams that describe the dependence of the ground state in the (1,1) charge sector to the coupling to the superconductor t_s and the inter-dot coupling t_d. In Fig. 5.4a, as the coupling to the lead increases, the excited state $|D_{YSR}\rangle$ starts from the superconducting gap and reaches zero energy at a finite coupling strength. At that point, a transition occurs $|S_{11}\rangle \rightarrow |D_{YSR}\rangle$. For even larger t_s both the excited triplet and the singlet ground states increase in energy, while the doublet remains at zero. Figure 5.4b describes a phase diagram of a DQD with respect to t_d and coupling to the left S t_L. Following our intuition, for strong inter-dot coupling t_d and at a finite t_L, the (1,1) sector is in the $|S\rangle$ ground state, as the exchange interaction J is strong. That is the partly screened regime that we studied in Fig. 5.2 and is depicted with the black arrow tuning t_L. With a combination of stronger t_L and weaker t_d it is possible to see a ground state transition in the (1,1) sector $|S_{11}\rangle \rightarrow |D_{YSR}\rangle$. For simplicity, we call this ‘screening regime’.

We now focus on the task of screening the electron of the left QD, in the (1,1) charge sector. We succeed in that by tuning two parameters. We can increase the coupling to the superconductor, by further increasing $V_{\mathrm{g}1}$ and effectively weakening the barrier between the lead and the QD.

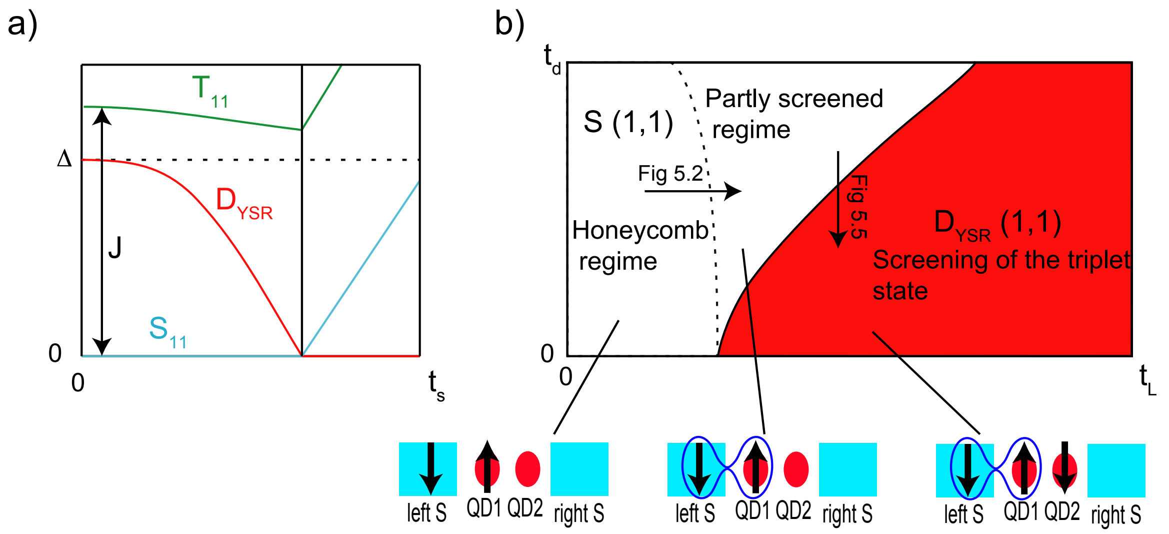

Figure 5.4: a) Qualitative diagram of the ground state $|S_{11}\rangle$ and the excited states $|T_{11}\rangle$, $|D_{YSR}\rangle$ of the (1,1) of a DQD with superconducting leads. It should be noted that on our experiment we only increased the tunnel coupling to the left lead, which we describe as t_L, while the coupling to the right lead which affects the right QD is kept at the weak coupling limit. The energy difference between the $|S_{11}\rangle$ and the $|T_{11}\rangle$ is given by the exchange interaction J. As the coupling to the superconductor t_s increases, the energy of the $|D_{YSR}\rangle$ drops, until it crosses zero and becomes the ground state of the system. This shows the process of screening of the excited $|T_{11}\rangle$ to the $|D_{YSR}\rangle$, reducing the spin from $S = 1 \rightarrow S = \frac{1}{2}$. b) Phase diagram of a S-DQD-S with respect to the inter-dot coupling and the coupling to one superconductor. For the sake of the argument we keep the coupling to the other superconductor minimal. As described in the previous chapter, for low t_L the system is in the honeycomb regime. For larger t_L, then depending on the inter-dot coupling, screening of the $|T\rangle^{11}$ can occur. The transition of the partly screened to the screening of the triplet state is sketched with the black arrow and measurements are shown in Fig. 5.5. Adapted from [14].

Moreover, we can decrease the voltage of V_{g3} with the aim of making the barrier between the two QDs more opaque, resulting in smaller exchange coupling. Hence, it should be possible to observe screening of the left spin, as it would cost less energy to excite to the $|T_{11}\rangle$ state. Figure 5.5 shows two charge stability diagrams of the same (1,1) sector at a different t_L and t_d. In Fig. 5.5b we see the charge stability diagram for the DQD at a lower inter-dot coupling. It can be seen that only two parity-change lines are visible. These two lines separate the system to singlet and doublet ground state domains. Specifically, the left row which consists of the (0,0), (1,0) and (2,0) charge states has $|S\rangle$ ground state. That was also the case in the partly screened regime. However, the middle row (2,1), (1,1) and (0,1) also appear to have the same ground state now, as the (1,1) sector has been successfully screened. Interestingly as soon as the ground state of the (1,1) is changed to $|D_{YSR}\rangle$, the enhancement of I_c in the surroundings of the (1,1) is suppressed.

To verify the argument that the electron of the left QD has been screened, we fitted the supercurrent through the (1,1) diamond to see whether the I_c behaviour comes in accordance with the stability diagrams. In Fig. 5.5c,d the equivalent fitted I_c can be seen. Two clear arguments

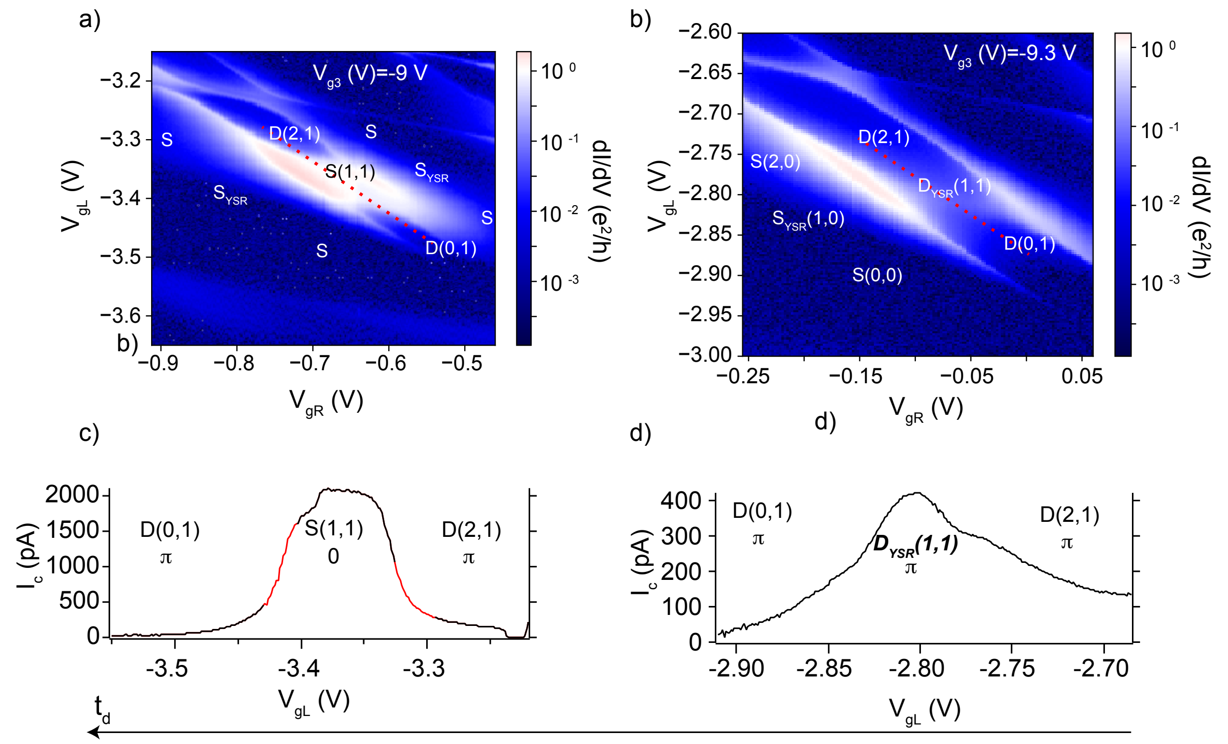

Figure 5.5: a) Charge stability diagram for the our S-DQD-S device at the partly screened regime, as it is visible that there is no parity-change line visible in the (2,0),(1,0),(0,0) line. The gate that controls the inter-dot coupling is set at $V_{g3} = -9\,V$. b) Measurement of the DQD at a lower t_d, $V_{g3} = -9.3\,V$. Now, through the (2,1)-(1,1)-(0,1) line there is no parity-change line, as we have a transition $|S_{11}\rangle \longrightarrow |D_{YSR,11}\rangle$. The ground state is maintained through the red dashed line, as the device shifts to the screened regime [14]. c,d) Fitted supercurrent for the red dashed lines of the previous panels. As the (1,1) sector suffers a ground state transition, the abrupt jumps of conductance smoothen, which is captured as a $0 \longrightarrow \pi$ transition of the supercurrent. The amplitude of I_c is significantly reduced, as expected for a $|D\rangle$ ground state.

can be given that support the phase transition $|S_{11}\rangle \longrightarrow |D_{YSR,11}\rangle$. Firstly, the abrupt walls of I_c in panel c are replaced by smooth 'hills' in panel d as the DQD is tuned from the (0,1) to the (1,1) and finally to the (2,1) charge state. Moreover, the decrease of I_c is a sign of a $|D\rangle$ ground state. Note, that the absence of unreliable fitted points in Fig. 5.5d supports the claim that there is no ground state transition throughout the measurement, since the sub-gap states do not cross zero bias when there is no transition. Zero-bias peak measurements that were used to extract I_c are shown in Appendix A.2.

We also measured the high bias conductance revealing the sub-gap states behaviour of the two regimes. Figure 5.6a shows a high bias spectroscopy measurement of the partly screened regime, with the DQD being tuned from the (0,1) to the (1,1) and finally to the (2,1) charge sectors. Complementing the supercurrent measurements, it is observed that the sub-gap states are undergoing a ground state transition $|D\rangle \longrightarrow |S\rangle \longrightarrow |D\rangle$ (black arrows). The two arrows indicate the position where the ground state transition happens. In contrast, Fig. 5.6b shows the sub-gap states of the same charge sectors anti-crossing instead of forming a loop. That is an indication that a ground state transition occurred in the (1,1) sector $|S\rangle \longrightarrow |D_{\text{YSR}}\rangle$. Hence, the electron of the left QD is screened by the superconducting lead.

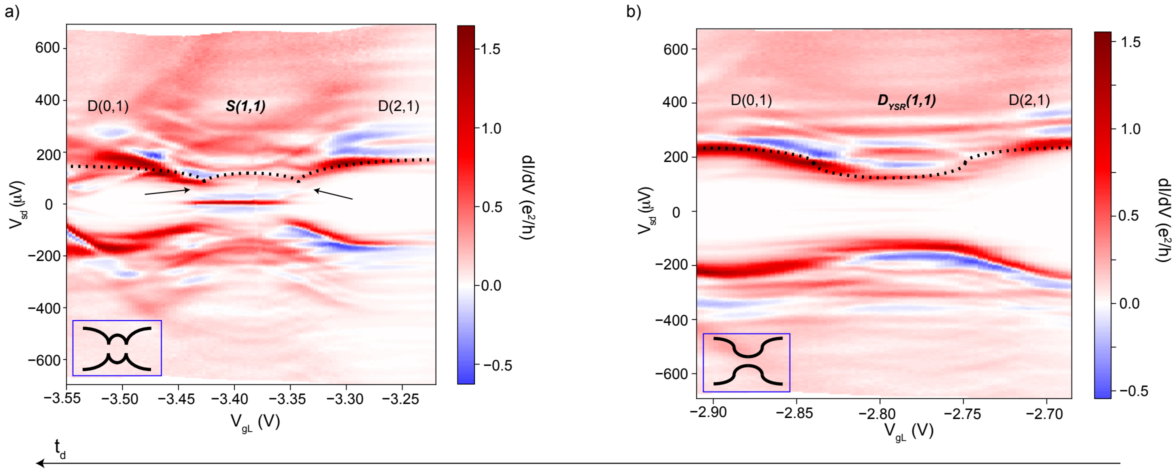

Figure 5.6: High bias spectroscopy $V_{\text{sd}} = \pm 600\,\mu V$ revealing the dependence of sub-gap states. Insets show the expected behaviour of sub-gap states. a) Conductance map in respect to the left plunger gate and bias voltage revealing bound state transitions. The device is tuned from the D(0,1) ground state to the S(1,1) and finally to the D(2,1). Dashed lines indicate the position of a bound state. The two arrows show the spots where the sub-gap states abruptly change direction, indicating a ground state transition. b) Conductance map for the screened triplet (1,1). It is observed that now that sub-gap states are smoothly anti-crossing, indicating no ground state transition in the (1,1) charge sector.

Screened regime for the right quantum dot

Increasing the coupling to the right lead t_R and decreasing the one to the left we achieved to tune the DQD to the screened regime but now for the right QD. Figure 5.7 shows a charge stability diagram of the screened right QD. The diagram is now rotated by 90°compared to the one of Fig. 5.5, as we now have the same ground states when sweeping the plunger gate controlling the right QD. No parity change lines are observed between the charge states (n,0),(n,1),(n,2) with n=0,1,2 indicating successful screening of the right QD.

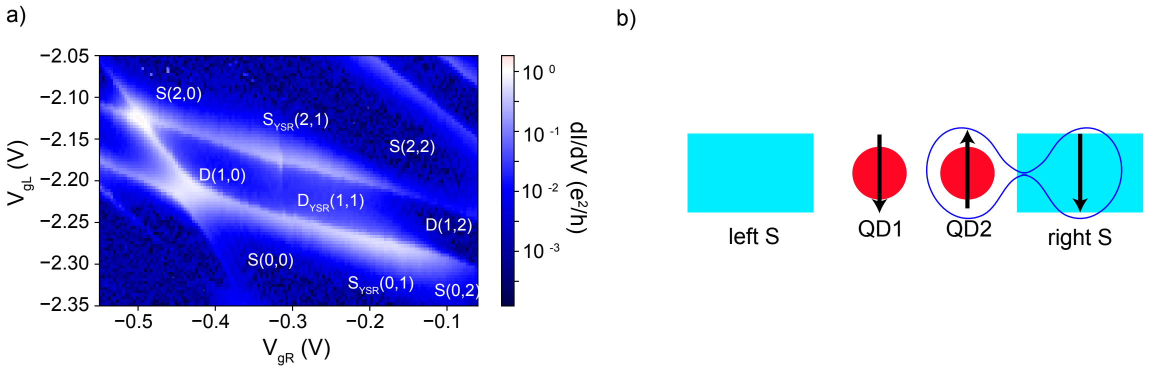

Figure 5.7: a) Charge stability diagram of our DQD. The coupling to the right lead t_R has now increased and there are no parity change lines between different QD occupations of the *right* QD. The (1,1) sector is also screened as the ground state between the (1,0),(1,1) and (1,2) charge states is maintained. Conductance walls are visible when adding an electron to the left QD proving that now the left QD is not screened. b) Schematic of screening of the right QD in the (1,1) sector. Initially the ground state was an exchange singlet. As the coupling to the right lead increased, the T_{11} state was screened into a D_{YSR}.

5.5 Simultaneous screening

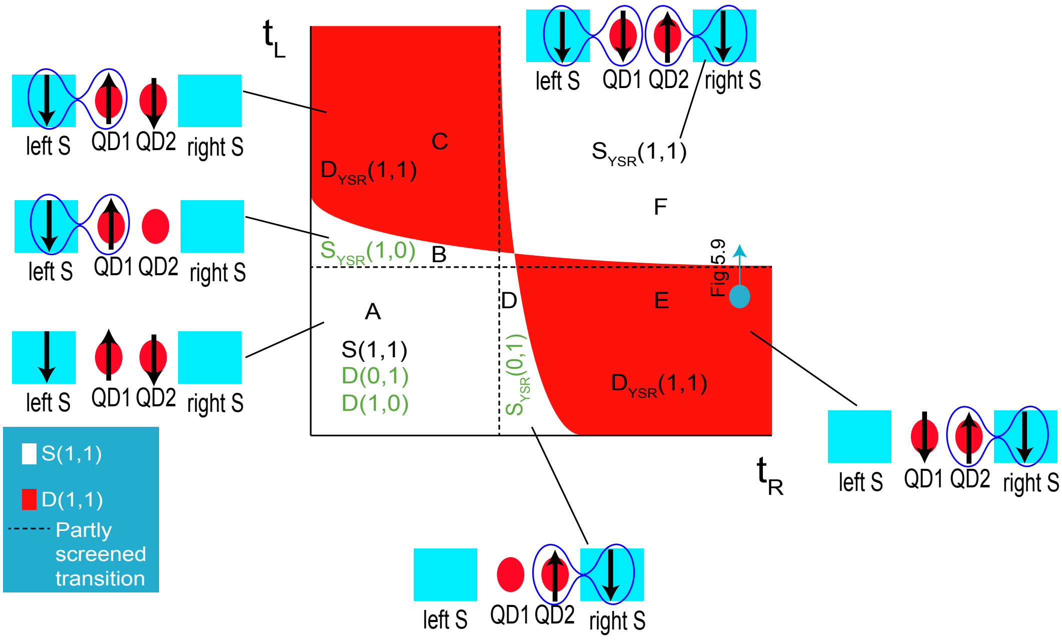

Figure 5.8: Schematic showing the dependence of the ground states of the sectors (1,1) (0,1) and (1,0) to the t_R and t_L. White colour implies that the (1,1) sector has a $|S\rangle$ ground state, while red a $|D_{YSR}\rangle$. Dashed lines show the point where the PS regime occurs. Each area of the diagram is described by a sketch showing changes in the (1,1) and the (1,0) charge sectors. On point A, the couplings are low and the DQD is in the known honeycomb regime. As t_L increases the (1,0) and (1,2) sectors suffer a ground state transition, noted with B and shown in Fig. 5.2c. In point C, for even larger couplings, where the exchange energy J is overcome, the $|T_{11}\rangle$ is screened to a $|D_{YSR}\rangle$. That process is shown in Fig. 5.5. Points D and E are symmetric to B and C but now t_R is increasing instead of t_L . To access the simultaneous screening regime, sufficient coupling to both leads is required in order to screen the (1,1) sector to a $|S_{YSR}\rangle$ where both electrons are screened by the S leads. That area is noted with F.

Demonstrating individual screening of each QD separately, we now want to proceed into the task of screening both QDs by increasing the tunnel coupling to both leads. Assume that the device is tuned in the screened regime for the right QD, as shown in Fig. 5.7. Charge sectors with odd occupation of the left QD have a $|D\rangle$ ground state, while the (1,1) has a $|D_{YSR}\rangle$. Following the intuition we cultivated from the previous measurements, by increasing the coupling to the left lead, screening of the (1,0),(1,1) and (1,2) charge states should be possible. Finally, with both QDs being screened, the ground state should be $|S\rangle$ for the all the nine charge states.

Figure 5.4 described the phase transitions for varying t_d and coupling to one S lead. We now extend that ground state diagram picking a fixed inter-dot coupling t_d and examining how the dependence to both t_L and t_R affects the transitions. That schematic is shown in Fig. 5.8 and describes the transitions between partly screened (areas B, D), screened (areas C, E), and simultaneous screened (area F) regimes. White colour corresponds to $|S\rangle$ ground state of the (1,1) sector while red to $|D\rangle$. The inter-dot coupling t_d determines the width of the PS regime, which is given by the distance of the dashed lines to the red area. For weaker t_d, we would expect the dashed lines to be pushed closer to the red regions. Note, that the distance between the partly screened (PS) and the screened (SC) regime is not stable. For larger t_R, we expect the transition to SC to be faster because an increase of fluctuations between the right QD and the right S lead could create a superposition of singlet and triplet ground state, making the process of screening the triplet easier.

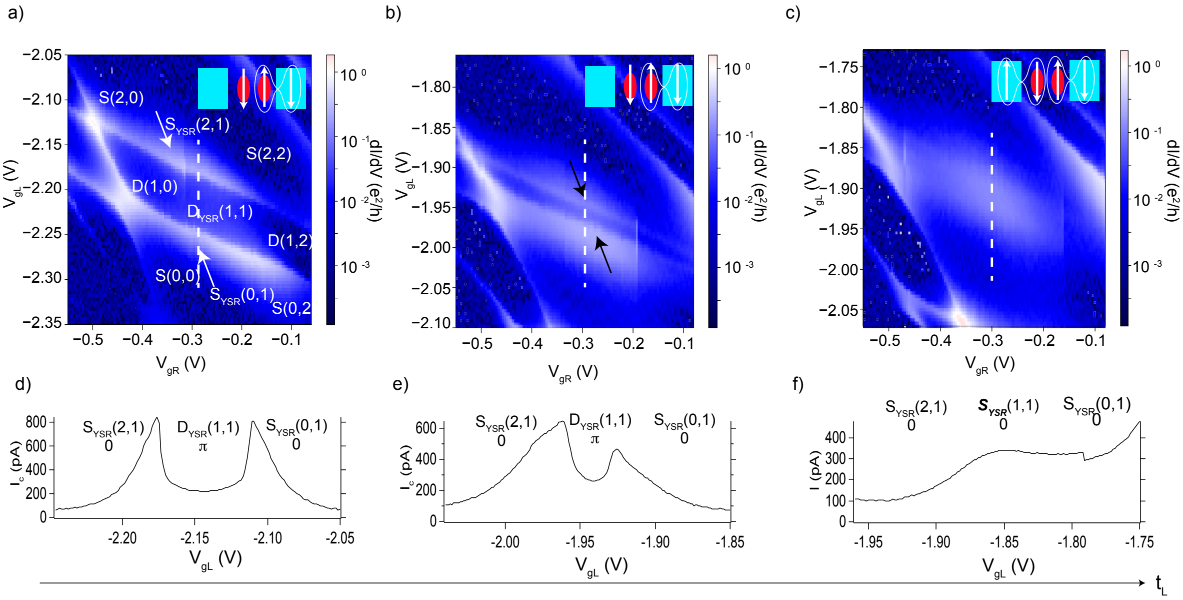

Figure 5.9: Charge stability diagrams for the intermediate steps between screened right QD to simultaneous screening of both QDs. The inset shows the (1,1) charge sector for each panel. a) The DQD is initially tuned in the screened regime for the right QD. b) Increasing t_L makes the parity change lines approach each other, shrinking the doublet ground state line. c) No sign of parity change line, as the two QDs are both screened by the superconductors. d-f) Equivalent I_c fits following the dashed line of panels a-c respectively. d) Extracted I_c has the expected behaviour, increasing smoothly in the singlet regions and abruptly decreasing when reaching a doublet. e) As the $|D\rangle$ region has shrank, the extracted I_c has also been affected. Note that the abrupt walls are starting to deteriorate. f) I_c is not showing any sharp changes or jumps. All three charge sectors have a singlet ground state, causing a $\pi \longrightarrow 0$ transition in the supercurrent.

In the following experiment, the device was initially tuned in the blue spot of the schematic. Figure 5.9 shows intermediate steps of tuning the backgate V_BG, indirectly increasing the coupling to the left lead. Initially, the DQD is tuned to the screened regime for the right QD, as there are no parity change lines when electrons are added to the same QD. For instance, tuning the device from the D(1,0) charge state to the D(1,1) and finally to the D(1,2) state does not produce any peak in conductance in the charge stability diagram. Tuning the V_BG, the barrier between the left lead and the nearest QD diminishes. It is visible that the parity change lines approach each other (see arrows), and finally in Figure 5.9c they have merged. The conductance is stronger in the middle of the plot while it seems to diminish smoothly on the edges. As there is no clear parity change line, but just a 'blob' of conductance, we claim that all nine charge sectors are in the $|S\rangle$ ground state.

Note that the adjacent (1,1) charge sectors have very different behaviour in terms of screening, as parity change lines are visible adjacent to the studied sector. The issue is that coupling is heterogeneous and strongly dependent to the plunger gates. Hence, by moving in the V_{gL}-V_{gR} space, we notice significant changes in coupling with the leads. Similar examples have been discussed in Chapter 4.

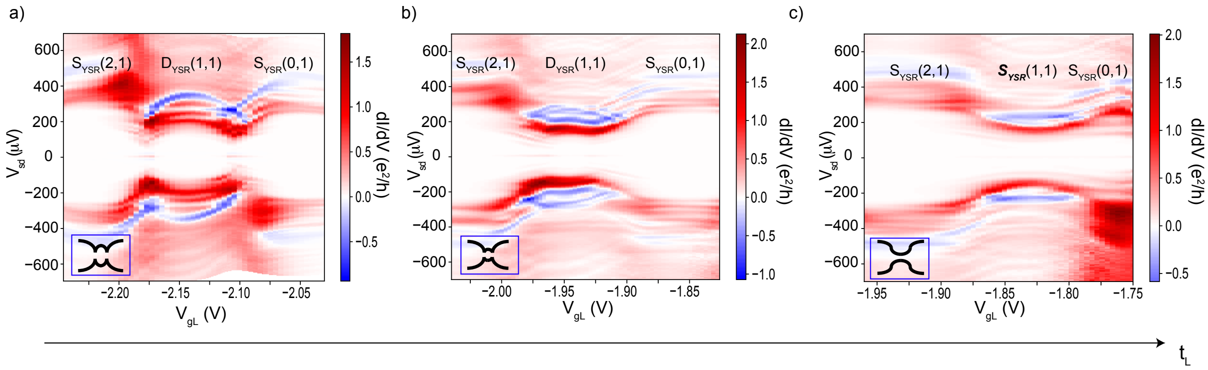

Figure 5.10: a) High bias spectroscopy revealing YSR sub-gap states dependence to increased coupling to the left lead. a) The DQD is transitting from the (2,1) to the (1,1) and finally to the (0,1) charge state. The right QD is screened, as a result the ground state transition are $|S_{\mathrm{YSR}}\rangle \rightarrow |D_{\mathrm{YSR}}\rangle \rightarrow |S_{\mathrm{YSR}}\rangle$. The bound state capture these transitions as they show an abrupt change when the QD enters the (1,1) sector and a second abrupt change at the (0,1) sector. These changes create a loop which is a signature of a bound state transition. b) Bias spectroscopy at higher coupling to the left lead. The loop is now not well defined, as the (1,1) sector is near its transition point. c) The (1,1) charge sector has transited to a $|S_{\mathrm{YSR}}\rangle$ indicating that both electrons are screened by the leads.

Figure 5.9d-f shows the extracted I_c that indicates ground state transitions. Panel d shows clear transitions between the charge sectors indicating $0 \rightarrow \pi \rightarrow 0$ transitions. Figure 5.9e shows a similar picture, but now the π region is significantly smaller, in accordance to panel b. Lastly, Fig. 5.9f shows the I_c having a smooth dependence to the plunger gate, implying that the ground state of the (1,1) sector has been changed to $|S_{\mathrm{YSR}}\rangle$. Note that the extracted critical current is lower when the ground state is singlet in the (1,1) sector. That is counter intuitive, since we have argued on this project that a $|S\rangle$ ground state provides higher I_c compared to a $|D\rangle$. However, in this case the tuning process was achieved by modifying the backgate. As a result, that affected the device globally, reducing the conductance of the system.

Higher bias measurements of the transitions to simultaneous screening are shown in Fig. 5.10, revealing the sub-gap states dependence. Initially, sub-gap states are forming a loop indicating ground state transitions $|S\rangle \longrightarrow |D\rangle \longrightarrow |S\rangle$. Figure 5.10b shows the intermediate step of tuning. The sub-gap states have cleared altered and the loop is suppressed. In Fig. 5.10c the sub-gap states at positive and negative bias are anti-crossing, indicating a ground state transition $|D_{\mathrm{YSR}}\rangle \longrightarrow |S_{\mathrm{YSR}}\rangle$ in the (1,1) sector.

5.6 Conclusions

The study of magnetic impurities in close proximity to superconductors has gained increased interest in the last years due to the presence of magnetic ions in high temperature superconductors. Hence, understanding how magnetic impurities interact with superconducting materials has inspired me to fabricate a double quantum dot (DQD) system in an InAs nanowire with epitaxial superconducting leads.

Through linear conductance measurements, I could map the transitions of the DQD for different QD occupation. By increasing the wave-function overlap of the superconductor to the QD, I could study how the unpaired spin of the QD altered the behaviour of the superconductor. Specifically, ground state transitions would occur for larger coupling, changing the ground state at odd total number of electrons to $|S\rangle$, which indicates successful screening of the magnetic impurity. Screening of the DQD for odd occupation of each dot was also demonstrated. Furthermore, I experimented with increased coupling to both superconducting contacts, realising simultaneous screening of the magnetic impurities, forming a DQD with all sectors being in the singlet ground state.

Finally, I sketched the quantum phase diagram of the screened phases of the system, which summarizes all these observations into a single diagram.

Chapter 6

Conclusions & Perspectives

6.1 Conclusions

This master thesis aids in the understanding of how two magnetic impurities interact with the Cooper pairs and quasiparticles of a superconductor. In my particular system, the two impurities were coupled to two superconductors, forming a novel type of Josephson junction. The culminating point of this thesis is the drafting of the quantum phase diagram of the system based on measurements of the supercurrent through the junction.

These measurements were made on a device based on a semiconductor nanowire with epitaxial superconducting leads. Using a number of bottom gates, I depleted sections along the nanowire and created tunnel barriers which defined a double quantum dot (DQD) in the semiconductor channel. Initially, I studied the system in the low coupling regime, in which the tunnel couplings are much weaker than the charging energies of the quantum dots (QDs) $\Gamma \ll U$. In that limit, I studied the honeycomb pattern of the DQD system. By defining a double quantum dot with large level spacing, I could label charge numbers (n,m) with n,m=0...2 referring to the QD occupation on the left and the right QD respectively. The QD occupation is directly related with the ground state of each charge sector. Hence, by measuring the zero bias peak of conductance which is related to supercurrent, I could map the ground state transitions $|S\rangle \longrightarrow |D\rangle$, which caused $0 \longrightarrow \pi$ transitions in the current-phase relation of the supercurrent $I_s = I_c \cdot sin(\phi + \phi_0)$. To verify that claim, I fitted my data with the extended RCSJ model with thermal fluctuations by Ivanchenko et al. [27]. Furthermore, I studied the hybridised bonding states in the vicinity of the triple points and analysed the behaviour of I_c against detuning. Fitted I_c curves show good agreement with a theoretical model of 4th order perturbation theory for the supercurrent, which was developed by our theory collaborators.

Completing the study of the honeycomb regime, I tuned the system to the intermediate coupling regime $\Gamma \sim U$ in order to study how the magnetic impurities interact with the superconducting leads. Specifically, I showed screening of $S = \frac{1}{2}$ states into a Yu-Shiba-Rusinov singlet ground state $|S_{YSR}\rangle$, by increasing the coupling to the closest superconductor. Additionally, I demonstrated individual screening of the left and the right QD, including screening of the spin of one dot when there is a spin present in the other. The latter involves screening of the excited $|T_{11}\rangle$ state of the S(1,1) charge sector to a $|D_{YSR}\rangle$. Apart from charge stability diagrams hinting the screening effects, I support the claim of coupling-induced ground-state transitions by studying the gate-modulation of I_c. A novelty of this study is the demonstration of the intermediate steps in the DQD charge stability diagram, starting from the honeycomb and reaching the screened regimes. These steps support the argument of YSR screening as the same set of nine charge sector is slowly transiting to the partially screened, and then to the screened regime. Moreover, we demonstrated simultaneous screening of both magnetic impurities in the (1,1) sector by increasing the couplings to both leads. That led to a situation where all the nine charge sectors of the DQD had a $|S\rangle$ ground state, resulting in the effective disappearance of the charge stability diagram.

Furthermore during this project I studied and was part of two more experiments that I have not included in the thesis. I studied the multi-level regime of the S-DQD-S system, in which the level spacing ΔE is negligible for both QDs . This led to the interesting result of having *both* 0 and π phases of the supercurrent $I_s = I_c \cdot sin(\phi + \phi_0)$ in the *same* charge sector. Additionally, I studied the relaxation time of quasiparticles in Yu-Shiba Rusinov sub-gap states in a N-QD-S system. We found out that the coupling to the superconductor Γ_s and the coupling to the normal metal Γ_N have an influence to the relaxation rate of the quasiparticle. We also studied how the relaxation rate depends on T.

6.2 Perspectives

I outline below two perspectives of my work.

The level spacing of the QDs defined in a nanowire scales inversely with its diameter. The nanowires I used in this project were 100 nm in diameter, leading to difficulty in defining a DQD with large level spacing. A period of three months of tuning of the device was needed to obtain a sufficient confinement of the dots. To overcome that struggle in future devices thinner nanowires are desired. First of all, thinner nanowires would create better confinement of electrons and it would be easier to observe a shell filling pattern in the DQD. Moreover the interface of semiconductor-superconductor film would decrease. Hence, we would observe less bound states as there is a speculation that bound states are created by Andreev reflection on the interface of the semiconductor and the superconducting film. However, a drawback of using such nanowires is that they might be more fragile to electrostatic discharge during fabrication process, slightly harder to manipulate with a micromanipulator. Lastly, they would be more sensitive to impurities in the wire and surface charges, as the surface to volume ratio is increased.

Furthermore, in such systems it is also interesting to study how an external magnetic field would induce ground state transitions in the charge sectors. One of the main advantages of the epitaxially grown aluminium is that its critical magnetic field is much higher compared to evaporated aluminium, mainly because it is much thinner. Exploiting this feature, it would be interesting to fabricate a superconductor - double quantum dot - normal metal (S-DQD-N) device with the aim of studying ground state transitions in the S(1,1) charge sector. Specifically, as the magnetic field increases the triplet degeneracy is lifted, and at some point the $|T_{-}\rangle$ excited state crosses the singlet state and becomes the ground state. If the g-factor of the nanowire is high enough, we might be able to observe an interplay of both YSR screening and magnetic field induced transitions in the S(1,1) sector. That can aid in further understanding how magnetic impurities behave in close proximity to superconductors. Such study could also be done in Josephson junction geometry as the one presented in this thesis.

Appendix A

Additional measurements

A.1 Honeycomb regime

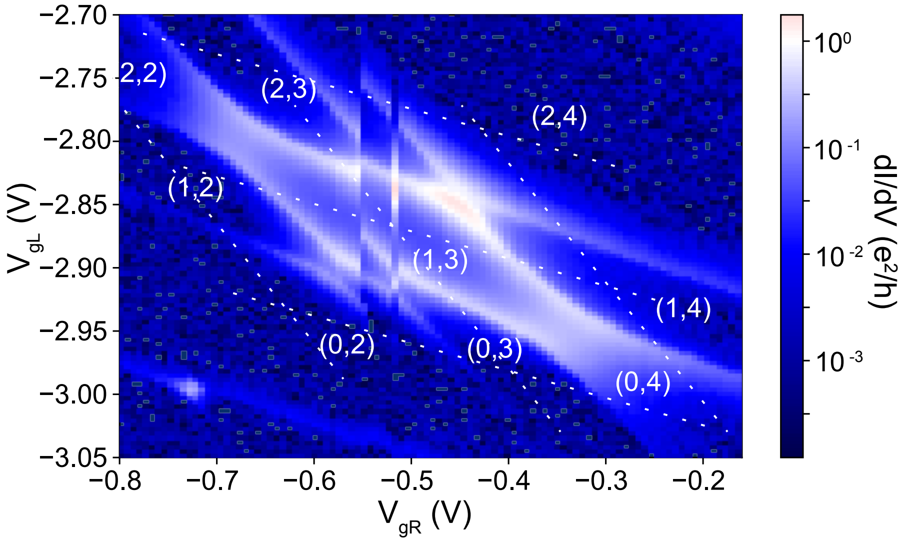

Figure A.1: Charge stability diagram of the (1,3) sector with its adjacent Coulomb diamonds. It is clear that the honeycomb looks qualitatively similar to the previous one depicted in Fig. 4.8. A few gate switches are interrupting the plot, however it is obvious that there is shell filling in this DQD tuning. Note that this measurement was taken at different tunnel gate values compared to the previous (1,1) charge sector. The dashed lines indicate the direction of the supercurrent cuts.

This section covers supercurrent measurements taken in an adjacent (1,1) charge sector of the one studied, with the aim to reveal the homogeneity of the system throughout the gate-space position. Specifically, it is essential to show that the supercurrent dependence to the QD occupancy is a universal feature, and not just an artefact that was observed on a specific gate tuning of the device. Fig. A.1 shows the charge stability diagram at zero bias for the (1,3) charge sector. Qualitatively, the DQD looks similar, apart from the few switches that are visible in the center of the plot. However, we need to view the bias spectroscopy plots to determine if the supercurrent shows the same behaviour in the ground state transitions. Figure A.2 shows the six plots indicated with dashed lines in Fig. A.1. Interestingly, the supercurrent is again slowly increasing followed by a sudden drop when the DQD transits from a $|S\rangle$ to a $|D\rangle$ region. Even though that there are a few switches in the measurements, it is possible to see that the system behaves with the same pattern. The zero bias conductance follows a slow increase when going towards a parity change line when on the $|S\rangle$ ground state, and it drops abruptly when it 'enters' a $|D\rangle$. In addition, the sub gap states that are visible create loops when there is such a transition, similar to those shown in the initial set of measurements in Fig. 4.9.

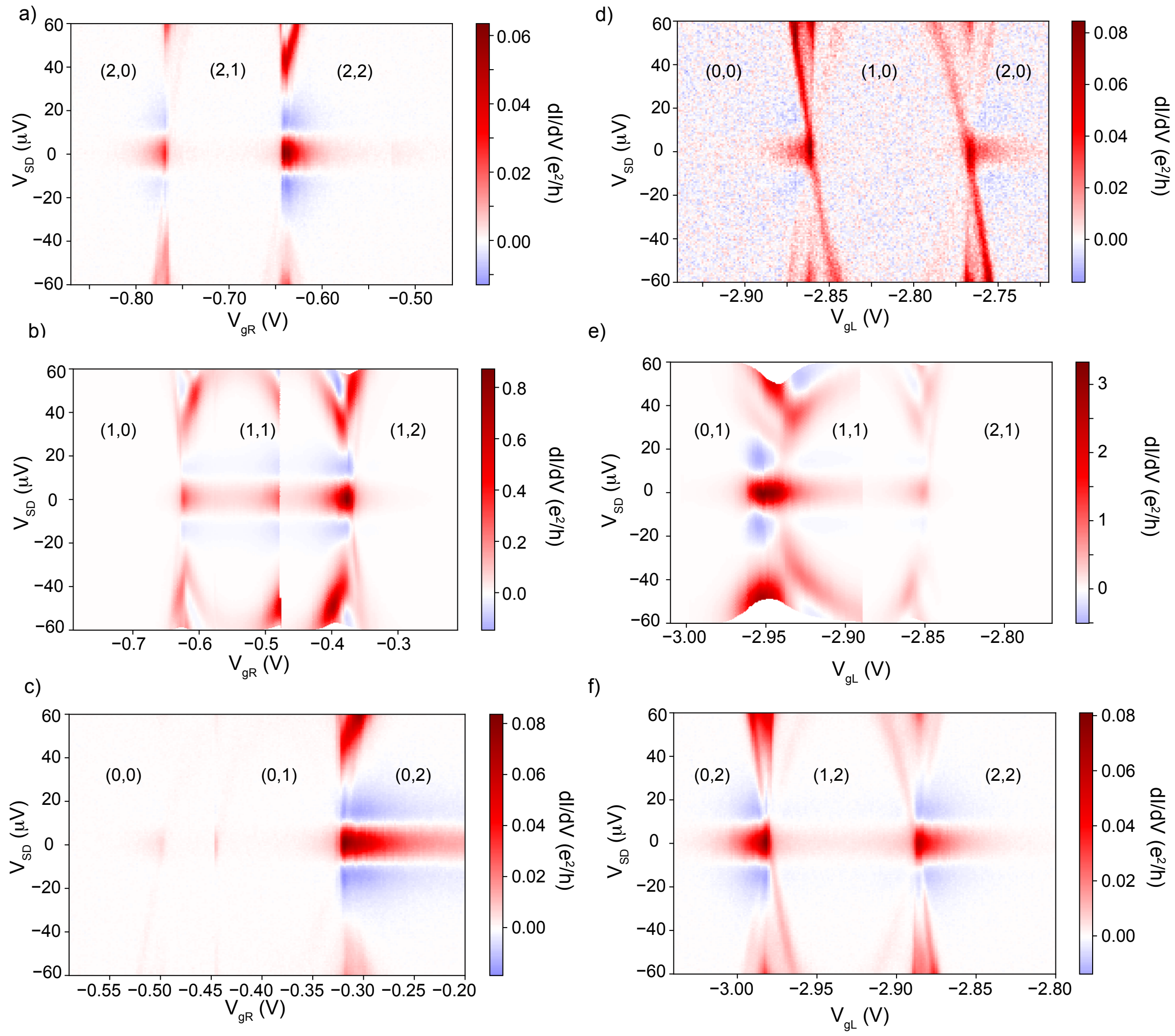

Figure A.2: Bias spectroscopy of supercurrent as a dot is swept through different occupation numbers with the second dot having fixed occupancy. Note that for the sake of comparison between the two charge states, the charge numbers of the (1,3) sector are transformed to show only the occupation of the highest orbital i.e. (1,3) → (1,1) and (2,4) → (2,2). a) Zero bias peak slowly increases in magnitude as the system is driven to the degeneracy point and abruptly drops when a phase transition occurs from $|S\rangle$ to $|D\rangle$. b) The system is now driven through the (1,1) sector which has a $|S\rangle$ ground state. The zero bias peak is slow increasing when the system moves closer to the degeneracy point with a $|D\rangle$ region, and then abruptly drops. c) Now the DQD is passing from the (0,0) to the (0,1) and finally to the (0,2) charge sector. Similar behaviour to a) can be seen. d-f) Analogous measurements with the left column with the difference that the right QD is now kept at fix occupation.

Molecular regime

Figure A.3 shows the zero-bias peak measurements of the detuning I_c fits shown in Chapter 4. The zero-bias peak does not show any abrupt jump or drop in conductance, hinting that the ground state is maintained. Nonetheless, the magnitude of the peak increases on the molecular regime, as shown by the I_c fits.

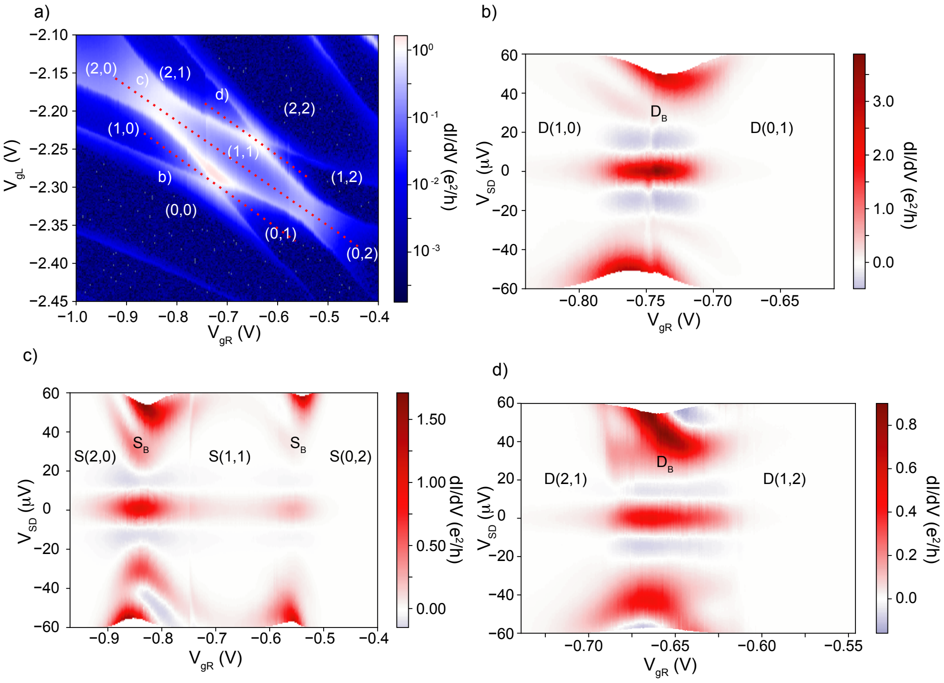

Figure A.3: a) Zero bias conductance map of the studied DQD. Dashed lines indicate the direction of the detuning cuts shown in the following panels. b) Detuning measurement through the doublet bonding orbital between the (1,0) and the (0,1) charge states. It is clear that although the ground state is unaffected on this cut, the supercurrent is enhanced in the molecular region. That is due to the fact that when the two levels of the QDs are aligned, supercurrent is enhanced. c) Detuning cut through the (1,1) sector. Supercurrent shows clears sign of enhancement in the $|S_B\rangle$ regions. One of the two show larger conductance owing to the different coupling caused by V_{gL}. d) Analogous cut with panel b through the (2,1) and (1,2) Coulomb diamonds.

A.2 Screening of the triplet state by left S

In this section I show the supplementary bias spectroscopy measurements for the transition from the partly screened to the screening of the triplet (1,1) state. Figure A.4 shows the respective zero-bias measurements of Fig. 5.5.

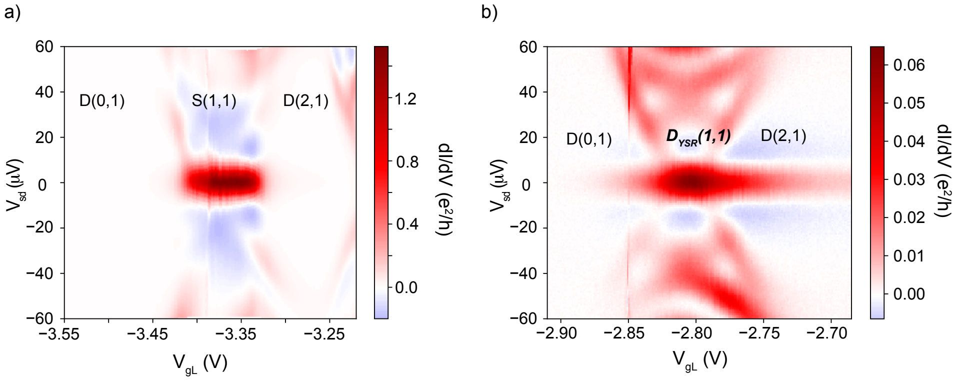

Figure A.4: a-c) Bias spectroscopy of the zero bias peak versus plunger gate for the dashed white lines shown in Fig. 5.5. The line-cut passes through the (2,1),(1,1) and (0,1) charge states, where the electron of the right QD is already screened. a) We observe a well defined doublet region in the (1,1) sector, which is breached by two zero-bias 'walls', indicating $|D\rangle \rightarrow |S\rangle$ transitions. b) At larger coupling to the left lead, the $|D\rangle$ region is significantly suppressed. Discontinuities in zero bias conductance are still present. c) Zero bias peak is now homogeneous throughout the gate range. That implies a ground state transition of the (1,1) sector.

A.3 Simultaneous screening

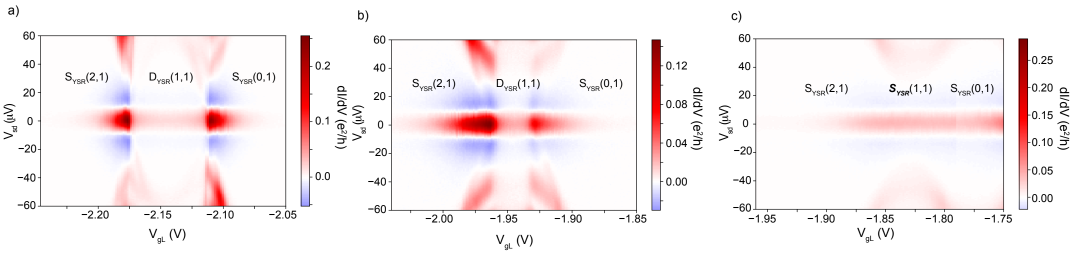

Figure A.5: Bias spectroscopy through the (0,1)-(1,1)-(2,1) charge states for the partly screened and screening of the triplet (1,1) state. a) Bias spectroscopy revealing a zero bias peak related to supercurrent for the partly screened regime. As expected, there is a clear abrupt 'jump' in conductance when the system transits from a doublet to a singlet ground state. b) At lower inter-dot coupling, the same bias spectroscopy reveals a continuous zero bias peak, implying that there is no ground state transition. The ground state is maintained as we have a $|S_{11}\rangle \rightarrow |D_{YSR,11}\rangle$ transition.

This section includes the zero-bias measurements for the device transiting to the simultaneous screening regime, as shown in Fig. 5.9.

Appendix B

Fabrication recipe

This section contains the full and detailed recipe that was used on the superconductor - double quantum dot - superconductor (S-DQD-S) device. All the steps that are described in the fabrication chapter are noted here in detail. The recipe had undergone several changes, until it was optimised for device A2S3 which is noted in the Device list section of the appendix.

B.1 Bonding pads

The processing began with a 2 inch Si/SiO_2 wafer with a 300 nm oxide height. After the wafer was cut at the desired dimensions, cleaning followed which is a very important step that ensures that there are no debris from cleaving in the substrate, as well as any other dirt that can harm the fabricated devices.

Cleaning:

- Rinsing in H_2O, isopropanol (IPA) and acetone
- Sonicating in acetone for 2 min. at frequency 80 kHz, power 100.
- Rinsing in H_2O, isopropanol (IPA) and acetone, then blow dry with N_2.
- O_2 plasma ashing for 2 min.

Spin coating of resist for bonding pads:

- Baking chip at 185 °C for 4 min.
- Spin coating LOR3B resist at 4000 rpm for 45 s
- Baking chip at 185 °C for 4 min.
- Spin coating AZ1505 resist at 4000 rpm for 45 s
- Baking chip at 115 °C for 2 min.

The LOR3B resist (lift-off resist) is used in order to create an undercut in the developing process of the resists, thus leading to smooth lift-off. For the bonding pads, we used photo-lithography since the features are large and electron beam lithography is not necessary on this step. For the photo-lithography system I used, the exposure time was 20 ms and the defocus -2.

Develop:

- Submersing the sample in MF321 for 30 s
- Submersing in Millipore (MQ) water for 30 s
- Drying with N_2
- O_2 plasma ashing for 2 min.

Metal evaporation:

To evaporate any sort of metal and make our devices we are using an AJA evaporation system. We rotated and tilted the chip 15 °to have smooth edges on the outer leads that ensure easy contacting.

- Deposition of 5 nm Ti.
- Deposition of 100 nm Au.

Lift-off:

- Submersing the sample in N-Methyl-2-pyrrolidone (NMP) at 85 °C.
- Sonication at 37 kHz 100 power for 1 min.
- 60 min. in NMP bath at 85 °C
- Flushing the chip with a pipette to accelerate lift-off
- rinsing in IPA
- Drying with N_2

B.2 Alignment marks

This section will cover the fabrication recipe for the alignment marks designed on the substrate. This step is crucial all the subsequent steps will use these marks are reference positions to accurately transfer the designed pattern in the software to the actual sample.

Resist spin coating:

- Rinsing in IPA and acetone
- O_2 plasma ashing for 2 min.
- Baking chip at 185 °C for 3 min.
- Spin coating EL9 resist at 4000 rpm for 45 s
- Baking chip at 185 °C for 3 min.
- Spin coating CSAR4 resist at 4000 rpm for 45 s
- Baking chip at 185 °C for 3 min.

Electron beam lithography exposure:

- Area dose of 400 $\mu C/cm^2$
- 20000 dots per write field and 150 μm write field size
- 500 pA current

Develop:

- Submersing the sample in O-xylene for 30 sec.
- Submersing in MIBK:IPA 1:3 developer for 40 sec.
- Submersing in IPA for 30 sec.
- O_2 plasma ashing for 1 min.

Metal evaporation:

- Rotating and tilting 15 °during evaporation
- Deposition of 5 nm Ti.
- Deposition of 100 nm Au. This amount of metal is needed for successful automatic alignment in EBL.

Lift-off:

- Submersing the sample in N-Methyl-2-pyrrolidone (NMP) at 85 °C.
- Sonication at 37 kHz 100 power for 1 min.
- 60 min. in NMP bath at 85 °C
- Flushing the chip with a pipette to accelerate lift-off
- rinsing in IPA
- Drying with N_2

B.3 Bottom gates

The next fabrication step was to define the bottom gates that will form the tunnel barriers and the plungers for our devices.

Resist spin coating:

- Rinsing in IPA and acetone
- O_2 plasma ashing for 2 min.
- Baking chip at 185 °C for 4 min.
- Spin coating A2 resist at 4000 rpm for 45 s
- Baking chip at 185 °C for 4 min.

EBL exposure:

- Area dose of 1600 $\mu C/cm^2$
- 60000 dots per write field and 150 μm write field size
- 500 pA current

Develop:

- 2 min. 30 sec. at IPA:H_2O mixture with ratio 7:3 at -5 °C .
- Drying with N_2 for 4 min. to thermalize the chip
- O_2 plasma ashing for 30 sec.

Metal evaporation:

- Deposition of 5 nm Ti.
- Deposition of 16 nm Au.

Lift-off:

- Submersing the sample in N-Methyl-2-pyrrolidone (NMP) at 85 °C.
- Sonication at 37 kHz 100 power for 1 min.
- 60 min. in NMP bath at 85 °C
- Flushing the chip with a pipette to accelerate lift-off
- rinsing in IPA
- Drying with N_2

B.4 Dielectric

To isolate the bottom gates with the nanowires that will be deposited on the substrates, 2 layers of HfO_2 were deposited with 7 nm height each. We used an atomic layer deposition (ALD) system for this step.

Resist spin coating:

- O_2 plasma ashing for 4 min.
- Baking chip at 185 °C for 4 min.
- Spin coating LOR3B resist at 4000 rpm for 45 s
- Baking chip at 185 °C for 4 min.
- Spin coating AZ1505 resist at 4000 rpm for 45 s
- Baking chip at 115 °C for 2 min.

The oxide patterns were exposed using photolithography, with the same parameters noted above.

Develop:

- Submersing the sample in MF321 for 30 s.
- Submersing in Millipore (MQ) water for 60 s
- Drying with N_2

ALD:

- O_2 plasma ashing for 2 min.
- 7 nm HfO_2

Lift-off:

- Scratch all four corners of the chip
- Submersing the sample in N-Methyl-2-pyrrolidone (NMP) at 85 °C.
- Sonication at 37 kHz 100 power for 1 min.
- 60 min. in NMP bath at 85 °C
- In a new NMP beaker, sonication at 37 kHz 100 power for 1 min.
- Flushing the chip with a pipette to accelerate lift-off
- rinsing in IPA
- Drying with N_2

B.5 Aluminum etching

After the substrate is prepared, nanowire deposition perpendicular to the bottom gates follows. A micromanipulator was used to transfer and deposit the nanowires. The first step of nanowire processing is to selectively etch a part of the Al shell. To achieve that, we used standard EBL processing.

Resist spin coating:

- O_2 plasma ashing for 2 min.
- Spin coating EL9 resist at 4000 rpm for 45 s with the low acceleration program
- Baking chip at 185 °C for 2 min.

EBL exposure:

- Area dose of 400 $\mu C/cm^2$
- 60000 dots per write field and 300 μm write field size
- 500 pA current

Develop:

- Submersing the sample in MIBK:IPA 1:3 developer for 40 sec.
- Drying with N_2
- Baking chip at 115 °C for 1 min.

Al etching:

We set the bath at 55 °C and we put inside a beaker of transene D and another one with MQ water of the same volume. We sporadically measure the temperature of the MQ beaker. When it reaches 50 °C then:

- Submersing the sample the transene D for 8 sec.
- Rinsing in the warm MQ beaker for 30 sec.
- Rinsing in room temperature MQ beaker for 30 sec.
- Drying with N_2

After the process is over, we remove the excess resist by submersing the sample in a beaker of NMP at 55 °C for 7 min.

Metal contacts: The final step of fabrication was to evaporate the leads of the devices.

Resist spin coating:

- O_2 plasma ashing for 1 min.
- Spin coating PMMA 50K resist at 4000 rpm for 45 s with the low acceleration program
- Baking chip at 115 °C for 2 min.
- Spin coating PMMA 50K resist at 4000 rpm for 45 s with the low acceleration program
- Baking chip at 115 °C for 2 min.

EBL exposure:

- Area dose of 850 $\mu C/cm^2$
- 60000 dots per write field and 300 μm write field size
- 500 pA current

Develop:

- Submersing the sample in MIBK:IPA 1:3 developer for 75 sec.
- Rinsing in IPA for 30 sec.
- Drying with N_2
- O_2 plasma ashing for 2 min.

Metal evaporation:

- RF milling to remove the native oxide of the nanowires. 15 W, 18 mTorr, for 8 min.
- Deposition of 5 nm Ti.
- Deposition of 200 nm Au.

Lift-off:

- Submersing the sample in N-Methyl-2-pyrrolidone (NMP) at 85 °C for 60 min.
- Flushing the chip with a pipette to accelerate lift-off
- rinsing in IPA
- Drying with N_2

Appendix C

Device list

In this section I have added a table including all the devices I fabricated during my thesis. All the devices starting with A2 or A5 have predesigned bottom gates with a pitch of 40 nm. Above them, there is a double 7 nm HfO_2 layer which insulates the bottom gates from the nanowire, providing good gating effect.

The main challenges that we had to overcome during fabrication was the over-etching problem that wouldn't allow us to study superconducting phenomena and also the issue with bad contact of the semiconducting nanowires. We also experienced several problems with devices blowing up after the final step of bonding and loading. The solutions to these problems are covered in the fabrication chapter of the thesis.

Chip name	Device description
AV1_2	InAs nanowires with 7 nm 3 facet epitaxial Aluminium (Al). 2 terminal (2T) devices with evaporated 5 nm Ti/150 nm Al. 1 out of 8 devices conducted. Supercurrent measurements and magnetic field dependance of the superconducting properties.
A2S8	InAs nanowires with 7 nm 3 facet epitaxial Al. 5 nm Ti / 160 nm Au evaporated contacts. 4 devices on the chip on which all of them blew up due sudden voltage change. On the SEM it was seen that large parts of the evaporated metal had peeled off, probably due to bad evaporation caused by resist residues.
A5S2	InAs nanowires with 7 nm 3 facet epi-Al. 5 nm Ti/ 160 nm Au evaporated. One device conducted but showed no superconducting features. The other 3 did not conduct, due to bad contact.
A5S7	Pristine InAs nanowires with evaporated 5 nm Ti / 150 nm Al contacts. Static electricity/sudden voltage change issues persisting. Poor gating effect due to overexposure. One parallel wire configuration attempt.
A5S3	InAs nanowires with 7 nm 3 facet epi-Al. 5 nm Ti/ 170 nm Au. Superconducting features were observed but the devices were unstable as well as the gate dependence of the nanowires weak.
A2S4	InAs nanowires with 7 nm 3 facet epi-Al. 5nm Ti / 170 nm Au. Bad contact between the evaporated metal and the nanowires.
A5S8	InAs nanowires. Al/V/Al metal evaporation. Lift-off problems caused most of the devices to have shorted source and drain. This happened because the vanadium was evaporated at high rate, 8.5 A/s, which made the resist near the developed area very warm, resulting into resist crystallization.
A5S5	InAs nanowires with 7 nm 3 facet epi-Al. 5 nm Ti / 200 nm Au evaporated to reassure that there is contact with the nanowire. On one device we defined a double quantum dot and we measured sub gap states. No presence of supercurrent or hard superconducting gap.
A5S4	InAs nanowires with 7 nm 3 facet epi-Al. 5 nm Ti/ 185 Au evaporated. Devices blew up possibly from not grounding ourselves properly during bonding and loading.
A2S3	InAs nanowires with 7 nm 3 facet epi-Al. 5 nm Ti/ 200 nm Au evaporated to ensure contact between the nanowire and the metal. One of the samples showed hard superconducting gap and we studied the honeycomb and the screened regimes on this device.
A2S7	InAs nanowires with 7 nm 3 facet epi-Al. This geometry differs from the previous in the sense that the aluminum is fully etched on the wire apart from a small segment of 170 nm in the center. 6 devices were fabricated, which were quite hard to pinch off.
A2S2	InAs nanowires with 7 nm 3 facet epi-Al. In this geometry there is a superconducting island in the center of the nanowire with a length of 180 nm. 6 bottomgates were used on each device as well as 2 side gates to have better control of the island.
A5S6	InAs nanowires with 7 nm 3 facet epi-Al. In this chip, 7 devices were fabricated. Half of the nanowire was wet etched in order to remove the Aluminum part. These devices used a combination of side and bottom gates and we formed a QD in the semiconducting channel.

References

[1] L Yu. Bound state in superconductors with paramagnetic impurities. Acta Phys. Sin, 21(1), 1965.

[2] Hiroyuki Shiba. Classical spins in superconductors. Progress of theoretical Physics, 40(3):435–451, 1968.

[3] AI Rusinov. Superconductivity near a paramagnetic impurity. Soviet Journal of Experimental and Theoretical Physics Letters, 9:85, 1969.

[4] Anders Jellinggaard, Kasper Grove-Rasmussen, Morten Hannibal Madsen, and Jesper Nygård. Tuning yu-shiba-rusinov states in a quantum dot. Physical Review B, 94(6):064520, 2016.

[5] Eduardo JH Lee, Xiaocheng Jiang, Manuel Houzet, Ramón Aguado, Charles M Lieber, and Silvano De Franceschi. Spin-resolved andreev levels and parity crossings in hybrid superconductor-semiconductor nanostructures. Nature nanotechnology, 9(1):79–84, 2014.

[6] Yoichi Kamihara, Hidenori Hiramatsu, Masahiro Hirano, Ryuto Kawamura, Hiroshi Yanagi, Toshio Kamiya, and Hideo Hosono. Iron-based layered superconductor: Laofep. Journal of the American Chemical Society, 128(31):10012–10013, 2006.

[7] Jorden a van Dam, Yuli V Nazarov, Erik P a M Bakkers, Silvano De Franceschi, and Leo P Kouwenhoven. Supercurrent reversal in quantum dots. Nature, 442(7103):667–670, 2006.

[8] John Bardeen, Leon N Cooper, and John Robert Schrieffer. Theory of superconductivity. Physical Review, 108(5):1175, 1957.

[9] BB Goodman. Type ii superconductors. Reports on progress in physics, 29(2):445, 1966.

[10] JE Hirsch. The origin of the meissner effect in new and old superconductors. Physica Scripta, 85(3):035704, 2012.

[11] P Krogstrup, NLB Ziino, W Chang, SM Albrecht, MH Madsen, Erik Johnson, Jesper Nygård, CM Marcus, and TS Jespersen. Epitaxy of semiconductor–superconductor nanowires. Nature materials, 14(4):400–406, 2015.

[12] W Chang, SM Albrecht, TS Jespersen, Ferdinand Kuemmeth, Peter Krogstrup, J Nygård, and CM Marcus. Hard gap in epitaxial semiconductor–superconductor nanowires. Nature nanotechnology, 10(3):232–236, 2015.

[13] MT Deng, S Vaitiekėnas, EB Hansen, J Danon, M Leijnse, K Flensberg, J Nygård, P Krogstrup, and CM Marcus. Majorana bound state in a coupled quantum-dot hybrid-nanowire system. Science, 354(6319):1557–1562, 2016.

[14] K Grove-Rasmussen, G Steffensen, A Jellinggaard, MH Madsen, R Žitko, J Paaske, and J Nygård. Yu–shiba–rusinov screening of spins in double quantum dots. Nature communications, 9(1):2376, 2018.

[15] Dawon Kahng. Silicon-silicon dioxide field induced surface devices. In the Solid State Device Research Conf., Pittsburgh, PA. June 1960, 1960.

[16] Ronald Hanson, Leo P Kouwenhoven, Jason R Petta, Seigo Tarucha, and Lieven MK Vandersypen. Spins in few-electron quantum dots. Reviews of Modern Physics, 79(4):1217, 2007.

[17] Elias Burstein and Stig Lundqvist. Tunneling phenomena in solids. Springer, 1969.

[18] D Goldhaber-Gordon, Hadas Shtrikman, D Mahalu, David Abusch-magder, U Meirav, and M A Kastner. Kondo effect in a single-electron transistor. Nature, 391(January):1996–1999, 1998.

[19] Leo Kouwenhoven and Leonid Glazman. Revival of the kondo effect. Physics world, 14(1):33, 2001.

[20] Wilfred G Van der Wiel, Silvano De Franceschi, Jeroen M Elzerman, Toshimasa Fujisawa, Seigo Tarucha, and Leo P Kouwenhoven. Electron transport through double quantum dots. Reviews of Modern Physics, 75(1):1, 2002.

[21] SJ Chorley, MR Galpin, FW Jayatilaka, CG Smith, DE Logan, and MR Buitelaar. Tunable kondo physics in a carbon nanotube double quantum dot. Physical review letters, 109(15):156804, 2012.

[22] S Alexander. S. alexander and pw anderson, phys. rev. 133, a1594 (1964). Phys. Rev., 133:A1594, 1964.

[23] Silvano De Franceschi, Leo Kouwenhoven, Christian Schönenberger, and Wolfgang Wernsdorfer. Hybrid superconductor-quantum dot devices. Nature Nanotechnology, 5(10):703–711, 2010.

[24] V. Mourik, K. Zuo, S. M. Frolov, S. R. Plissard, E. P. a. M. Bakkers, and L. P. Kouwenhoven. Signatures of Majorana Fermions in. Science, 336(6084):1003, 2012.

[25] Brian David Josephson. Possible new effects in superconductive tunnelling. Physics letters, 1(7):251–253, 1962.

[26] Michael Tinkham. Introduction to superconductivity. Courier Corporation, 1996.

[27] Yu M Ivanchenko and L A Zil 'berman. the Josephson Effect in Small Tunnel Contacts. Soviet Physics Jetp, 28(6):1272–1276, 1969.

[28] Vinay Ambegaokar and B. I. Halperin. Voltage due to thermal noise in the dc josephson effect. Phys. Rev. Lett., 23:274–274, Aug 1969.

[29] H. Ingerslev Jörgensen, T. Novotný, K. Grove-Rasmussen, K. Flensberg, and P. E. Lindelof. Critical current 0-π transition in designed josephson quantum dot junctions. Nano Letters, 7(8):2441–2445, 2007.

[30] Rudolf Gross, Achim Marx, and Frank Deppe. Applied superconductivity: Josephson effect and superconducting electronics. De Gruyter, 2015.

[31] R Delagrange, R Weil, A Kasumov, M Ferrier, H Bouchiat, and R Deblock. 0-π quantum transition in a carbon nanotube josephson junction: universal phase dependence and orbital degeneracy. Physical Review B, 93(19):195437, 2016.

[32] Benjamin W Heinrich, Jose I Pascual, and Katharina J Franke. Single magnetic adsorbates on s-wave superconductors. Progress In Surface Science, 93(1):1–19, 2018.

[33] JD Pillet, CHL Quay, P Morfin, C Bena, A Levy Yeyati, and P Joyez. Andreev bound states in supercurrent-carrying carbon nanotubes revealed. Nature Physics, 6(12):965–969, 2010.

[34] http://www.oxford-instruments.cn/oxfordinstruments/media/nanoscience/priciples-of-dilution-refrigeration.pdf.

[35] https://www.omega.co.uk/temperature/z/overviewieee.html.

[36] Pablo Jarillo-Herrero, Jorden A Van Dam, and Leo P Kouwenhoven. Quantum supercurrent transistors in carbon nanotubes. Nature, 439(7079):953–956, 2006.

[37] Zhaoen Su, Alexandre B Tacla, Moïra Hocevar, Diana Car, Sébastien R Plissard, Erik PAM Bakkers, Andrew J Daley, David Pekker, and Sergey M Frolov. Andreev molecules in semiconductor nanowire double quantum dots. Nature communications, 8(1):585, 2017.

[38] H Ingerslev Jørgensen, Kasper Grove-Rasmussen, K-Y Wang, AM Blackburn, Karsten Flensberg, Poul Erik Lindelof, and DA Williams. Singlet–triplet physics and shell filling in carbon nanotube double quantum dots. Nature Physics, 4(7):536, 2008.

[39] JC Saldaña, R Žitko, JP Cleuziou, EJH Lee, V Zannier, D Ercolani, L Sorba, R Aguado, and S De Franceschi. Supercurrent through a spin-split quasi-ballistic point contact in an inas nanowire. arXiv preprint arXiv:1801.01855, 2018.

[40] Z Su, A Zarassi, J-F Hsu, P San-Jose, E Prada, R Aguado, EJH Lee, S Gazibegovic, R Veld, D Car, et al. Mirage andreev spectra generated by mesoscopic leads in nanowire quantum dots. arXiv preprint arXiv:1805.04289, 2018.

[41] Philip Warren Anderson. Localized magnetic states in metals. Physical Review, 124(1):41, 1961.

[42] Koji Satori, Hiroyuki Shiba, Osamu Sakai, and Yukihiro Shimizu. Numerical renormalization group study of magnetic impurities in superconductors. Journal of the Physical Society of Japan, 61(9):3239–3254, 1992.

[43] Johannes Bauer, Akira Oguri, and AC Hewson. Spectral properties of locally correlated electrons in a bardeen–cooper–schrieffer superconductor. Journal of Physics: Condensed Matter, 19(48):486211, 2007.